

**Swift Heavy Ion Irradiation and Thermal Annealing Induced  
Modification of Structural, Topographical and Magnetic  
Properties in Monolayer and Bilayer Films Based  
on FeNiMoB and Zinc Ferrite**

Thesis submitted to  
Cochin University of Science and Technology  
in partial fulfilment of the requirements for the  
award of the degree of

**Doctor of Philosophy**

**Lisha Raghavan**



Department of Physics  
Cochin University of Science and Technology  
Cochin- 682022  
India

**August 2015**

**Swift Heavy Ion Irradiation and Thermal Annealing Induced Modification of Structural, Topographical and Magnetic Properties in Monolayer and Bilayer Films Based on FeNiMoB and Zinc Ferrite**  
**Ph.D. Thesis**

**Author:**

Lisha Raghavan  
Nandanam  
Amayoor P.O.  
Palakkad- 679310  
Kerala, India  
E-Mail: [lisharghvn@gmail.com](mailto:lisharghvn@gmail.com)

**Supervising Guide:**

Prof. (Dr.) M. R. Anantharaman  
Professor, Department of Physics  
Cochin University of Science and Technology  
Cochin - 682 022  
Kerala, India.

**August 2015**

Cover page illustration:

Front: AFM images of zinc ferrite thin films irradiated at fluences of  $1 \times 10^{12}$  and  $3 \times 10^{13}$  ions/cm<sup>2</sup>

Back: Hysteresis loop of FeNiMoB-Zinc ferrite films at room temperature and at 10K (with field cooling). MH at 10K shows a shift in loop indicating exchange bias in the system.



Department of Physics  
Cochin University of Science and Technology  
Cochin – 682022

## CERTIFICATE

Certified that the present Ph.D. thesis work entitled **“Swift Heavy Ion Irradiation and Thermal Annealing Induced Modification of Structural, Topographical and Magnetic Properties in Monolayer and Bilayer Films Based on FeNiMoB and Zinc Ferrite”** submitted by **Mrs. Lisha Raghavan** is an authentic record of research work carried out by her under my supervision in the Department of Physics in partial fulfillment of the requirements for the Degree of Doctor of Philosophy of Cochin University of Science and Technology, and has not been included in any other thesis submitted previously for the award of any degree.

August 2015  
Cochin -22

**Prof. M. R. Anantharaman**

Supervising Guide  
Department of Physics  
CUSAT

# DECLARATION

I hereby declare that the Ph.D. thesis work entitled, **“Swift Heavy Ion Irradiation and Thermal Annealing Induced Modification of Structural, Topographical and Magnetic Properties in Monolayer and Bilayer Films Based on FeNiMoB and Zinc Ferrite”** is based on the original work carried out by me under the guidance of **Prof. M R Anantharaman**, in the Department of Physics, Cochin University of Science and Technology, Cochin-22 and has not been included in any other thesis submitted previously for the award of any degree.

Cochin – 22  
August 2015

**Lisha Raghavan**



Department of Physics  
Cochin University of Science and Technology  
Cochin – 682022

## CERTIFICATE

Certified that all the relevant corrections and modifications suggested by the audience during the Pre-synopsis seminar and recommended by the Doctoral Committee of the candidate has been incorporated in the thesis.

Cochin -22  
August 2015

**Prof. M. R. Anantharaman**

Supervising Guide  
Department of Physics  
CUSAT

## **ACKNOWLEDGEMENT**

*The supreme power who created us, who bestows us with all blessings and without the power of Almighty nothing is possible.*

*After four and half years of research work at Department of Physics, Cochin University of Science and Technology, now the stage has arrived to remember and thank everyone for all their helping hands, support and friendship. This is a tedious task as the help rendered by well-wishers cannot be belittled to a word "Thank You". But still this is the opportunity to remember each and everyone who have stood by me for the successful accomplishment of the PhD program and inception of a research career.*

*It gives me immense pleasure to acknowledge my deep sense of gratitude and indebtedness to my supervisor Prof. M. R. Anantharaman. He is an incessant researcher, an excellent teacher and well proficient in his field. Despite his busy schedule, he has given his precious time to discuss and interact with each and every student. He opened in front of me the doors of research and opportunities to meet many eminent scientists working in this realm. His motivations, mental support and words keep me going during these years. I wholeheartedly thank him for all the assistance and care provided.*

*I thank all the teachers and non teaching staff of the Department of Physics for their help and support.*

*During these years I have been a frequent visitor at Inter University Accelerator Centre, New Delhi and the institute also supported me with funding during the first three years of research. I gratefully express my sincere thanks to Dr. D K Avasthi for his guidance*

*and support. The constructive discussions I had with him aided me to plan, execute and analyze a Physics problem more scientifically. I am grateful to Dr. Ambuj Tripathi, Dr V V Sivakumar, Dr K Asokan, Dr. Pawan Kularia, Mr. Abhilash S. R, Mrs. Indra Sulania for their help during experiments. I am particularly obliged to Mr. Sunil Ojha for his unconditional support and amicable discussions in understanding and analyzing RBS data. I wish to express my sincere thanks to Dr. Udai, Dr. Srishti Gupta, Compesh and Sonu for helping me during sample measurements and data analysis. I am deeply thankful to the research scholars and research associates of IUAC especially Dr. Tanuj, Dr. Shammi Varma, Renu, Manju, Dr. Lakshmi, Phaneendra and the users of IUAC Ratnesh, Meenu, Ruchi, Shareef, Shamlath, Laveen for making my stays at IUAC memorable.*

*Magnetic measurements related to the thesis problem were carried out at UGC DAE CSR Indore. Special gratitude is expressed to Dr. V Ganesan, Director and former director Dr. Ajay Gupta for providing facilities. I express my heartfelt thanks to Dr. R V Reddy, Dr. Ram Janay Choudhary and Dr. Alok Banerjee for providing me facilities and fruitful suggestions. I am much indebted to Ms. Komal Bapna and Pankaj Pandey who were friendly with me and helped in performing the magnetic measurements.*

*The help provided by Dr. Raju Ramanujan, Nanyang Technological University, Singapore and Dr. P A Joy, NCL Pune needs special mention.*

*Magnetics Laboratory have always been warm and provided a homely atmosphere. Hysen chetan has always helped me in my work by providing suggestions and corrections. Geetha chechi also provided great*

*help and also her support to me both in my personal and academic life is beyond words. Lija and I joined the lab at the same time and has been a good friend. The friendship with Sivaraj, Babu sir and Aravind needs special mention. I thank all other members Reena chechi, Smitha chechi, Vinaya chechi, Sethu chechi, Sudeepetan, Archana, Thoufeeq and Sreeram. Beena have always been a very good friend and the moments spend with her are indeed cherishable. I also remember the friendship of Santhosh, Deepu, Geethu, Aswathy, Aiswarya, Manju chechi, Parvathi, Soumya chechi and other research scholars of the university.*

*With deep respect, I recollect the eminent professors at Department of Physics, University of Calicut who have instilled research in me. I am much obliged to Prof. Vishnu Mayya Bannur, his classes and words were always a motivation to learn Physics. Also I remember Prof. K. P. Subramanian, Physical Research Laboratory, Ahmedabad with whom I did my M.Sc project. My friends and M.Sc classmates Vijith, Mithun and Sunil who are also in their final stages of PhD work always stood with me in my personal and academic life.*

*Finally my boundless gratitude to achan, amma, chechi, Rajiettan, Gayatri and Saneesh for their love, care and constant encouragement, without which I could not reach this stage.*

*Lisha Raghavan*



## PREFACE

Magnetism and magnetic materials have been playing a lead role in the day to day life of human beings. The human kind owes its gratitude to the 'lodestone' meaning 'leading stone' which led to the discovery of nations and the onset of modern civilizations. If it was William Gilbert, who first stated that 'earth was a giant magnet', then it was the turn of Faraday who correlated electricity and magnetism. Magnetic materials find innumerable applications in the form of inductors, read and write heads, motors, storage devices, magnetic resonance imaging and fusion reactors. Now the industry of magnetic materials has almost surpassed the semiconductor industry and this speaks volumes about its importance. Extensive research is being carried out by scientists and engineers to remove obsolescence and invent new devices. Though magnetism can be categorized based on the response of an applied magnetic field into diamagnetic, paramagnetic, ferromagnetic, ferrimagnetic and antiferromagnetic; it is ferrimagnetic, ferromagnetic and antiferromagnetic materials which have potential applications. The present thesis focusses on these materials, their composite structures and different ways and means to modify their properties for useful applications.

In the past, metals like Fe, Ni and Co were sought after for various applications though iron was in the forefront because of its cost effectiveness and abundance. Later, alloys based on Fe and Ni were increasingly employed. They were used in magnetic heads and in inductors. Ferrites entered the arena and subsequently most of the newer applications were based on ferrites, a ferrimagnetic material, whose composition can be tuned to tailor the magnetic properties. In the late 1950s a new class of magnetic material emerged on the magnetic horizon and they were fondly known as metallic glasses. They are well

known for their soft magnetic properties. They were synthesized in the form of melt spun ribbons and are amorphous in nature and they are projected to replace the crystalline counterparts.

Metallic glasses are alloys of transition elements and metalloids and have attracted the attention of technologists owing to their superlative soft magnetic properties compared to other conventional crystalline materials. The transition elements like Fe, Co, Ni imparts magnetic properties, while metalloids like B and Si aid in amorphisation and Mo and Nb act as grain growth inhibitors. Nanocrystallinity can be induced in these alloys by thermal annealing and this improves the soft magnetic properties. The nanocrystalline thin films are highly sought after for read and write heads and sensors. Metallic glass having a composition of  $\text{Fe}_{40}\text{Ni}_{38}\text{Mo}_4\text{B}_{18}$  exhibits high saturation magnetisation, high Curie temperature and low anisotropy and crystallizes at  $400^{\circ}\text{C}$ . The bulk properties of these alloys are well studied; however studies on thin films are rare in literature. Earlier investigations carried out in this laboratory on thin film forms of these alloys by employing vacuum evaporation yielded films with excellent magnetic properties; however the target and the film composition were at variance. Retaining the composition of the target in the film as well is necessary as this influences the magnetic properties substantially.

Preparation of thin films based on FeNiMoB incorporating the target elements and modification of its properties by various techniques is interesting as this system can act as an ideal template to study the role of target element, crystallinity and surface morphology on the magnetic properties. Fabrication of thin films by Radio Frequency (RF) sputtering is an ideal alternative and this forms part of the objective of this study. Moreover, a study on such thin film

forms will be a prelude for magnetic MEMS (Micro Electro Mechanical Systems).

Zinc ferrite is a normal spinel and known for its antiferromagnetic properties with a Neel temperature of 10K. However anomalous results are reported in the literature for nano zinc ferrite. In spite of the continued efforts by researchers, a conclusive explanation for such a behaviour is still elusive. The properties of zinc ferrite are highly dependent on the synthesis method. Zinc ferrite is purported to be an antiferromagnet and exhibits size effects on its magnetic properties and can exhibit ferrimagnetism at room temperature. These anomalies make zinc ferrite stand out among other spinels. Most of the studies on zinc ferrite thin films lack high magnetisation at room temperature. A thin film form of zinc ferrite with appreciable saturation magnetisation will be a good candidate for fundamental research as well as for applications.

Exchange bias effect is the phenomenon wherein the spins of ferromagnet are pinned by the antiferromagnetic spins on field cooling below the Neel temperature of the antiferromagnet. As a result the hysteresis loop is shifted along the field axis accompanied by loop widening and shift in magnetisation direction. These kind of structures are highly desirable in spin valves and magnetic tunnel junctions. Theoretical and experimental studies have been done widely on the field of exchange bias, still technologists look for novel materials and techniques to control the exchange bias. Earlier exchange bias studies were mainly on ferromagnetic-antiferromagnetic system; but recently it has been reported that ferromagnetic-spin glass, ferrimagnetic-antiferromagnetic and even soft-hard magnetic systems can exhibit exchange bias. A bilayer system of FeNiMoB-zinc ferrite can exhibit exchange bias and is one of the main themes of this thesis. The modification of exchange bias by various techniques is also important.

Once we have the desired film, the next question is how can we improve or tailor the properties. Usually thermal annealing is employed which can alter the grain size and thus can change the magnetic properties. The effect of thermal annealing on films of FeNiMoB, zinc ferrite and their bilayer structure is being investigated.

Another technique to modify the material properties is by subjecting them to ion beam irradiation. Ion beams can be employed for synthesis, modifications and characterization of materials. When ions traverse through a material, they can impart their energy and momentum to the material. Depending on the energy of ions two regimes can be defined viz, nuclear energy regime (few KeV) and electronic energy regime ( $>$  few MeV). Swift heavy ion (SHI) irradiation can alter magnetic properties of bulk materials as well as thin films. The magnetic properties of thin films depends on a range of factors like composition, crystallinity, crystal structure, anisotropies-magneto-crystalline, surface and interface roughness, domain structure. By tailoring any of the above properties the magnetic properties can be modified.

Of the various factors affecting magnetic properties, inducing crystallinity seems to be a promising way to alter the magnetic characteristics due to the ease by which a material can be crystallised. Crystallization can be realised by thermal annealing whereas amorphisation can be induced in the material by SHI irradiation. Irradiation in crystalline materials results in creation of amorphous tracks embedded in the residual crystalline matrix. Ion irradiation can also result in ion beam mixing at the interface of two layers. Such investigations are of paramount importance in modifying the interfaces which will have a positive bearing on the exchange bias. Spinel structures are susceptible to track formation.

The track formation and the resulting changes in room temperature and low temperature magnetic properties as a result of ion irradiation will be studied.

The exchange bias depends on the ferromagnet-antiferromagnet interface. Ion beams can create defects as well as result in interface mixing in a bilayer structure. The modification of exchange bias and the resultant exchange field can be probed by ion irradiation. Ion beam irradiation induced modification of exchange bias in FeNiMoB- zinc ferrite bilayer structure is examined in the present thesis.

The effect of swift heavy ion irradiation and thermal annealing on the structural, topographical and magnetic properties of FeNiMoB- zinc ferrite thin films are of major concern in the present thesis.

The main objectives of the present study are the following:

1. To replicate the exact composition of  $\text{Fe}_{40}\text{Ni}_{38}\text{Mo}_4\text{B}_{18}$  in their thin film forms by RF sputtering.
2. To study the effect of thermal annealing on the structural and magnetic properties of RF sputtered FeNiMoB thin films.
3. To tailor magnetic characteristics of FeNiMoB thin films by swift heavy ion irradiation.
4. To prepare zinc ferrite thin films by RF sputtering and detailed investigation of the mechanism responsible for magnetism in thin films.
5. To create amorphous tracks in zinc ferrite thin films by swift heavy ion irradiation.
6. To prepare exchange biased FeNiMoB – zinc ferrite bilayer film

7. To study the modification of exchange bias in FeNiMoB – zinc ferrite bilayer films by Swift heavy ion irradiation.

The proposed thesis is entitled “**Swift Heavy Ion Irradiation and Thermal Annealing Induced Modification of Structural, Topographical and Magnetic Properties in Monolayer and Bilayer Films Based on FeNiMoB and Zinc Ferrite**” and consists of eight chapters.

**Chapter 1** gives an introduction to magnetism in general and ferromagnetism and antiferromagnetism in particular. The physics behind exchange bias effect and ion interaction in materials is dealt with in this chapter.

The preparation methods and experimental techniques used for the present study are described in **chapter 2**.

The thermal annealing effects on structural, topographical and magnetic properties of FeNiMoB films prepared by RF sputtering are presented in **chapter 3**.

**Chapter 4** deals with swift heavy ion irradiation on RF sputtered FeNiMoB films with a view to enhancing the soft magnetic properties.

**Chapter 5** describes preparation of zinc ferrite thin films by RF sputtering and the room temperature and low temperature magnetic ordering in these films. Effect of annealing is also one of the themes of this chapter.

The amorphisation and modification of properties in zinc ferrite films by swift heavy ion irradiation is covered in **chapter 6**.

**Chapter 7** explains the exchange bias studies in FeNiMoB-zinc ferrite bilayer and its modification by thermal annealing and swift heavy ion irradiation. It was inferred that on ion irradiation, exchange bias greatly enhanced.

Finally conclusions of the research work and future outlook is presented in **chapter 8.**

**PEER REVIEWED PUBLICATIONS:**

1. Defect induced enhancement of exchange bias by Swift Heavy Ion irradiation in Zinc Ferrite-Fe-Ni-Mo-B alloy based bilayer films, **Lisha R.**, Hysen T., Geetha P., Aravind P. B., Shareef M., Shamlath A., Sunil Ojha, R. V. Ramanujan, M. R. Anantharaman, (Accepted for publication in Nuclear Instruments and Methods in Physics Research B)
2. Exchange Bias In Zinc Ferrite-FeNiMoB Based Metallic Glass Composite Thin Films, **Lisha R.**, Hysen T, Geetha P, Aravind P B, S. Ojha, D K Avasthi, R V Ramanujan, M R Anantharaman, AIP Conference Proceedings 1665 (2015) 130045
3. Room temperature ferrimagnetism and low temperature disorder effects in zinc ferrite thin films, **Lisha Raghavan**, Geetha Pookat, Hysen Thomas, Sunil Ojha, D K Avasthi, M R Anantharaman, Journal of Magnetism and Magnetic Materials 385 (2015) 265–271
4. Structural, topographical and magnetic evolution of RF sputtered Fe-Ni alloy based thin films with thermal annealing, **Lisha R.**, Hysen T, Geetha P., D. K. Avasthi, R V Ramanujan, M R Anantharaman, Materials Research Express 1 (2014) 015707
5. Effect of 100 MeV  $\text{Ag}^{+7}$  ion Irradiation on the Bulk and Surface Magnetic properties of Co-Fe-Si Thin films, T Hysen, Geetha P, Salim Al-Harhi, I. A. Al-Omari, **Lisha R.**, R V Ramanujan, Sakthikumar D, D. K. Avasthi and M R Anantharaman, Journal of Magnetism and Magnetic Materials 372 (2014) 224–232

6. Annealing induced low coercivity, nanocrystalline Co–Fe–Si thin films exhibiting inverse cosine angular variation, T.Hysen, Salim Al-Harhi, I.A. Al-Omari, P.Geetha, **R.Lisha**, R.V.Ramanujan, D.Sakthikumar, M.R. Anantharaman, *Journal of Magnetism and Magnetic Materials* 341(2013)165–172
7. Magnetic and topographical modifications of amorphous Co-Fe thin films induced by high energy Ag<sup>7+</sup> ion irradiation, G Pookat, T Hysen, S H Al-Harhi, I A Al-Omari, **R Lisha**, D K Avasthi, M R Anantharaman, *Nuclear Instruments and Methods in Physics Research B* 310 (2013) 81–86.
8. Evolution of structural and magnetic properties of Co-Fe based metallic glass thin films with thermal annealing, G. Pookat, H. Thomas, S. Thomas, S.H. Al-Harhi, **L. Raghavan**, I.A. Al Omari, D. Sakthikumar, R. V. Ramanujan, M. R. Anantharaman, *Surface and coatings technology* 236 (2013) 246–251.

#### **CONFERENCE PROCEEDINGS**

1. Tailoring topographical and magnetic properties of Fe-Ni alloy based thin films by 100 MeV Ag ions, **Lisha Raghavan**, Hysen Thomas, Geetha Pookat, Aravind P B, Shareef M, Shamlath A, Sunil Ojha, Indra Sulania, D K Avasthi, Raju Ramanujan, M R Anantharaman, International conference on Swift heavy Ions in materials Science **SHIMEC 2014**, (Oral presentation)
2. Exchange Bias In Zinc Ferrite-FeNiMoB Based Metallic Glass Composite Thin Films, **Lisha R**, Hysen T, Geetha P, Aravind P B, S. Ojha, D K Avasthi, R V Ramanujan, M R Anantharaman, 59<sup>th</sup> DAE Solid State Physics Symposium **DAE-SSPS-2014**.
3. Effect of substrate temperature on the structural, topographical and magnetic properties of zinc ferrite thin films, **Lisha Raghavan**, Hysen Thomas, Geetha P,

- M R Anantharaman, ISAS National conference on Advanced Technologies for Material Processing and Diagnostics (**Third Best Poster Prize**)
4. Tailoring topographical and magnetic properties of zinc ferrite thin films by 100 MeV Ag<sup>7+</sup> ion irradiation, **Lisha R**, Hysen T, Geetha P, Shareef M, Shamlath A, Sunil Ojha, Indra Sulaniya, D K Avasthi, M R Anantharaman, Accepted for Poster presentation for International conference on Magnetic Materials and applications, **ICMagMA 2014, (Best Poster Prize)**
  5. Ion Irradiation: A versatile tool for material modification, **Lisha Raghavan**, Hysen Thomas, Geetha P, M R Anantharaman, National seminar on Current trends in material science 2014 (Oral presentation)
  6. Ion Irradiation induced modification of materials, **Lisha Raghavan**, Hysen Thomas, Geetha P, M R Anantharaman, National Seminar on Frontiers of Nanotechnology 2014 (Oral presentation)
  7. Evolution of topographical and magnetic properties of zinc ferrite thin films with annealing, **Lisha Raghavan**, Hysen Thomas, Geetha Pookat, M R Anantharaman, International conference on Magnetic Materials and applications, **MagMA 2013**
  8. Depth profiling in Zinc Ferrite - Metglas bilayer films using Rutherford Backscattering Spectrometry, **Lisha Raghavan**, Hysen Thomas, Geetha Pookat, Sunil Ojha, M R Anantharaman, International conference on nanostructuring by ion beams **ICNIB-2013**
  9. Fabrication of Nano crystalline thin film based on Iron Nickel for MEMS applications-An initial study, **Lisha Raghavan**, Hysen Thomas, Geetha Pookat and M R Anantharaman, India Israel Meeting on Material science and Nanoscience - **IIMNN 2013.**



## CONTENTS

<b>Chapter 1- Introduction</b>	<b>1</b>
1.1 Introduction	3
1.2 Magnetism in materials	4
1.2.1 Diamagnetism	5
1.2.2 Paramagnetism	5
1.2.3 Ferromagnetism	6
1.2.4 Antiferromagnetism	9
1.2.5 Ferrimagnetism	11
1.2.6 Superparamagnetism	11
1.2.7 Spin Glasses	12
1.2.8 Hard and Soft Magnets	12
1.3 Magnetism in amorphous and nanocrystalline alloys	13
1.3.1 Random Anisotropy Model: Herzer Model	18
1.3.2 Metallic Glasses	20
1.4 Magnetism in spinels	21
1.4.1 Zinc Ferrite	22
1.5 Magnetism at ferromagnet-antiferromagnet interface- Exchange Bias	25
1.5.1 Phenomenon	25
1.5.2 Evolution of Exchange Bias	27
1.6 Ion interaction with materials	30
1.6.1 Swift Heavy Ions (SHI)	33
1.6.2 Ion Beam Mixing	35
1.7 Modification of magnetic properties by SHI	36
1.8 Motivations and objectives	39

References	43
<b>Chapter 2 -Experimental Methods</b>	<b>55</b>
2.1 Synthesis of Nanomaterials	57
2.1.1 Sol Gel Auto Combustion	57
2.2 Thin Film Deposition	58
2.2.1 Sputtering	59
2.3 Ion Irradiation Facility	61
2.3.1 Pelletron accelerator	61
2.4 Rutherford Backscattering Spectrometry	64
2.5 X- Ray Reflectivity	67
2.6 X-Ray Diffractometer	69
2.7 Glancing Angle X- Ray Diffractometer	72
2.8 Transmission Electron Microscope	73
2.9 Selected Area Electron Diffraction	75
2.10 X-ray Photoelectron Spectroscopy	76
2.11 Atomic Force Microscope	79
2.12 Vibrating Sample Magnetometer	81
2.13 Superconducting Quantum Interference Device Magnetometer	83
2.13.1 Modes of Magnetic Measurements	84
References	86
<b>Chapter 3 - Fabrication of RF sputtered FeNiMoB thin films and modification of its structural, topographical and magnetic properties by thermal annealing</b>	<b>87</b>
3.1 Introduction	89
3.2 Experimental Methods	91

3.3 Results and Discussions	92
3.4 Conclusion	104
References	104
<b>Chapter 4- Tailoring topographical and magnetic properties of FeNiMoB films by 100 MeV Ag ions Swift Heavy Ion irradiation</b>	<b>107</b>
4.1 Introduction	109
4.2 Experimental Methods	110
4.3 Results and Discussions	111
4.4 Conclusion	119
References	120
<b>Chapter 5- On the room temperature ferrimagnetism in RF sputtered zinc ferrite thin films and disorder effects at low temperature</b>	<b>123</b>
5.1 Introduction	125
5.2 Experimental Methods	126
5.3 Results and Discussions	127
5.4 Conclusion	137
References	138
<b>Chapter 6- Evolution of structural, topographical and magnetic properties of zinc ferrite thin films by Swift Heavy Ion irradiation</b>	<b>141</b>
6.1 Introduction	143
6.2 Experimental Methods	144
6.3 Results and Discussions	145
6.4 Conclusion	154
References	155
<b>Chapter 7- Exchange bias in FeNiMoB-Zinc Ferrite bilayer films</b>	<b>159</b>
7.1 Introduction	161

7.2 Experimental Methods	164
7.3 Results and Discussions	165
7.3.1 Dependence of film thickness and thermal annealing on Exchange Bias	165
7.3.2 Dependence of SHI irradiation on exchange bias	168
7.4 Conclusion	176
References	177
<b>Chapter 8-Conclusions and Future Scope</b>	<b>181</b>

## **Chapter 1**

### **Introduction**

1.1 Introduction

1.2 Magnetism in materials

1.3 Magnetism in amorphous and nanocrystalline alloys

1.4 Magnetism in spinels

1.5 Magnetism at ferromagnet-antiferromagnet interface-Exchange Bias

1.6 Ion interaction with materials

1.7 Modification of magnetic properties by Swift Heavy Ions (SHI)

1.8 Motivations and objectives

References

*Chapter 1*

## **1.1 INTRODUCTION**

The history of magnetism can be traced to the serendipitous discovery of 'magnetite' a naturally occurring mineral in present day Turkey. This material later came to be known by the name 'lodestone' meaning leading stone. The journey from lodestone to the present day molecular magnets has been replete with newer phenomenon and novel materials. Thus the phenomenon of magnetism and the field of magnetic materials is evergreen and remained temporal. It is as attractive as a toy to a child as well as to a scientist or engineer.

Magnetic materials find umpteen applications in a horde of devices namely inductors, transformer cores, memory elements, read and write heads, refrigerator door seals, motors, spintronics, automobiles. The list is endless and new devices are being added on a day to day basis. In the post industrial revolution era most of the applications were based on Fe, Ni, Co. Then came alloys and in that permalloys were a good choice for various applications. Permalloys were slowly replaced by ferrites and are still in vogue. However in the late 60's and early 70's, metallic glass became popular and slowly started replacing conventional ferrites. Metallic glasses are basically amorphous in nature and find usefulness as memory devices, read and write heads, sensors because of their superlative soft magnetic properties. The functionality of metallic glasses further improved with the advent of nanocrystallinity induced in these materials by thermal annealing. They exhibited excellent magnetic properties which could be controlled by tuning the grain size. The emergence of Micro Electro Mechanical Systems (MEMS) and Nano Electro Mechanical Systems (NEMS) devices demanded that these devices are in the thin film form and a great deal of studies are on the thin film form of these alloys. Among various metallic glasses which are in use Fe-Ni and Fe-Co are the most popular candidates. A tiny amount

of B, Si, or Mo are also added in these alloys either to inhibit grain growth or for amorphisation as the case maybe. The properties exhibited by thin films are different from the bulk and assumes great significance from a fundamental perspective. Recently these alloy thin films form part of devices such as MEMS, NEMS, Giant magnetoresistance (GMR) and Tunnel magnetoresistance (TMR) sensors. This thesis takes a look at the interesting properties exhibited by the thin film form of these alloys especially Fe-Ni and different ways to modify their properties. Also, investigations on thin film form of zinc ferrite and bilayer films based on Fe-Ni and zinc ferrite for exchange bias properties are also examined.

## 1.2 MAGNETISM IN MATERIALS

The magnetic property in a material is due to its spin and orbital angular momentum. An electron moving round the nucleus causes a magnetic moment and the moment is defined as the current flowing through unit area of the circular loop. As magnetic property is a collective phenomenon, the magnetism observed in atomic scale and microscopic scale are quite different [1]. On application of a magnetic field  $H$ , the magnetism induced in the material is called magnetic induction  $B$ . The magnetization  $M$  in material is defined as the magnetic moment per unit volume  $V$ .

$$B = H + 4\pi M \quad (1.1)$$

$$M = \frac{m}{V} \quad (1.2)$$

The ratio of magnetization to applied magnetic field is defined as susceptibility  $\chi$  and is telltale of the response of material to an applied field.

$$\chi = \frac{M}{H} \quad (1.3)$$

According to the response of a material to an applied magnetic field, materials are classified as diamagnetic, paramagnetic, ferromagnetic, ferrimagnetic and antiferromagnetic. Each property is detailed in the following sections.

### **1.2.1 Diamagnetism**

This is the weakest magnetic effect and is observed in all materials. On applying a magnetic field, the change in orbital motion of electrons induces a moment opposite to that of the applied field. Hence, the susceptibility is negative. All elements exhibit diamagnetism but the effect is usually surpassed by other strong magnetic properties. Elements with completely filled shells exhibit diamagnetic properties. Lack of magnetization limits them for various applications but the main forte of diamagnetic materials are in superconductors.

### **1.2.2 Paramagnetism**

Paramagnetism refers to the property of atomic spins to align in accordance with an applied magnetic field (figure 1). As the magnetic moments are weakly coupled with each other, the magnetisation is very small. It is usually observed in elements with unpaired electrons. Paramagnetic materials have a positive value of susceptibility.

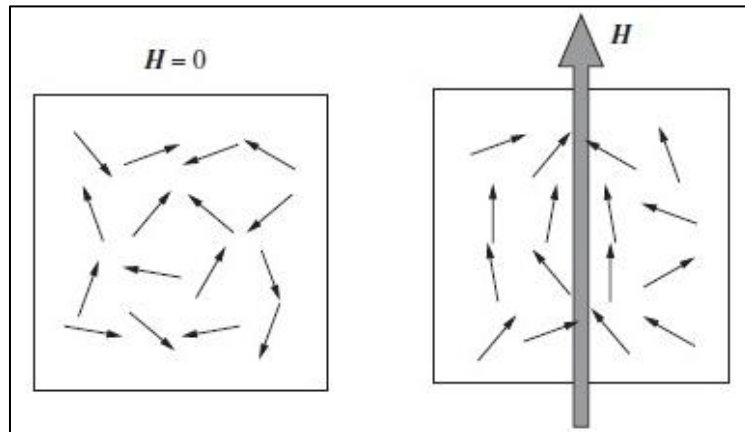


Fig. 1 Alignment of spins in paramagnetic material without and with a magnetic field [2]

### 1.2.3 Ferromagnetism

The ferromagnetic property of a material is due to its unpaired electron in its orbital. Fe, Ni and Co are the room temperature ferromagnetic elements. Due to the interaction among the spins of a ferromagnet, an effective magnetic moment is observed without an applied magnetic field. Above a particular temperature called Curie temperature; wherein the thermal effects become stronger to perturb the aligned spins, the material behaves as paramagnet. Ferromagnetic materials have large positive susceptibility and variation of susceptibility with temperature is given by Curie Weiss law.

$$\chi = \frac{C}{T - T_c} \quad (1.4)$$

where, C is the Curie constant, T temperature and  $T_c$  the Curie temperature.

Weiss proposed the domain theory of ferromagnetism in 1907 [3]. According to the domain theory, a ferromagnet consists of regions called domains, that are spontaneously magnetized; but the magnetisation of individual

moments are random so that they cancel each other giving rise to a zero moment. He also suggested the existence of molecular field that act in a ferromagnetic material which magnetize the material even in the absence of a magnetic field. The limitation of Weiss theory was that it failed to explain the origin of the molecular field.

Heisenberg in 1928 put forward a quantum mechanical model for ferromagnetism [4]. The theory is grounded on quantum mechanical exchange interactions among spins and depends on the relative orientation of two spins. If two atoms have spins  $S_i$  and  $S_j$ , the exchange energy is expressed as,

$$E_{ex} = -2J_{ex} \vec{S}_i \cdot \vec{S}_j \quad (1.5)$$

where,  $J_{ex}$  is the exchange integral. The condition for stability is that exchange energy has to be minimum. For ferromagnetic ordering, the spins should align parallel and the dot product is positive. This set a constraint on  $J_{ex}$  that, for energy to be negative  $J_{ex}$  should be positive. Therefore in ferromagnetic materials exchange integral has to be positive. The Bethe Slater curve (figure 2) shows the variation of exchange integral with  $D/d$  ratio, where  $D$  and  $d$  are atomic separation and diameter of 3d orbital respectively. From the Bethe Slater curve, Fe, Co and Ni have  $J_{ex}$  positive and are room temperature ferromagnetic elements [5].

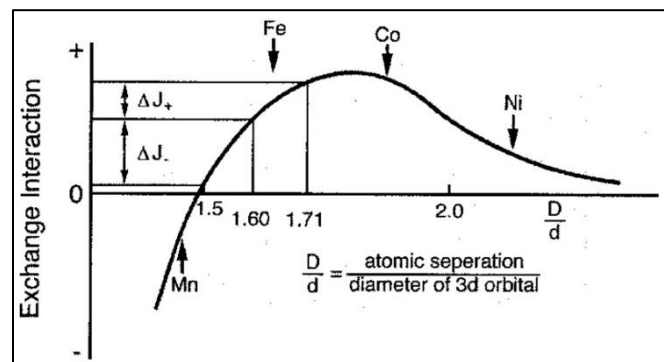


Fig. 2 Bethe Slater curve [5]

## *Chapter 1*

The domain theory and the Heisenberg theory successfully explained the concept of domains, exchange interaction and temperature dependence of susceptibility; but failed to account for the exact value of magnetic moment in metals. Both these theories are also referred as localized moment theory, as they are based on the assumption that, the electrons responsible for ferromagnetism are attached to a single atom and cannot move about in crystal. This has been overcome by the collective electron model or the Band theory of magnetism [6]. Band theory discards the localization of electron to single atom and electrons are assumed to belong to the whole crystal and can move from atom to atom. When atoms are brought together, the electron clouds overlap and discrete energy levels of individual atoms with same energy should split, so that Pauli's exclusion principle is not violated. The extent of splitting differs for various energy levels, and the levels spread out and results in formation of bands as shown in figure 3. According to the band theory, for ferromagnetism, the electrons must lie in partially filled bands so that there are vacant levels where electrons can move. The density of levels in the bands must be high, so that the increase in energy caused by spin alignment will be small. For the interaction of d electrons via exchange forces, the atoms must be at the right distance.

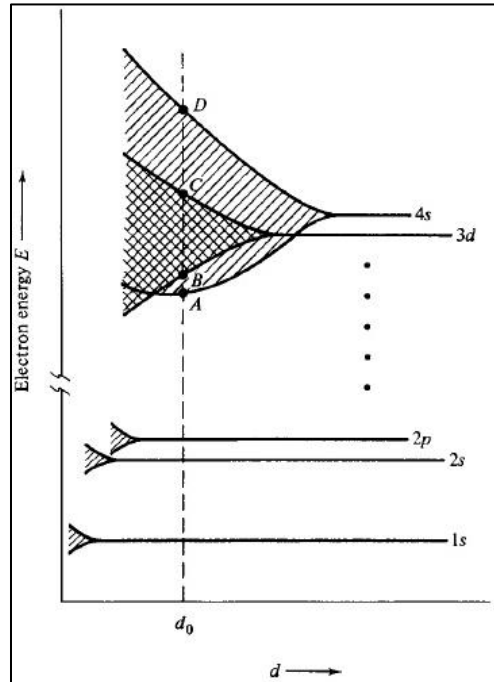


Fig. 3 Schematic of band theory of magnetism [6]

#### 1.2.4 Antiferromagnetism

In antiferromagnetic materials, the interaction between adjacent spins aligns moment antiparallel to each other (figure 4) and the effective magnetisation is zero. This alignment happens only below a critical temperature called Neel temperature, above which the material is paramagnetic. Antiferromagnetic materials have a small positive value of susceptibility and above Neel temperature it follows the features of paramagnet, while below Neel temperature susceptibility decreases with temperature (figure 4). Antiferromagnetism arise in a material, when there are two interpenetrating sub-lattices with the moments equal and opposite, and effective moment is the sum of moments of the sub-lattices which is zero.

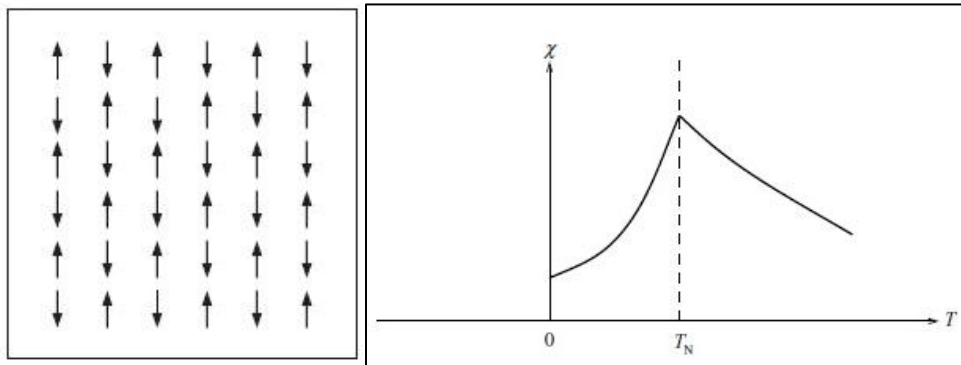


Fig. 4 Alignment of spins in antiferromagnet and the variation of susceptibility with temperature [2]

The well known antiferromagnetic material is MnO and its antiferromagnetism can be explained based on the super exchange interaction, that is, exchange interaction mediated through non magnetic atoms, usually oxygen. For covalent sharing of spins from oxygen, the spins of the sublattices of Mn should align antiparallel to each other which gives rise to the antiferromagnetic ordering.

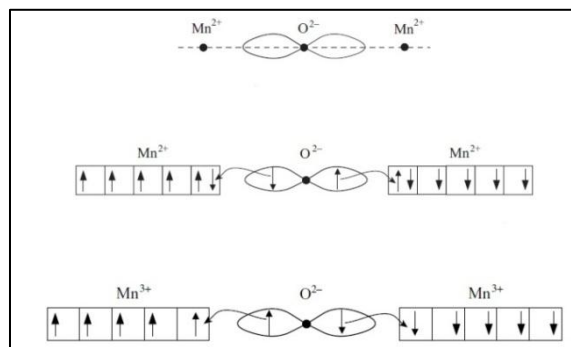


Fig. 5 Schematic of super exchange interaction [2]

### 1.2.5 Ferrimagnetism

In this kind of magnetic interaction, the coupling of moments result in antiparallel orientation but moment of one sublattice is higher than the other which introduces an effective magnetization. The ferrimagnetic materials behave similar to ferromagnets, in that they exhibit hysteresis loops and high magnetization.

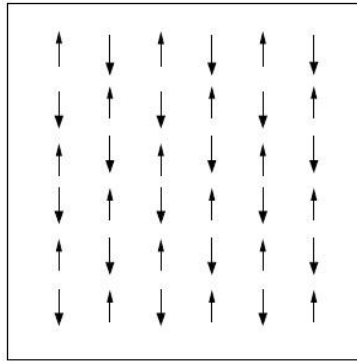


Fig. 6 Alignment of spins in ferrimagnet [2]

### 1.2.6 Superparamagnetism

It is a state of zero coercivity and zero remanence. This kind of magnetic property is observed in the nanoregime. In nanoparticles, the surface to volume ratio is high. The particle volume reduces and the anisotropy energy, which is the product of anisotropy constant and volume also come down. In such cases, the thermal energy overcomes the anisotropy energy and magnetization direction flips easily [2]. The relaxation time of the spin flipping is given by [7],

$$\tau = \tau_0 e^{\left(\frac{E_B}{k_B T}\right)} = \tau_0 e^{\left(\frac{KV}{k_B T}\right)} \quad (1.6)$$

## Chapter 1

where,  $k_B$  is the Boltzmann constant,  $V$  is the particle volume,  $\tau_0$  is the time scale characteristic of the material and its typical value is  $10^{-9}$  to  $10^{-10}$ s. The temperature at which the measurement time is equal to the relaxation time is called the Blocking temperature and  $T_B$  can be obtained from equation 1.6 as,

$$T_B \approx \frac{KV}{25k_B} \quad (1.7)$$

### 1.2.7 Spin Glasses

These are comparatively newer class of magnetic materials and is said to be the most complex kind of condensed state encountered so far in solid state physics [8]. Contrary to the magnetism discussed earlier which is long range ordered, the magnetism in spin glasses are ordered in short range. Spin glass is defined as a collection of spins whose low temperature state is frozen and disordered. Spin glasses are usually a result of magnetic frustration; that is, the spins compete each other in terms of configuration and no unique configuration is favored and the interactions of spins are random. Spin freezing temperature is the transition below which the system behaves as spin glass and above this temperature, system exhibit normal magnetic properties [9].

### 1.2.8 Hard and Soft magnets

Ferromagnets and ferrimagnets can be further classified according to the hysteresis loops as hard and soft magnets. Hard magnets are difficult to magnetize and demagnetize, they have large value of coercivity and remanence. They find application as permanent magnets. Soft magnets are easier to magnetize and demagnetize and they have low value of coercivity and remanence. Soft magnets are used as recording media, memory devices and read and write heads. Typical hysteresis curve of hard and soft magnets is shown in figure 7.

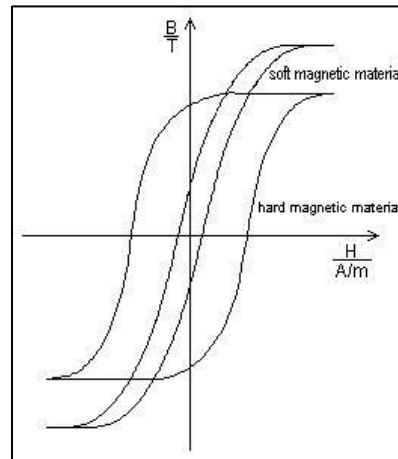


Fig. 7 Magnetic hysteresis of hard and soft magnets

### 1.3 MAGNETISM IN AMORPHOUS AND NANOCRYSTALLINE ALLOYS

In the earlier times, crystallinity was thought to be a necessity for magnetic phenomenon. BCC Fe and Co were the conventional materials used for soft magnetic properties. They were later replaced by permalloys, which are alloys of Fe and Ni. In the 1950s Duwez *et al.* introduced a new class of materials that exhibited better soft magnetic properties than permalloys and were amorphous [10]. This marked the beginning of a new study in the field of magnetism in amorphous materials.

Amorphous magnetic materials are excellent soft magnetic materials with high induction and permeability, low hysteresis losses, high Curie temperature and better mechanical properties like corrosion resistance. These amorphous alloys can be prepared by rapid solidification techniques like melt spinning and sputter quenching [5]. A typical amorphous magnetic material can be represented by  $T_{70-90}X_{10-30}$ , where T stands for transition metals like Fe, Co, Ni and X can be

Chapter 1

metalloids like B, Si or metals like Mo, Hf, Nb [11]. The transition elements impart magnetic properties, while metalloids aids in amorphisation and metals like Mo act as grain growth inhibitors. The alloy composition, microstructure and morphology influence the performance of these classes of materials. Regarding the alloy design, Slater Pauling curve provides information regarding the magnetic dipole moment and the alloy compositions (figure 8). Fe-Co alloys have high magnetic induction and they are also found to have high Curie temperature. Fe rich alloys have smaller induction and low Curie temperature while Co rich alloys have smaller induction and larger Curie temperature [5].

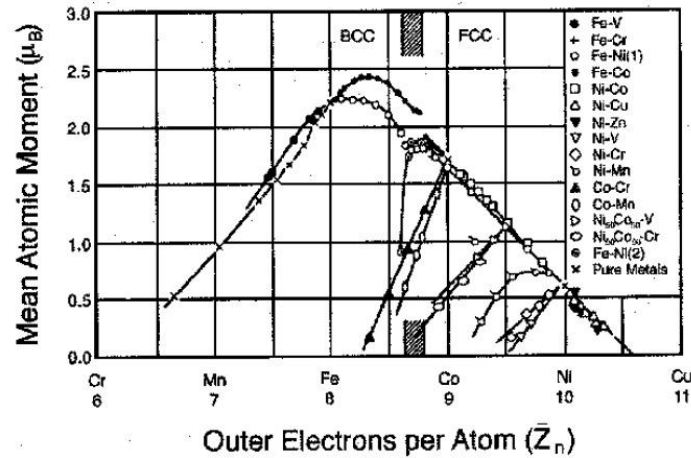


Fig. 8 Slater Pauling curve [5]

Soon after the advent of amorphous alloys, crystallinity was found to be a deteriorating factor for superior soft magnetic properties [12]. But later in 1988, Yoshizawa, Oguma and Yamauchi introduced a new class of alloys having Fe-Si-B with small additions of Cu and Nb [13]. This resulted in nanocrystalline magnetic alloys which created renowned interests in scientists and technologists.

These materials consist of nanocrystallites with grain size in the range 1-50 nm embedded in an amorphous matrix. They were found to exhibit superior soft magnetic properties than crystalline and amorphous magnetic materials. Nanocrystalline alloys can be formed from their amorphous counterparts by thermal annealing. Numerous nanocrystalline and amorphous alloys of different elements were developed and they have been patented under trade names like FINEMET, NANOPERM, HITPERM, METGLAS etc [5].

Several factors like magnetic anisotropy, magnetostriction, domain walls and grain size can have a profound influence on the magnetization of amorphous and nanocrystalline soft magnets [5]. Magnetic anisotropy refers to the directional dependence of magnetization and they are of different origins like magnetocrystallinity, shape and stress. The phenomenon that causes the material to magnetize along a specific crystallographic direction is called magnetocrystalline anisotropy. Anisotropy energy is the energy required to rotate the spin system of a domain away from the easy axes. For a cubic crystal, anisotropic energy is given by,

$$E = K_0 + K_1(\alpha_1^2\alpha_2^2 + \alpha_2^2\alpha_3^2 + \alpha_3^2\alpha_1^2) + K_2(\alpha_1^2\alpha_2^2\alpha_3^2) + \dots (1.8)$$

where,  $K_1$ ,  $K_2$  are anisotropy constants and  $\alpha_1$ ,  $\alpha_2$ ,  $\alpha_3$  are the direction cosines. Very small or negligible anisotropy is preferred for soft magnetic materials. The lack of crystallinity in amorphous materials leads to low magnetocrystalline anisotropy. Apart from crystal orientation, the shape of the material can also affect the magnetisation. The demagnetizing field  $H_d$  is the field that sets inside the material opposite to that of the applied field  $H_{app}$ .

$$H_d = N_d M \quad (1.9)$$

The effective field of the material is given by,

Chapter 1

$$H_{eff} = H_{app} - H_d \quad (1.10)$$

The demagnetizing field is always greater along the shorter axis of the material. To magnetize the material along shorter axis, larger fields will be required than that of longer axis. Shape and stress anisotropies are also minima in amorphous and nanocrystalline materials.

Magnetostriction refers to change in material dimension as a result of an applied magnetic field. Lower value of magnetostriction is preferred for soft magnetic applications. Fe based alloys have higher value of magnetostriction compared to Co based alloys.

In a ferromagnetic material, the domains are randomly oriented in the absence of a magnetic field and the growth of these domains with the applied field results in magnetization of the material. Thus, the process of magnetization is the growth of domains in the applied field direction, that is, a change over from multi-domains to single-domain (figure 9).

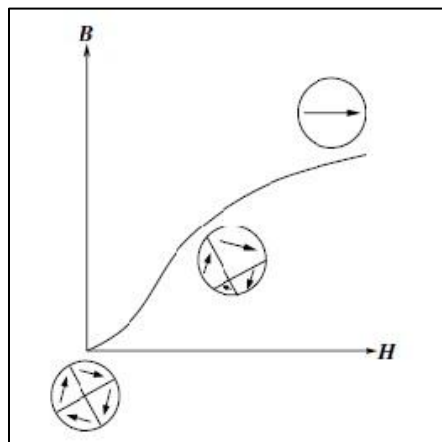


Fig. 9 Growth of domains in an applied magnetic field [2]

The formation of domains can minimize the total magnetostatic energy. In the absence of a field, each domains are spontaneously magnetized in different directions and these domains are separated by domain walls. Domain walls are the interfacial region separating two domains through which the magnetization direction change (figure 10). This change cannot be sudden, usually domains change through either  $180^\circ$  or  $90^\circ$  domain wall. The domain wall width is given by

$$\delta_w = \pi \sqrt{\frac{A_{ex}}{K_1}} \quad (1.11)$$

where,  $A_{ex}$  is the exchange stiffness and  $K_1$  the magnetocrystalline anisotropy. The width of domain walls and their movement influences the ease with which a material can be magnetized.

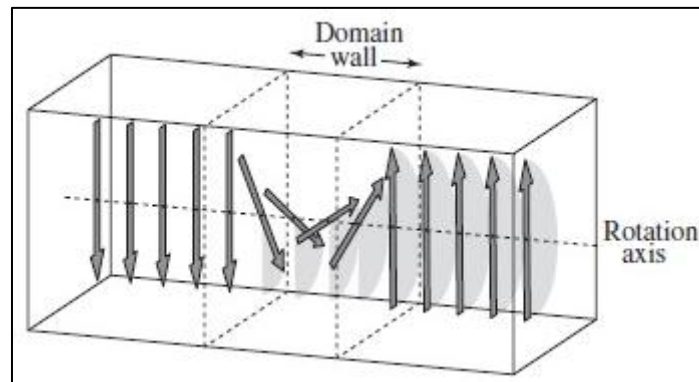


Fig. 10 Depiction of domain wall [2]

The  $180^\circ$  domain wall can further be classified on the basis of rotation of spins. If spins rotate parallel to the plane of domain wall, they are called as Bloch walls. Neel walls are formed if spin rotates perpendicular to the plane of domain walls.

Neel walls are observed in thin films. A pictorial representation of Bloch and Neel walls are shown in figure 11.

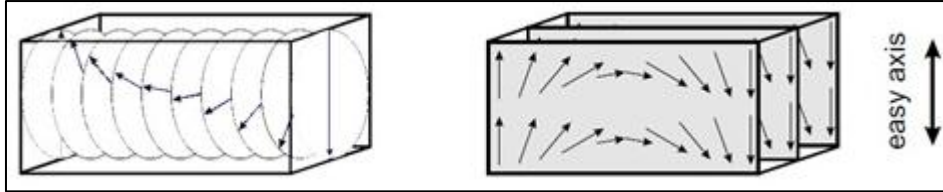


Fig. 11 Bloch and Neel domain walls [2]

### 1.3.1 Random Anisotropy Model: Herzer model

The random anisotropy in amorphous ferromagnets was first proposed by Alben *et al.* [14]. The model was modified by Herzer in 1990 [15]. According to earlier theories, the coercivity follows an inverse dependence on grain size, indicating smaller coercivities require larger grain sizes [15]. This was applicable for grain sizes greater than 100 $\mu\text{m}$ . This changes when we switch over to nano regime. If the grain size is less than the exchange correlation length, superlative soft magnetic properties are expected. Exchange correlation length  $L_{ex}$  is the minimum length scale below which, the ferromagnetic exchange interaction can be sensed.

$$L_{ex} = \varphi \sqrt{\frac{A}{|K_1|}} \quad (1.12)$$

According to Herzer model, if grain size is less than the exchange length, the anisotropies are averaged and the average anisotropy is given by, [15]

$$\langle K \rangle = K_1 x^2 \left[ \frac{D}{L_{ex}} \right]^6 \quad (1.13)$$

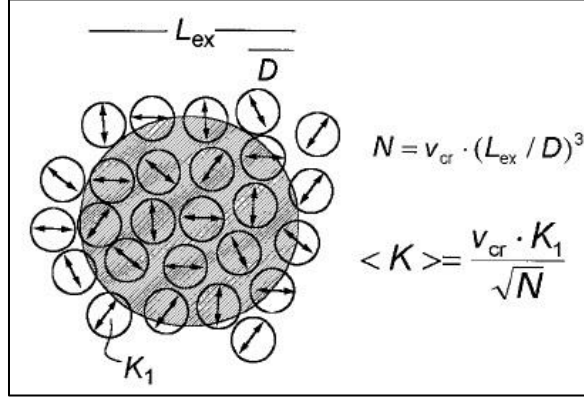


Fig. 12 Depiction of random anisotropy model [12]

The coercivity and permeability are related to anisotropy as;

$$H_c = \frac{p_c \langle K \rangle}{M_s} = \frac{p_c K_1^4 x^2 D^6}{M_s A^3} \quad (1.14)$$

$$\mu = \frac{p_\mu M_s^2}{\mu_0 \langle K \rangle} = \frac{p_\mu M_s^2 A^3}{\mu_0 x^2 K_1^4 D^6} \quad (1.15)$$

where,  $x$  denotes crystalline volume fraction,  $H_c$  is the coercivity,  $M_s$  saturation magnetisation,  $p_c$  and  $p_\mu$  - fitting parameters. According to the Herzer model, the anisotropy of nanocrystalline soft magnetic materials follows a  $D^6$  law [15]. It was observed that this  $D^6$  law was not applicable in the case of thin films. The films are a two dimensional structure and the confinement effect have to be considered. Accordingly the average anisotropy is represented as, [16]

$$\langle K \rangle = \frac{K_1^2 D^2}{A} \quad (1.16)$$

Therefore coercivity and permeability becomes

$$H_c = \frac{p_c K_1^2 D^2}{M_s A} \quad (1.17)$$

$$\mu = \frac{p_\mu M_s^2 A}{\mu_0 K_1^2 D^2} \quad (1.18)$$

Thus, for thin films coercivity follows a  $D^2$  law.

### 1.3.2 Metallic Glasses

Libermann *et al.* in 1976 developed a new amorphous alloy having Fe, Ni and P, by using a supercooled fast spinning wheel and this was named as metallic glasses or metglas [17]. These were commercialized in 1980s by allied signal. Different alloy compositions were developed. Metglas 2826 is a Fe based alloy having a composition of  $\text{Fe}_{40}\text{Ni}_{38}\text{Mo}_4\text{B}_{18}$ . This alloy has high permeability, high magnetic saturation, low magnetostriction and higher corrosion resistance. Many researchers have carried out studies on their crystallization kinetics, magnetic properties and microstructure [18-21]. Diverse reports exist regarding the crystallization kinetics of  $\text{Fe}_{40}\text{Ni}_{38}\text{Mo}_4\text{B}_{18}$ . Antonione *et al.* was the first to report the crystallization kinetics in 1978, according to which,  $\text{Fe}_{40}\text{Ni}_{38}\text{Mo}_4\text{B}_{18}$  follow a two stage crystallization at temperatures 703K and 777 K with activation energies 296 and 334  $\text{kJmol}^{-1}$  respectively [22]. Majumdar and Nigam observed three stage crystallization at temperatures 728K, 810K and 863K [23]. The findings of Cumbreira *et al.* were also in accordance with the three stage crystallization [24]. From XRD studies carried out by Mizglaski the first phase to crystallize is  $(\text{FeNi})_{23}\text{B}_6$  [25]. V S Raja *et al.* observed that  $\gamma$ -FeNiMo crystallizes via primary crystallization and fcc  $(\text{FeNi})_{23}\text{B}_6$  undergoes polymorphic crystallization [26]. Du *et al.* carried out studies on crystallization and microstructural analysis by Selected Area Electron Diffraction and observed that Fe-Ni crystallizes first and at higher temperatures  $(\text{FeNiMo})_{23}\text{B}_6$  phase is formed [19-20]. Hysen *et al.*

reported the crystallization of FeNiMo at 699K and  $(\text{FeNiMo})_{23}\text{B}_6$  at 809K [21]. R Krishnan *et al.* reported a magnetization value of 87 emu/g for  $\text{Fe}_{40}\text{Ni}_{38}\text{Mo}_4\text{B}_{18}$  ribbon [27]. Du *et al.* observed that the Fe-Ni phase enhances the magnetisation, while  $(\text{FeNiMo})_{23}\text{B}_6$  being a non magnetic phase degrades the soft magnetic properties of  $\text{Fe}_{40}\text{Ni}_{38}\text{Mo}_4\text{B}_{18}$  [20]. The variation of magnetic properties of  $\text{Fe}_{40}\text{Ni}_{38}\text{Mo}_4\text{B}_{18}$  with grain size was in accordance with the Herzer model [20]. The metallic glass  $\text{Fe}_{40}\text{Ni}_{38}\text{Mo}_4\text{B}_{18}$  have been used widely for various soft magnetic applications like memory elements, read and write heads, magnetostrictive sensors [28]. With the advent of miniaturization and Micro Electro Mechanical Systems (MEMS) and Nano Electro Mechanical Systems (NEMS) devices, the study of thin film forms of  $\text{Fe}_{40}\text{Ni}_{38}\text{Mo}_4\text{B}_{18}$  has gained momentum. From a fundamental perspective, thin films are an ideal template to study the effect of surface properties on magnetism. Hysen *et al.* and Senoy *et al.* carried out studies on  $\text{Fe}_{40}\text{Ni}_{38}\text{Mo}_4\text{B}_{18}$  thin films prepared by thermal evaporation. They also studied the role of thermal annealing on the magnetic properties [16, 29-31]. The as prepared films were amorphous in nature, and on annealing nanocrystallinity could be induced, which can tailor the magnetic properties. Senoy *et al.* have developed a magnetostrictive sensor based on  $\text{Fe}_{40}\text{Ni}_{38}\text{Mo}_4\text{B}_{18}$  [28]. Liang *et al.* developed a magnetoelastic sensor using FeNiMoB films prepared by co-sputtering [32]. Thus the study and development of devices based on FeNiMoB are still in its full bloom.

#### 1.4 MAGNETISM IN SPINELS

Spinel structures are categorized as having fcc cubic closed array of oxygen atoms with two interstitial sites-the tetrahedral vacancies, called A site, which has a tetrahedral coordination of oxygen atoms, and octahedral interstitials, that has a octahedral coordination of oxygen atoms and known as B sites [33].

## Chapter 1

Unit cell of spinel structure has 64A sites and 32B sites. They have the general formula  $MFe_2O_4$ , where M is a divalent metal [34-35]. Depending upon the charge state of ions occupying the A and B site, three types of spinels are defined:

- Normal Spinel: The divalent cation occupies the A site and trivalent cation occupies the B site. This can be represented by the formula  $[M^{2+}]_A [Fe_2^{3+}]_B O_4$ . Zinc ferrite is one of the normal spinel.
- Inverse spinel: The divalent cation occupies the B site and trivalent cation equally occupies the A and B site. This has the formula  $[Fe^{3+}]_A [M^{2+}Fe^{3+}]_B O_4$ .
- Mixed Spinel: In these kinds of spinels, the divalent and trivalent cations can occupy both the A and B sites. These spinels are represented by the formula  $[A^{2+}_{1-x}B^{3+}_x][A^{2+}_x B^{3+}_{2-x}]O_4$ . Here, x denotes the degree of inversion.

The magnetism in spinel structures depends on the type of spinel structure and the magnetic ions present in A and B sites. The interactions in spinel structures are indirect interactions mediated through oxygen atoms called as superexchange interaction. Three kind of superexchange interaction is observable in spinels: AOA, BOB and AOB. Among these exchange interactions the strongest is AOB, then BOB and AOA [2]. If magnetic ions are present only in A site, the interaction is  $J_{AA}$  and is known to be a weak interaction. If magnetic ions are present only in B site,  $J_{BB}$  interaction is dominant. The magnetic ions present in both A and B site, give rise to  $J_{AB}$  interaction resulting in good magnetic property of materials.

### 1.4.1 Zinc ferrite

Zinc ferrite is a normal spinel with  $Zn^{2+}$  occupying the A site and  $Fe^{3+}$  occupying the B site. The magnetic ion Fe is in B site, therefore the dominant

magnetic interaction is among  $\text{Fe}^{3+}$  ions in B site. The  $J_{\text{BB}}$  interaction is very weak and results in antiferromagnetic ordering and thus effectively no net magnetic moment is observed.

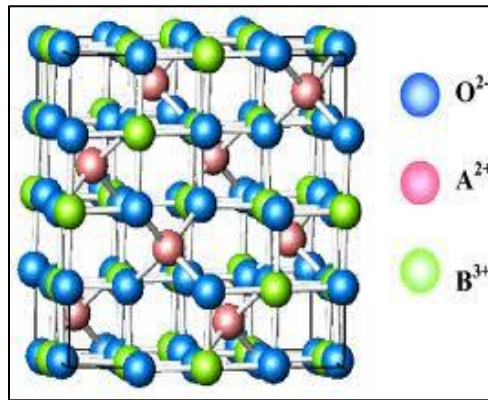


Fig. 13 Structure of spinel

Brockman *et al.* was the first to study the structure and magnetic property of zinc ferrite [36]. Neel temperature of zinc ferrite estimated by various methods was found to be at 10.5K [37-38]. Schiess *et al.* observed coexistence of long range and short range ordered antiferromagnetism below Neel temperature and short range ordered antiferromagnetism at temperatures much higher than the Neel temperature [39]. Kamazawa *et al.* carried out studies on single crystal zinc ferrite and concluded that zinc ferrite is a three dimensional frustrated magnet [40]. A weak ferromagnetic ordering in zinc ferrite has also been reported [37, 41].

The properties in nanoregime are entirely different from that of the bulk. Many groups have carried out structural, magnetic (both ac and dc measurements) and dielectric studies on nano zinc ferrite synthesized via different routes [42-49].

## Chapter 1

The remarkable fact is that zinc ferrite nano particles never show a consistent behavior. Depending upon the synthesis method, the properties can vary from antiferromagnetic to ferrimagnetic, superparamagnetic or spin glasses [46-47, 50-51]. Anantharaman *et al.* have carried out Mossbauer and Low Energy Ion Scattering (LEIS) studies on ultra fine zinc ferrites prepared by low temperature and high temperature methods [52-53]. They observed that zinc occupies the B site contrary to the conventional normal spinel structure and the amount of zinc substitution depends on the particle size. Mossbauer studies also confirmed the AOB interaction. Many studies carried out on nano zinc ferrite throw light on the fact that the blocking temperature gets enhanced from 10K [51]. Tung *et al.* studied the dependence of thermal annealing and observed that blocking temperature shifts to 150K with annealing which was attributed to cation redistribution [43]. Nuclear magnetic resonance (NMR) studies on nano zinc ferrite revealed the spin canting of Fe ions in B site, which is due to the fact that on cation redistribution the Fe ions in B site produces an antiferromagnetic ordering while the Fe ions among A and B site causes ferrimagnetic ordering [54].

Apart from nanosized zinc ferrite, thin films of zinc ferrite have also drawn attention of researchers and technologists. Studies on thin films of zinc ferrite by various techniques and different methods to modify the properties of thin films were reported [55-69]. Yamamoto *et al.* in 2001 deposited zinc ferrite thin films by Pulsed laser deposition (PLD) and observed that the films exhibited cluster glass behavior and studied the rate of deposition on the glass transition temperature [68]. Tanaka *et al.* prepared zinc ferrite thin films by sputtering and obtained room temperature ferrimagnetic behavior [56]. Nakashima *et al.* also observed room temperature ferrimagnetic behavior in zinc ferrite films deposited by sputtering and they carried out theoretical and experimental studies using

X-ray absorption near edge structure (XANES) and observed cation redistribution in zinc ferrite thin films [57, 70]. The effects of thermal annealing on the structural, topographical and magnetic properties were studied [61, 63, 71-72]. The interesting fact is that the results obtained by one kind of deposition cannot be reproduced by other method. The films deposited by sputtering yields room temperature ferrimagnetism, while that by PLD gives weak magnetic properties at room temperature [55, 57, 60, 67, 69]. Glassy behavior could be induced in films by using sputtering technique [57, 61]. These anomalies make zinc ferrite an interesting candidate to study.

Zinc ferrites are used in inductors, catalysts, high frequency systems and as gas sensors [73-74]. Zinc ferrites were found to be excellent sensors for ethanol [75]. The gas sensing properties depend on various factors like grain size, porosity and surface area [74]. Thin films form of zinc ferrite is an ideal template to study the properties and they are easier to integrate in various devices.

## **1.5 MAGNETISM AT FERROMAGNET (FM)- ANTIFERROMAGNET (AFM) INTERFACE- EXCHANGE BIAS:**

### **1.5.1 Phenomenon:**

When a ferromagnet and antiferromagnet form an interface, an interesting phenomenon called exchange bias is observed. This phenomenon results either in a hysteresis loop shift, or loop widening, when the FM-AFM system is field cooled below the Neel temperature of AFM. Loop shift or loop widening depends on the AFM anisotropy. The spin orientation and loop shift as a result of exchange bias is shown in Figure 14. The ferromagnet aligns along the applied field direction at room temperature while AFM spins are randomly aligned. When the system is field cooled below  $T_N$ , the AFM spins align antiparallel to each other. During this procedure, at the interface, the AFM spins are coupled by FM spins to

align parallel to FM. On reversing the magnetic field the AFM spins exerts an additional torque if the AFM anisotropy is sufficiently large, which the FM spins have to overcome. Thus a more negative field is required to make magnetization zero. When AFM anisotropy is small, both FM and AFM spins rotate on magnetic field reversal and this causes enhancement of hysteresis loop [76-78].

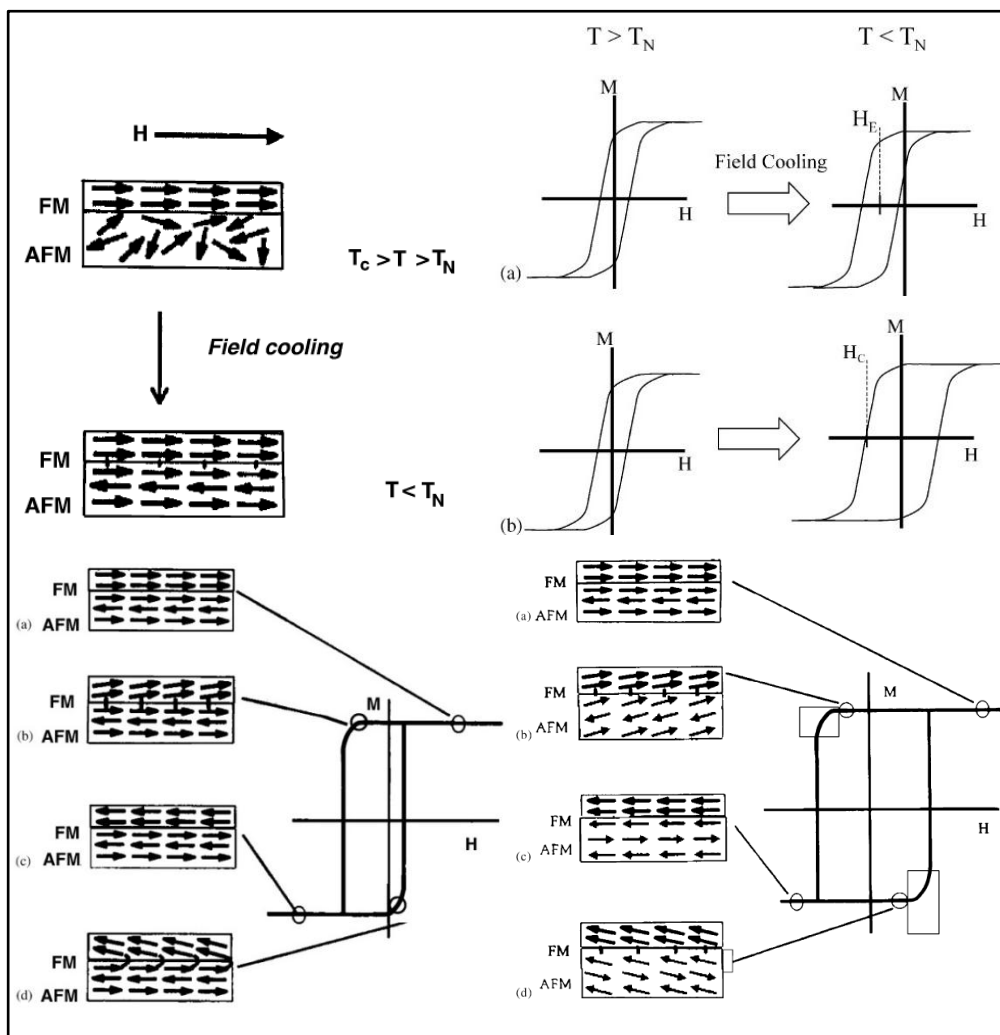


Fig. 14 Schematic of exchange bias [76]

### 1.5.2 Evolution of exchange bias:

In 1956 Meiklejohn and Bean reported “A new type of magnetic anisotropy has been discovered which is best described as an exchange anisotropy. This anisotropy is the result of an interaction between an antiferromagnetic material and a ferromagnetic material”[79]. They observed a loop shift in Co nanoparticle, and the exchange bias was due to FM-AFM interaction arising from the oxidation of Co which results in Co-CoO core shell structure. They assumed an ideal FM-AFM interface, that is, a smooth interface with uncompensated spins. The predicted exchange field according to his model was

$$H_E = \frac{J_i}{M_{FM} t_{FM}} \quad (1.19)$$

where,  $J_i$  is the interfacial exchange,  $M_{FM}$  is the magnetization of ferromagnet and  $t_{FM}$  is the thickness of ferromagnet. But the obtained experimental value of exchange bias was not in agreement with this model. Neel observed exchange bias in films of Co-CoO and Ni-NiO [77]. Most widely studied systems for exchange bias is FeNi as the ferromagnet, and FeMn as AFM [80-82]. Many studies on exchange bias with NiO, CoO, IrMn, Pt-Mn as AFM layers were reported [77].

However, the experimental results were not in accordance with the theoretical predictions. The first correlation between experimental and theoretical model was obtained with the development of domain wall model proposed by D Mauri in 1987 [83]. The formation of domain wall at the interface can minimize the interfacial exchange energy and thus stabilizes the system. According to this model, the exchange field was

$$H_E = 2 \frac{\sqrt{A_A K_A}}{M_{FM} t_{FM}} \quad (1.20)$$

## Chapter 1

where,  $A_A$  and  $K_A$  are the exchange stiffness and anisotropy of antiferromagnet. This theory was in agreement with the experimental results. Malozemoff discarded the concept of ideal compensated interface and proposed a random field model, wherein the interface had moment imbalance due to interfacial roughness and defects [84]. The exchange field is then influenced by the balance between applied field pressure  $2HM_{FTF}$  and the effective pressure from the interfacial energy difference  $\Delta\sigma$ .

$$H_E = \frac{\Delta\sigma}{2M_{FM}t_{FM}} \quad (1.21)$$

The exchange field calculation involves finding the interfacial energy difference between two ferromagnetic orientations and is thus given by,

$$H_E = \frac{2z\sqrt{AK}}{\pi^2 M_{FM}t_{FM}} \quad (1.22)$$

The Malozemoff model points out that the domain wall can be formed either in the ferromagnet or antiferromagnet depending on where the energy is lower. Malozemoff also studied the dependence of AFM layer thickness on the exchange bias properties [85]. According to him there exists a critical thickness of the order of domain wall width below which exchange field is observed given by,

$$t_{crit} = \frac{f_i\sqrt{A/K}}{4\sqrt{\pi}} \quad (1.23)$$

Koon *et al.* proposed a mechanism for exchange coupling at compensated interfaces [78, 86]. The magnetic frustration as a result of competing antiferromagnetic and ferromagnetic interaction results in a canted spin configuration. This gives rise to a perpendicular orientation of ferromagnetic spins relative to antiferromagnet easy axis. The exchange field is then given by,

$$H_E = \frac{\sigma}{2t_{FM}M} \sqrt{1 - \left(\frac{\sigma}{4J_2}\right)^2} \quad (1.24)$$

In 2000, Miltenyi studied the dependence of non magnetic dilution of AFM on the exchange bias properties of Co-CoO bilayers [87]. They observed that the exchange bias increases by a factor of 2-3. Diluting the antiferromagnet and then cooling the AFM below Neel temperature results in the formation of a domain wall. This energy increase due to the formation of domains can be minimized if the domain wall passes through the non magnetic defects. Therefore the dilution of AFM or creating defects at AFM results in the formation of domain walls. As the dilution enhances the exchange field, the formation of domain walls also enhances the exchange bias. This model is often regarded as a proof for the domain wall model. Thus the exchange field can be tuned by dilution or creating defects at the AFM.

In 2007, Mannan Ali observed exchange bias in spin glass (SG) [88]. He reported exchange bias in Co-CuMn bilayer. Interestingly many of the AFM systems like CuMn, AgMn in which exchange bias is observed was later shown to exhibit spin glass properties. All the exchange bias properties like field shift, dependence of exchange bias on cooling field observed in FM-AFM systems were found in FM-SG systems also. Usadel modeled the exchange bias due to FM-SG using Monte Carlo simulations [89]. Apart from the common binary alloys that shows exchange bias effects, many manganites, cobaltites and ferrites exhibiting exchange bias has been reported recently [90-94].

Most of the models on exchange bias involve an inverse dependence of exchange field on ferromagnet thickness, however the thickness dependence of AFM is not well clear. In FeNi-FeMn system, it was reported that the bias field

## *Chapter 1*

obeys a power law with AFM thickness as  $1/t^\lambda$ , where the exponent  $\lambda$  ranges from 0 to 0.3 [95]. The inverse relation of exchange bias with AFM thickness was also observed in various other systems namely IrMn<sub>3</sub>/Co, La<sub>2/3</sub>Ca<sub>1/3</sub>MnO<sub>3</sub>/La<sub>1/3</sub>Ca<sub>2/3</sub>MnO<sub>3</sub>, Ta/Py/IrMn/Pt [96-98]. In most of the studies carried out so far, the optimum thickness of the AFM layer is ~20 nm, the bias field disappears for thickness values greater than this optimum thickness [99]. In some other systems like CuMn-Co, it was observed that bias field increases with thickness and attains saturation [88-89]. The effect of thickness on the exchange bias is not universal and found to vary from system to system.

The phenomenon of exchange bias is of extensive interest as they can be used in various spin valves, magnetic tunnel junction and other spintronic devices and also due to the rich Physics involved [76, 100-101].

### **1.6 ION INTERACTION WITH MATERIALS**

Energetic ion beams offers wide possibilities for various studies in Physics and other branches of Science. How we view different sized objects around the universe and the solutions for such interrogations have led to the discovery of various instruments; for instance, microscopes to view micron sized objects like bacteria, telescopes to view distant stars and galaxies and electrons to view things at an atomic scale. What happens if we go still deeper inside nucleus? How can we probe the nucleus? High energy ions provide the retort. Since momentum and wavelength are inversely related, high energy particles have smaller wavelength which is comparable to the nuclear size and hence they are an ideal tool to inspect the nucleus. The high energy particles are produced with the help of particle accelerators. In the beginning of accelerator technology, high energy ions were used only in the field of nuclear physics and atomic physics. Later by 1960s scientists found the advantages of high energy ions in solid state physics also

[102]. The defects created by ion beams could change the properties of the materials and thus the journey of ion interaction with matter was on its way.

Energetic ion beams can be used effectively in materials science for diverse applications. Ion beams can be used for synthesis, modification and characterization of materials [102-103]. Energy of 1eV corresponds to 10000 K of temperature. Production of such high temperatures with other methods is in general, a tough challenge. The highly localized heating and sudden cooling upon energetic ion beam irradiation is extremely a non equilibrium process. This can cause drastic changes in the material properties [102]. Low energy ions of the order of few KeVs are used for material synthesis like in sputtering, ion beam assisted deposition etc. Energies of the order of few MeVs are used for material characterization. Various characterization techniques employing ions are Rutherford Backscattering Spectrometry (RBS), Elastic Recoil Detection Analysis (ERDA), Particle Induced X-ray Emission (PIXE), Nuclear Reaction Analysis (NRA), etc. High energetic ions of the order of few MeVs to hundreds of MeVs can be used for material modification, nanostructuring, etc. Ion beams are used widely in semiconductor industry for controlled and precise doping.

When ions pass through the material, they undergo various kinds of interaction and thus lose energy. The ions lose energy through collisions, columbic interaction and bremsstrahlung losses. The Coulomb interaction and associated energy loss is more predominant compared to other modes. Among the coulombic losses, incoming ion can lose energy either by elastic or inelastic interaction. Depending on the kind of interaction energy loss is classified as:

***Electronic energy loss:***

The incoming ions, on traversing through the target material, lose energy and slow down by inelastic collision with the electrons of the target atom. The

## *Chapter 1*

possible outcomes of these interactions are the ionization and/or excitation of target atoms. Here the energy transmitted to electrons through inelastic collisions is transferred to the material via electron phonon interaction. As it is evident from de Broglie hypothesis, the energy or momentum of incoming ion should be high enough to have such small wavelength for interaction with orbital electrons. The heavy energetic ion, on entering the medium, starts losing energy continuously via Coulomb interaction. Since the time of interaction is less, the energy loss per unit length will be minimum which maintains the ion trajectory straight. But as it traverse through the material, the ion counters multiple interactions and starts to slow down thereby increasing the number of interaction per unit length and this process continues. Finally the ions get buried in the material, if the range of ions is less than material thickness, depositing a major portion of energy near the end of ion trajectory and if range is higher ions pass through the material. Energy loss as a function of energy will have sharp peak near end known as Bragg peak, a typical characteristic of charged particle interaction with matter. Also it has been observed that the ion trajectory deviates from straight line near the end where energy remaining is less and the interaction is more.

### ***Nuclear energy loss:***

For lower energy regime, below a few hundred keV, the ions lose energy via elastic collision with the target atom. At lower energies, de Broglie wavelength of the incoming ion will be relatively high, comparable to atomic dimension and thus the prominent interaction can be visualized as atom-atom elastic collision mediated by repulsive potential between them. When atoms receive significant recoil energies, they will be removed from their lattice positions, and produce a cascade of further collisions in the lattice. In the case of low energy ions, the ion trajectory deviates largely from a straight line.

### **1.6.1 Swift Heavy Ions (SHI):**

Swift heavy ions are ions having energy greater than 1MeV/u. Their interaction is mainly via electronic energy loss. Two models namely Coulomb explosion and thermal spike model have been proposed to explain the interaction of swift heavy ions [102].

#### ***Coulomb Explosion model:***

An energetic ion ionizes the atoms in a cylindrical region along the ion path. Repulsive electrostatic forces, that is, the Coulomb force act during the period before charge neutrality is restored, giving rise to a violent explosion. The Coulomb explosion occurs, only if the charge neutralization time exceeds  $10^{-14}$  s. This phenomenon leads to the localized damage or change of the lattice within a narrow cylindrical zone in insulators and not in metals. In case of metals the charge neutralization time is less than  $10^{-14}$  s and therefore charges are neutralized before explosion. Coulomb explosion theory failed to explain the ion interaction in metals.

#### ***Thermal Spike model:***

In thermal spike model, it is assumed that when the temperature in the ion track exceeds the melting point of the material, a transient molten state is formed in a localized zone of few nanometers, existing for a short duration in typically ps time scale. The rapid thermal quenching of the hot cylindrical region results in an amorphous track along the ion path in a short span of time. This results in a modified material within the cylindrical region.

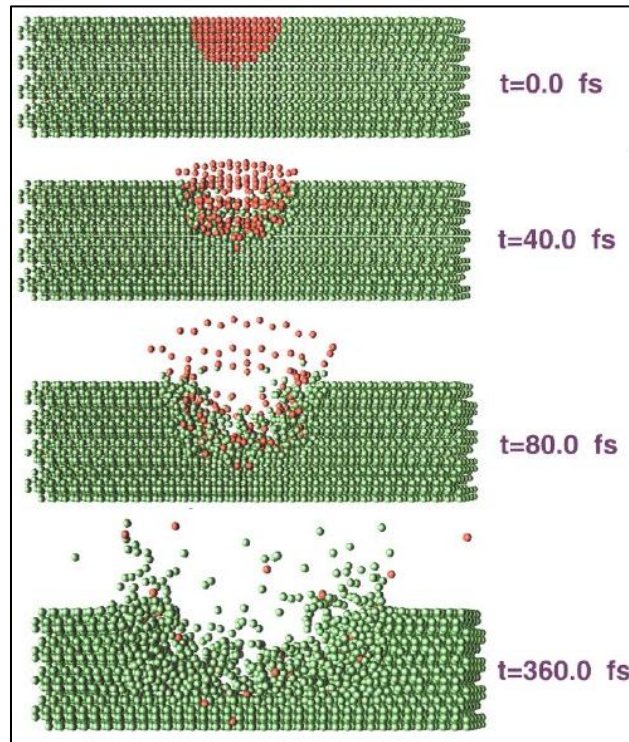


Fig. 15 Schematic of Coulomb explosion model [104]

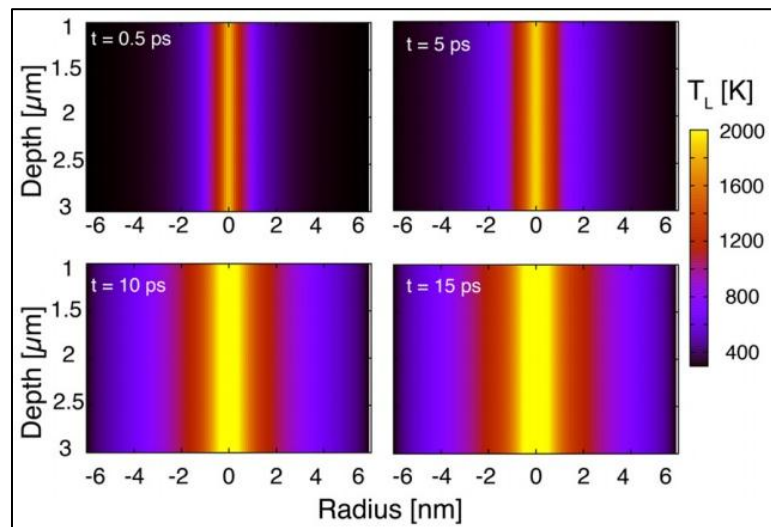


Fig. 16 Schematic of Thermal spike model [105]

### 1.6.2 Ion Beam Mixing

At the interface of two layers, passage of ions results in movement of atoms from one layer to the other forms a new mixed layer. This is referred to as ion beam mixing. When a film deposited on a substrate is irradiated with ions, at the interface of the film and substrate, ion beam mixing can take place. If we have a bilayer or multilayer film, ion irradiation causes mixing of different layers. The properties of mixed layer are different from that of individual layers. In the lower energies ion beam mixing is dominated by the nuclear energy loss and at higher energies by electronic energy loss. Ion beam mixing by swift heavy ions was first reported in Fe/Si multilayers by Dufour *et al.* [106]. The advantages of ion beam mixing are its spatial selectivity and thermodynamically immiscible systems can be mixed [102-103].

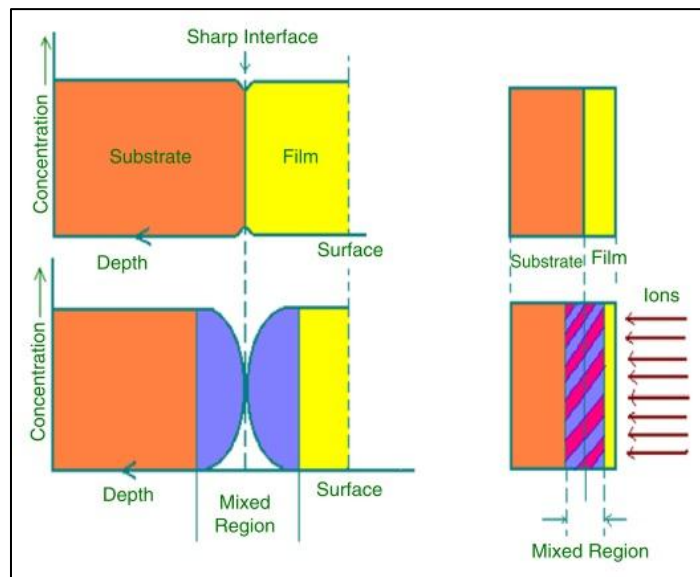


Fig. 17 Schematic of ion beam mixing [103]

## 1.7 MODIFICATION OF MAGNETIC PROPERTIES BY SHI

Swift heavy ions can be used effectively to alter the properties of the material. Even though the ion interaction in materials has ensued around 1960s, it is only recently that the role of ion beams on magnetic properties began to be perceived. The structural and topographical changes induced as a result of irradiation can influence the magnetic properties of the material. Ion irradiation can cause structural disorder, produce interstitial defects and introduces strain effects which can cause changes in magnetic anisotropy and magnetic order [107]. The irradiation effects carried out on permalloy thin films by Baglin *et al.* modified the anisotropy and magneto resistance [108]. Implanting Cr ions in NiFe alloys reduces the Curie temperature [109]. In FePt alloys which was non magnetic, ferromagnetism was induced as a result of ion irradiation [110]. Ion beam also finds application as a tool to create pattern in high density recording media [107]. In intermetallic alloys the crystalline state is weakly magnetic, while the amorphous state exhibits enhanced magnetisation as a result of local disorder which can localize the 3d electrons [111]. Amorphous tracks can be created by ion irradiation.

In soft magnetic alloys coercivity and anisotropy could be tailored by ion irradiation. Thin films based on metallic glasses were irradiated with swift heavy ion and the changes in topographical and magnetic properties have been studied [112-115]. Senoy *et al.* carried out irradiation studies on thermally evaporated Fe-Ni alloy thin films using 108MeV Ag ions. They observed that the surface roughness increases with ion fluence which in turn causes domain wall pinning resulting in an increased coercivity [115]. Geetha *et al.* carried out irradiation studies on CoFeSi films and an increase in roughness with ion fluence was observed. The stress relaxation at lower fluences reduced the coercivity and at

higher fluence the increase in density of pinning centers increase coercivity [114]. Hysen *et al.* observed an increase of surface roughness at lower fluence and then a decrease at higher fluence on metallic glass thin films as a result of irradiation. This is due to the interplay of ion induced sputtering, surface diffusion and volume diffusion [112].

SHI induced track formation in ferrites have been of great interest to researchers. Track formation occurs above a particular threshold value of electronic energy loss [111, 116]. Below this threshold, defects and disorders are produced as a result of ion irradiation. The formation of latent track as a result of ion irradiation was first observed in mica [116]. Among the magnetic oxides the track formation was reported in yttrium garnets [116]. Studer *et al.* observed a ferrimagnetic to paramagnetic transition in barium hexa ferrite and yttrium garnet irradiated with GeV Ar ions [117]. They observed a threshold electronic energy loss above which damage efficiency increases drastically and a high electronic energy loss where the damage effects gets saturated in yttrium garnets [118]. Chukalkin *et al.* reported ferrimagnetic transition of zinc ferrite under neutron irradiation [119]. Studer *et al.* reported in 1993 the irradiation induced by GeV energetic U, Kr and Xe ions in zinc ferrite spinels, which creates amorphous tracks and induces ferrimagnetic properties on zinc ferrite [120]. Zinkle *et al.* studied the effect of electronic energy loss on the track formation of  $\text{MgAl}_2\text{O}_4$  spinel [121]. A comparative study on the effect of 85 MeV oxygen ions on micron and nano sized strontium ferrite was carried out and the micron sized samples were more profound to irradiation induced damages than nano sized counterpart [122]. The effect of track induced stresses on the magnetic anisotropy and permeability of yttrium garnets was studied by Costantini *et al.* [123]. Irradiation induced modification on nanostructures of Ni-Zn ferrite, Mn-Zn ferrite, Mg-Mn

## Chapter 1

ferrites were reported and changes in magnetic properties is attributed to amorphisation and track formation [124-126]. The amorphisation in nickel ferrite thin films as a result of ion irradiation was studied [127]. Srivastava *et al.* reported that superparamagnetic state of zinc ferrite retains even after irradiation with 100 MeV oxygen ions [128]. J P Singh *et al.* studied the effect of oxygen irradiation on zinc ferrite nanostructures and formation of latent tracks of diameter 3nm; however the magnetic properties were found to decline with irradiation [129].

Exchange bias is an interface phenomenon and modification of interface can have a profound influence on the exchange bias properties. Ion irradiation can be used as an ideal tool to modify the interface. Mewes *et al.* reported suppression of exchange bias in FeNi-FeMn system by keV He ion irradiation [130]. Mougine *et al.* in 2001 put forward a theoretical model to explain the modification of exchange bias by ion irradiation [131]. According to the model, the exchange bias is directly proportional to the defects created at the AFM as a result of ion irradiation; as defects act as pinning centres for domain wall formation and thus can enhance the exchange bias effect. Also, exchange bias exponentially decay with the interface defects. The model is theoretically expressed as

$$\frac{H_{EB}}{H_{EBini}} = (1 \pm aptN) \times e^{-bN} \quad (1.25)$$

where,  $H_{EB}$  is the exchange bias field,  $H_{EBini}$  is the exchange bias field prior to irradiation,  $a$  is the efficiency of ions to create defects at the AFM and thus enhance the exchange field,  $p$  is the probability of atoms to be displaced by the incoming ion,  $t$  thickness of AFM,  $N$  is the ion dose and  $b$  is the efficiency of ions to modify the interface and thereby reduce exchange bias. Thus the ion induced modification of exchange bias is a competition between defects creation in AFM

and interface mixing [131-132]. This model agrees with the experimental results obtained for He ion irradiation on FeNi-FeMn systems [131]. Engel *et al.* reported the modification of exchange bias in FeNi-NiO system by He ion bombardment in an applied magnetic field [133]. The initial studies on exchange bias modification by low energy ions have been extended to spin valves and magnetic tunnel junctions [80-81, 134-137]. The time dependence of exchange bias after irradiation was also studied and modeled [138-140].

Ion irradiation offers wide possibilities to alter the magnetic properties by microstructural, magnetic and interface modification.

## **1.8 MOTIVATION AND OBJECTIVES**

Metallic glasses have attracted the attention of technologists because of their excellent soft magnetic properties compared to other conventional crystalline materials. From literature it is evident that the studies on bulk systems have been extensively pursued by researchers worldwide [5, 12, 141].  $\text{Fe}_{40}\text{Ni}_{38}\text{Mo}_4\text{B}_{18}$  belongs to the family of metallic glass, where Fe-Ni imparts magnetic properties, B aids in amorphisation and Mo act as a grain growth inhibitor. Thermal annealing induces nanocrystallinity in these alloys and their soft magnetic properties get enhanced [142]. The crystallization kinetics and magnetic properties of  $\text{Fe}_{40}\text{Ni}_{38}\text{Mo}_4\text{B}_{18}$  ribbon have been studied in detail by various researchers [19, 21, 143]. Studies on thin films of these materials assume significance as the magnetic properties of thin films are different from bulk and they can be integrated in to MEMS and NEMS devices. Earlier studies carried out in our lab on thin film forms of  $\text{Fe}_{40}\text{Ni}_{38}\text{Mo}_4\text{B}_{18}$  alloys by employing vacuum evaporation yielded films with excellent magnetic properties. However, the target composition could not be retained in the film [16, 30, 31]. As each element has its own contribution, retaining the composition of the target in the film is necessary

## *Chapter 1*

as the individual components play a very important part in deciding the overall magnetic properties of these films.  $\text{Fe}_{40}\text{Ni}_{38}\text{Mo}_4\text{B}_{18}$  system can act as an ideal template to study the role of target elements, crystallinity and surface morphology on the magnetic properties of thin films. The target elements can be retained by adopting Radio Frequency (RF) sputtering methods to fabricate thin films. Retaining the target elements in thin film form and the modification of their properties by thermal annealing is one of the objectives of the present study. The motivation behind such a study is based on the presumption that thermal annealing modifies the surface roughness and grain size which in turn alters the magnetic characteristics of the film.

Ferrites are an interesting class of candidates to study the magnetic properties, as the properties are highly structure sensitive and also because of their potential applications in areas like catalysts, sensors. Zinc ferrite is an antiferromagnet with a Neel temperature of 10K and the antiferromagnetism is attributed to its spinel structure [36]. However several anomalies exist in the magnetic properties of zinc ferrite. In the nano regime, Zinc ferrite can be superparamagnetic, ferrimagnetic or a spin glass depending on the synthesis method [46-48, 51]. Studies on thin films of zinc ferrite indicate that the film thickness, the synthesis method and annealing conditions greatly influence the magnetic behavior and the Neel temperature [55-57, 67]. A zinc ferrite thin film with excellent ferrimagnetic properties at room temperature is desirable for various applications. Fabrication of zinc ferrite film with room temperature ferrimagnetic property and its response to thermal annealing is another objective of the present study. The magnetic ordering of zinc ferrite at lower temperatures is also of interest from a fundamental perspective.

Exchange bias is a phenomenon observed at FM-AFM interfaces. The FM spins are pinned by AFM spins on field cooling below the Neel temperature of the antiferromagnet. As a result the hysteresis loop is shifted along the field axis. These kind of exchange coupled structures are highly desirable in spin valves, magnetic tunnel junctions and other spintronic devices [76]. Exchange bias is also observed in ferromagnetic-spin glass, ferrimagnetic-antiferromagnetic and even soft-hard magnetic systems [76, 88-89]. As FeNiMoB is a FM and zinc ferrite can be an AFM or SG, a bilayer system of FeNiMoB-Zinc ferrite could probably exhibit exchange bias. Exchange bias depends on FM-AFM thickness and the FM-AFM interface. Most of the studies of FM-AFM systems carried out so far is on ultra thin films with thickness typically ranging from ~1-20nm [80, 95]. The effect of thicker films on the exchange bias properties is never seen investigated thoroughly. So a systematic investigation is desirable in order to examine the possibilities of an exchange biased system consisting of a FM film like FeNiMoB and an AFM/SG like zinc ferrite. This is yet another motivation of the present study.

The film properties can be modified by thermal annealing and ion irradiation. Ions on traversing through a material lose energy by nuclear energy loss and electronic energy loss. Swift heavy ion (SHI) irradiation can alter magnetic properties of bulk materials as well as thin films [102]. The magnetic properties of thin films depend on various factors like composition, crystallinity, crystal structure, anisotropy, surface and interface roughness and any changes in the above properties can also bring in changes in their magnetic properties [112-114]. Swift Heavy ion irradiation can amorphise, recrystallize or create defects in materials. Ion irradiation studies on RF sputtered films of FeNiMoB are carried

## *Chapter 1*

out with a view to enhancing the magnetic properties. This is also an objective of the present study.

Ion irradiation in crystalline materials can create amorphous tracks within the material. Spinel structures are susceptible to track formation [111, 116, 120, 129]. The track formation and the resulting changes in room temperature and low temperature magnetic properties as a result of ion irradiation in zinc ferrite is of great interest. The interdependence of crystallinity with the nature of magnetism exhibited by these films is of fundamental interest. This is also an intended study in the present thesis.

The modification of interface by ion irradiation can induce substantial changes in the exchange bias. The ion induced modification of exchange bias is the interplay between the defect creation in AFM and ion beam mixing at the interface [131]. Most of the studies on ion induced modification of exchange biased systems carried out so far is in the low energy regime of the order of a few keVs where nuclear energy loss is predominant [130-131, 133]. At higher energies, the ions lose energy by electronic energy loss and swift heavy ion irradiation induced modification of exchange bias properties offers possibilities to model the dependence of exchange bias on electronic energy loss. The modification of exchange bias in FeNiMoB-zinc ferrite system by swift heavy ion irradiation is also another motivation.

Thus, the major objectives of the present study in a nut shell are the following.

1. To replicate the exact composition of  $\text{Fe}_{40}\text{Ni}_{38}\text{Mo}_4\text{B}_{18}$  in their thin film forms by RF sputtering.

2. To study the effect of thermal annealing on the structural and magnetic properties of RF sputtered FeNiMoB thin films.
3. To tailor magnetic characteristics of FeNiMoB thin films by swift heavy ion irradiation.
4. Preparation of zinc ferrite thin films by RF sputtering and conduct a detailed investigation of the mechanism responsible for magnetism in these films.
5. To create amorphous tracks in zinc ferrite thin films by swift heavy ion irradiation.
6. Fabrication of FeNiMoB – zinc ferrite bilayer film exhibiting exchange bias effect.
7. To study the modification of exchange bias in FeNiMoB – zinc ferrite bilayer film by Swift heavy ion irradiation.

**REFERENCES:**

- [1] Stephen Blundell, Magnetism in condensed matter, Oxford University press 2001
- [2] Nicola A Spaldin, Magnetic materials fundamentals and applications, Cambridge University press 2011
- [3] P. Weiss, J.Phys., **6** (1907) 661
- [4] W. Heisenberg, Z. Phys., **49** (1928) 619
- [5] Michael E Mchenry, Matthew A Williard, David E Laughlin, Prog. Mater. Sci, **44** (1999) 291
- [6] B D Cullity, C D Graham, Introduction to magnetic materials, John Wiley & sons, 2009

*Chapter 1*

- [7] M. Knobel, W. C. Nunes, L. M. Socolovsky, E. De Biasi, J. M. Vargas, J. C. Denardin, J. Nanosci. Nanotechnol. 8 (2008) 2836
- [8] K H Fischer, J. A. Hertz, Spin Glasses, Cambridge University Press, Cambridge, 1991
- [9] J A Mydosh, J. Magn. Magn. Mater., **157/158** (1996) 606
- [10] Clement W, Willens R H, Duwez P, Nature **187** (1960) 869
- [11] Herzer G, Proc. of the NATO Advanced Study Insititute on Magnetic Hysteresis in Novel Materials, 1996
- [12] Herzer G, Chapter 3, Handbook of magnetic materials, vol. 10, Elsevier 1997
- [13] Yoshizawa Y, Oguma S, Yamauchi K , J. Appl. Phys. **64** (1988) 6044
- [14] R. Alben, J. J. Becker, M. C. Chi, J. Appl. Phys. **49** (1978) 1653
- [15] G Herzer, IEEE Trans. Magn. **26** (1990) 1397
- [16] Hysen T, Deepa S, Saravanan S, Ramanujan R V, Avasthi D K, Joy P A, Kulkarni S D, Anantharaman M R **39** (2006) 1993
- [17] Libermann H., Graham C., IEEE Trans. Magn. **12** (6) (1976) 921
- [18] Du S W, Ramanujan R V, J. Magn. Magn. Mater. **292** (2005) 286
- [19] Du S W, Ramanujan R V, Mater. Sci. Eng. A **375** (2004) 1040
- [20] Du S W, Ramanujan R V, J. Non-Cryst. Solids **351** (2005) 3105
- [21] Hysen T, Senoy T and Anantharaman M R, J. Mater Sci **43** (2008) 635
- [22] Antonione C, Battezzati L, Lucci A, Riontino G, Venturelo G, Scr. Metall. **12** (1978) 1011
- [23] Majumdar AK, Nigam AK, J. Appl. Phys. **51**(1980) 4218
- [24] Cumbreira FL, Miranda H, Conde A, Marquez R, Vigier P, J. Mater. Sci. **17** (1982) 2677
- [25] Misglaski, J. Mater. Sci. **16** (1981) 3357

- [26] Raja VS, Kishore, Ranganathan S, Bull. Mater. Sci. **9** (1987) 207
- [27] R. Krishnan, Shiva Prasad, K. Branska, J. Appl. Phys. **50** (1979) 7639
- [28] Thomas S, Mathew J, Radhakrishnan P, Nampoori V P N, George a. K, Al-Harhi S H, Ramanujan R V, Anantharaman M R, Sens. Actuators A **161** (2010) 83
- [29] Senoy Thomas (2009) Fabrication of thin films and nano columnar structures of Fe-Ni amorphous alloys and modification of its surface properties by thermal annealing and swift heavy ion irradiation for tailoring the magnetic properties, PhD Thesis, Cochin University of Science and Technology, India
- [30] Thomas S, Al-Harhi S H, Sakthikumar D, Al-Omari I A, Ramanujan R V, Yasuhiko Yoshida, Anantharaman M R, J. Phys. D: Appl. Phys. **41** (2008)155009
- [31] Senoy Thomas, S H Al-Harhi, I A Al-Omari, R V Ramanujan, V Swaminathan, M R Anantharaman, J. Phys. D: Appl. Phys. **42** (2009) 215005
- [32] Cai Liang, Chinthaka Gooneratne, Dongkyu Cha, Long Chen, Yogesh Gianchandani, J. Appl. Phys. **112** (2012) 113912
- [33] E Muhammad Abdul Jamal (2009) Preparation and Characterization of Magnetic and Non-magnetic Nanosized Spinel Oxides, Nickel Nanoparticles and Nickel-Polymer Nanocomposites, PhD Thesis, Cochin University of Science and Technology, India
- [34] Mathew D S, Juang R S, Chem. Eng. J. **129** (2007) 51
- [35] Mahmoud Goodarz Naseri, Elias B. Saion, Chapter 13, Advances in Crystallization Processes, Intech 2012
- [36] F.G. Brockman, Phys. Rev. **77** (1950) 841

*Chapter 1*

- [37] B.N. Brockhouse, Phys. Rev. **94** (1953) 781
- [38] Hastings J. M., Corliss L. M., Phys. Rev. **102** (1956)14
- [39] W. Schiessl, W. Potzel, H. Karzel, M. Steiner, G. M. Kalvius, A Martin, M. K. Krause, I. Halevy, J. Gal W. Schafer, G. Will, M. Hillberg, R Wappling, Phys. Rev. B **53** (1996) 9143
- [40] Kamazawa K, Tsunoda Y, Kadowaki H, Kohn K, Phys. Rev. B **68** (2003) 024412
- [41] C.B.R. Jesus, E.C. Mendonça, L.S. Silva, W.S.D. Folly, C.T. Meneses, J.G.S. Duque, J. Magn. Magn. Mater. **350** (2014) 47
- [42] Lazarevic, C. Jovalekic, A. Milutinovic , D. Sekulic, V. N. Ivanovski, A. Recnik, B. Cekic, N. Z. Romcevic, J. Appl. Phys. **113** (2013) 187221
- [43] Tung L ., Kolesnichenko V, Caruntu G, Caruntu D, Remond Y, Golub V ., O'Connor C ., Spinu L, Physica B **319** (2002) 116
- [44] Sushant Singh , Naresh Kumar, Aashish Jha, Mohit Sahni, Richa Bhargava, Amit Chawla, R. Chandra, Sanjeev Kumar, S. Chaubey, J. Supercond. Nov. Magn. **27** (2013) 821
- [45] Mozaffari M, Arani M E, Amighian J, J. Magn. Magn. Mater. **322** (2010) 3240
- [46] Shenoy S D, Joy P A, Anantharaman M R, J. Magn. Magn. Mater. **269** (2004) 217
- [47] Souad Ammar, Noureddine Jouini<sup>1</sup>, Fernand Fievet, ZyedBeji, Leila Smiri, PhilippeMoline, Michel Danot, Jean-Marc Greneche, J. Phys.: Condens. Matter **18** (2006) 9055
- [48] Pradeep A., Priyadharsini P, Chandrasekaran G, J. Alloys Compd. **509** (2011) 3917
- [49] Jeyadevan B, Tohji K and Nakatsuka K, J. Appl. Phys. **76** (1994) 6325

- [50] Eun Jung Choi, Yangkyu Ahn, Eun Joo Hahn, J. Korean Phys. Soc. **53** (2008) 2090
- [51] Hofmann M, Campbell S J, Ehrhardt H, Feyerherm R, J. Mater. Sci. **39** (2004) 5057
- [52] Anantharaman M R, Jagatheesan S, Malini K., Sindhu S, Narayanasamy A., Chinnasamy C N, Jacobs J P, Reijne S, Seshan K, Smits R H H, Brongersma H H, J. Magn. Magn. Mater. **189** (1998) 83
- [53] Anantharaman M R, Reijne S, Jacobs J P, Brongersma H H, J. Mater. Sci. **4** (1999) 4279
- [54] Shim J, Lee S, Park J, Han S-J, Jeong Y H, Cho Y W, Phys. Rev. B **73** (2006) 064404
- [55] Bohra M, Prasad S, Kumar N, Misra D S, Sahoo S C, Venkataramani N, Krishnan R Appl. Phys. Lett. **88** (2006) 262506
- [56] Katsuhisa Tanaka, Seisuke Nakashima, Koji Fujita, Kazuyuki Hirao, J. Phys.: Condens. Matter **15** (2003) L469
- [57] Seisuke Nakashima, Koji Fujita, Katsuhisa Tanaka, Kazuyuki Hirao, J. Phys.: Condens. Matter **17** (2005) 137
- [58] Katsuhisa Tanaka, Seisuke Nakashima, Koji Fujita, Kazuyuki Hirao, J. Appl. Phys. **99** (2006) 106103
- [59] Sultan M, Singh R, J. Appl. Phys. **105** (2009) 07A512
- [60] Yuan-Chang Liang, Hao-Yuan Hsia, Nanoscale Res. Lett. **8** (2013) 537
- [61] Nakashima S, Fujita K, Tanaka K, Hirao K, Yamamoto T, Tanaka I, J. Magn. Magn. Mater. **310** (2007) 2543
- [62] Timopheev A. A., Azevedo A. M, Sobolev N A., Brachwitz K, Lorenz M, Ziese M, Esquinazi P, Grundmann M, Thin Solid Films **527** (2013) 273

*Chapter 1*

- [63] Li G, Zhu X, Song W, Yang Z, Dai J, Sun Y, Fu Y, *J. Am. Ceram. Soc.* **94** (2011) 2872
- [64] Suzuki Y, van Dover R B, Gyorgy E M, Phillips J M, Korenivski V, Werder D J, Chen C H, Cava R J, Krajewski J J, Peck W F, Do K B, *Appl. Phys. Lett.* **68** (1996) 714
- [65] Sultan M, Singh R, *J. Phys. D: Appl. Phys.* **42** (2009) 115306
- [66] Guo D, Jiang C, Fan X, Xue D, *Appl. Surf. Sci.* **307** (2014) 576
- [67] Raghavender A. T, *Mater. Lett.* **65** (2011) 3636
- [68] Yamamoto Y, Tanaka H and Kawai T, *Jpn J. Appl. Phys., Part 2* **40** (2001) L545
- [69] Murtaza Bohra , Shiva Prasad , N. Venkataramani , S. C. Sahoo , Naresh Kumar, R. Krishnan, *IEEE Trans. Magn.* **49** (2013) 4249
- [70] Nakashima S, Fujita K, Tanaka K, Hirao K, Yamamoto T, Tanaka I, *Phys. Rev. B* **75** (2007) 174443
- [71] Guo D, Zhu J, Yang Y, Fan X, Chai G, Sui W, Zhang Z, Xue D, *J. Appl. Phys.* **107** (2010) 043903
- [72] Raghavan L, Pookat G, Thomas H, Ojha S, Avasthi D K, Anantharaman M R, *J. Magn. Magn. Mater.* **385** (2015) 265
- [73] Valenzuela R, *Phys. Res. Int.* (2012) 591839
- [74] Gadkari A B, Shinde T J and Vasambekar P N, *IEEE Sens. J.* **11** (2011) 849
- [75] Rezlescu N, Rezlescu E, Tudorache F and Popa P D *Rom. Rep. Phys.* **61** (2009) 223
- [76] Nogués J, Sort J, Langlais V, Skumryev V, Suriñach S, Muñoz J S and Baró M D, *Phys. Rep.* **422** (2005) 65
- [77] A.E. Berkowitz, K. Takano, *J. Magn. Magn. Mater.* **200** (1999) 552
- [78] R L Stamps, *J. Phys. D: Appl. Phys.* **33** (2000) R247

- [79] W.H. Meiklejohn, C.P. Bean, Phys. Rev. **102** (1956) 1413
- [80] Mewes T, Roos B F P, Demokritov S O, Hillebrands, J. Appl. Phys., **87** (2000) 5064
- [81] A. Mougín, S. Poppe, J. Fassbender, and B. Hillebrands, G. Faini, u ebels, M. Jung, D. Engel, A. Ehresmann, H. Schmoranzler, J. Appl. Phys., **89** (2001) 6606
- [82] A. V. Svalov, P. A. Savin, V. N. Lepalovskij, A. Larranaga, V. O. Vas'kovskiy, A. Garcia Arribas, and G. V. Kurlyandskaya AIP Adv. **3** (2013) 092104
- [83] Mauri D, Siegmann H C, Bagus P S, Kay E, J. Appl. Phys. **62** (1987) 3047
- [84] A P Malozemoff, J. Appl. Phys. **63** (1988) 3874
- [85] A. P. Malozemoff, Phys. Rev. B **37** (1988) 7673
- [86] N C Koon, Phys. Rev. Lett. **78** (1997) 4865
- [87] Miltenyi P, Gierlings M, Keller J, Beschoten B, Guntherodt G, Nowak U, Usadel K, Phys. Rev. Lett. **84** (2000) 4224
- [88] Ali M, Adie P, Marrows C H, Greig D, Hickey B J, Stamps R L, Nat. Mater. **6** (2007) 70
- [89] Usadel K D, Nowak U, Phys. Rev. B **80** (2009) 014418
- [90] S Giri, M Patra, S Majumdar, J. Phys.: Condens. Matter **23** (2011) 073201
- [91] Dong xing Zheng, Mingyu Sun, Dong Li, Peng Li, Chao Jin, Haili Bai, Europhys. Lett., **110** (2015) 27005
- [92] C. He, A. J. Grutter, M. Gu, N. D. Browning, Y. Takamura, B. J. Kirby, J. A. Borchers, J.W. Kim, M.R. Fitzsimmons, X. Zhai, V.V. Mehta, F. J. Wong, Y. Suzuki, Phys. Rev. Lett. **109** (2012) 197202
- [93] D. Niebieskikwiat, M. B. Salamon, Phys. Rev. B **72** (2005) 174422

*Chapter 1*

- [94] S Thomas, G Pookat, S S Nair, MDaniel, B Dymerska, A Liebig, S H Al-Harthi, R V Ramanujan, MR Anantharaman, J Fidler and MAlbrecht, J. Phys.: Condens. Matter **24** (2012) 256004
- [95] Sang H, Du Y W, Chien C L, J. Appl. Phys. **85** (1999) 4931
- [96] Yanes R, Jackson J, Udvardi L, Szunyogh L, Nowak U, Phys. Rev. Lett. **111** (2013) 217202
- [97] Kobrinskii A., Goldman A., Varela M, Pennycook S, Phys. Rev. B **79** (2009) 094405
- [98] Baltz V, Sort J, Landis S, Rodmacq B, Dieny B, Phys. Rev. Lett. **94** (2005) 117201
- [99] Demirci E, Öztürk M, Topkaya R, Kazan S, Akdoğan N, Obaida M, Westerholt K, J. Supercond. Nov. Magn. **25** (2011) 2591
- [100] R. Morales, M. Kovylyna, Ivan K. Schuller, A. Labarta, X. Batlle, Appl. Phys. Lett. **104**, (2014) 032401
- [101] A. Scholl, M. Liberati, E. Arenholz, H. Ohldag, J. Stohr, Phys. Rev. Lett. **92** (2004) 247201
- [102] D K Avasthi, G K Mehta, Swift heavy ions for materials engineering and nanostructuring, Springer series 2011
- [103] Jain I P and Agarwal G, Surf. Sci. Rep. **66** (2011) 77
- [104] Cheng H, Gillaspay J, Phys. Rev. B **55** (1997) 26
- [105] Aumayr F, Facsko S, El-said A S, Trautmann C, Schleberger M J. Phys.: Condens. Matter **23** (2011) 393001
- [106] Ph. Bauer, C. Dufour, C. Jaouen, G. Marchal, J. Pacaud, J. Grilhé, and J. C. Jousset, J. Appl. Phys. **81** (1997) 116
- [107] John E.E. Baglin, Chapter 3, Engineering Thin Films and Nanostructures with Ion Beams, Taylor and Francis, 2005

- [108]J.E.E. Baglin, M.H. Tabacniks, R. Fontana, A.J. Kellock and T.T. Bardin, Mater. Sci. Forum **248** (1997) 87
- [109]L. Folks, R. Fontana, B. Gurney, J. Childress, S. Maat, J. Katine, J.E.E. Baglin, A. Kellock and P. Saunders, J. Phys. D: Appl. Phys. **36** (2003) 2601
- [110]S. Maat, A.J. Kellock, D. Weller, J.E.E. Baglin and E.E. Fullerton, J. Magn. Mater. **265** (2003) 1
- [111]J P Nozieres, M. Ghidini, N.M. Dempsey, B. Gervais, D. Givord, G. Suran, J.M.D. Coey, Nucl. Instrum. Methods Phys. Res. Sect. B, **146** (1998) 250
- [112]Thomas H, Thomas S, Ramanujan R V, Avasthi D K, Omari I A, Al-harathi S, Anantharaman M R, Nucl. Instrum. Methods Phys. Res. Sect. B **287** (2012) 85
- [113]Hysen T, Geetha P, Al-Harathi S, Al-Omari I A., Lisha R, Ramanujan R V, Sakthikumar D, Avasthi D K, Anantharaman M R, J. Magn. Mater. **372** (2014) 224
- [114]Pookat G, Hysen T, Al-harathi S H, Al-omari I A, Lisha R, Avasthi D K, Anantharaman M R, Nucl. Instrum. Methods Phys. Res. Sect. B **310** (2013) 81
- [115]Thomas S, Thomas H, Avasthi D K, Tripathi A., Ramanujan R V., Anantharaman M R, J. Appl. Phys. **105** (2009) 033910
- [116]M. Toulemonde, S. Bouffard, F. Studer, Nucl. Instrum. Methods Phys. Res. Sect. B **91**(1994) 108
- [117]F. Studer, N. Nguyen, G. Fuchs, M. Toulemonde, Hyperfine Interact. **29** (1986) 1287
- [118]Studer F, Houpert C, Pascard H, Spohr R, Vetter J, Fan J Y, Toulemonde M, Radiat. Eff. Defects Solids **116** (1991) 59

*Chapter 1*

- [119] Yu.G. Chukalkin, B.N. Goshchitskii, S.F. Dubinin, S.K. Sidorov, V.V. Petrov, V.D. Parkhomenko, V.G. Vologin, *Phys. Status Solidi* **A28** (1975) 345
- [120] Studer F, Houpert C, Groult D, Meftah A, Toulemonde M, Cedex C, *Nucl. Instrum. Methods Phys. Res. Sect. B* **82** (1993) 91
- [121] S.J. Zinkle, V. A. Skuratov, *Nucl. Instrum. Methods Phys. Res. Sect. B* **141** (1998) 737
- [122] Shinde S R, Bhagwat A, Patil S I, Ogale S B, Mehta G K, Date S K, Marest G J. *Magn. Mater.* **186** (1998) 342
- [123] Costantini J M, Studer F, Peuzin J C, *J. Appl. Phys.* **90** (2001) 126
- [124] Sharma S K, Kumar R, Siva Kumar V V, Knobel M, Reddy V R, Gupta A., Singh M, *Nucl. Instrum. Methods Phys. Res. Sect. B* **248** (2006) 37
- [125] Kumar R, Sharma S K, Dogra A, Siva Kumar V V., Dolia S N, Gupta A., Knobel M, Singh M, *Hyperfine Interact.* **160** (2005) 143
- [126] Rao B P, Rao K H, Subba Rao P S V, Mahesh Kumar A., Murthy Y L N, Asokan K, Siva Kumar V V, Kumar R, Gajbhiye N S, Caltun O F, *Nucl. Instrum. Methods Phys. Res. Sect. B* **244** (2006) 27
- [127] Dixit G, Singh J P, Srivastava R C, Agrawal H M, *Nucl. Instrum. Methods Phys. Res. Sect. B* **269** (2011) 133
- [128] Srivastava R C, Singh J P, Agrawal H M, Kumar R, Tripathi A, Tripathi R P, Reddy V R, Gupta A, *J. Phys. Conf. Ser.* **217** (2010) 012109
- [129] Pal J, Dixit G, Kumar H, Srivastava R C, Agrawal H M, Kumar R, *J. Magn. Mater.* **352** (2014) 36
- [130] Mewes T, Lopusnik R, Fassbender J, Hillebrands B, Jung M, Engel D, Ehresmann A, Schmoranzler H, **1057** (2014) 8

- [131]Mougin A., Mewes T, Jung M, Engel D, Ehresmann A., Schmoranzer H, Fassbender J, Hillebrands B, Phys. Rev. B **63** (2001) 060409
- [132]Poppe S, Fassbender J, Hillebrands B, Europhys. Lett. **66** (2004) 430
- [133]Engel D, A. Kronenberger, M. Jung, H. Schmoranzer, A. Ehresmann, A. Paetzold, K.Roll, J. Magn. Mater. **263** (2003) 275
- [134]Schmalhorst J, Höink V, Reiss G, Engel D, Junk D, Schindler A, Ehresmann A, Schmoranzer H, J. Appl. Phys. **5556** (2006) 1
- [135]D. Engel, I. Krug, H. Schmoranzer, A. Ehresmann, A. Paetzold, K. Röhl, B. Ocker, W. Maass J. Appl. Phys. **94** (2003) 5925
- [136]Fassbender J, Poppe S, Mewes T, Juraszek J, Hillebrands B, Barholz K-U, Mattheis R, Engel D, Jung M, Schmoranzer H, Ehresmann A., Appl. Phys. A. **77** (2003) 51
- [137]Morales R, Kovylyna M, Schuller I K, Labarta A., Batlle X, Appl. Phys. Lett. **104** (2014) 032401
- [138]A. Ehresmann, D. Junk, D. Engel, A. Paetzold, K. Röhl, J. Phys. D **38** (2005) 801
- [139]Arno Ehresmann, Christoph Schmidt, Tanja Weis, Dieter Engel, J. Appl. Phys. **109** (2011) 023910
- [140]Christoph Schmidt, Tanja Weis, Dieter Engel, Arno Ehresmann, J. Appl. Phys. **110** (2011) 113911
- [141]G. Herzer, J. Magn. Mater. **294** (2005) 99
- [142]S. W. Du, R. V. Ramanujan, J. Metastable Nanocryst. Mater. **23** (2005) 207
- [143]R. V. Ramanujan, S. W. Du. J. Alloys Compd. **425** (2006) 251

*Chapter 1*

## Chapter 2

### Experimental Methods

- 2.1 Synthesis of Nanomaterials
- 2.2 Thin Film Deposition
- 2.3 Ion Irradiation Facility
- 2.4 Rutherford Backscattering Spectrometry (RBS)
- 2.5 X-Ray Reflectivity (XRR)
- 2.6 X-Ray Diffractometer (XRD)
- 2.7 Glancing Angle X-Ray Diffractometer (GXRD)
- 2.8 Transmission Electron Microscope (TEM)
- 2.9 Selected Area Electron Diffraction (SAED)
- 2.10 X-ray Photoelectron Spectroscopy (XPS)
- 2.11 Atomic Force Microscope (AFM)
- 2.12 Vibrating Sample Magnetometer (VSM)
- 2.13 Superconducting Quantum Interference Device (SQUID)

*Chapter 2*

The advent of nanotechnology demands fine and precise analytical tools. It is extremely important to know the underlying Physics and the experimental details involved while doing research. This chapter is devoted to the various experimental and analytical techniques used for the present study. The chapter begins with synthesis of nanomaterials and thin films, and then the structural characterizations like XRD, SAED are discussed. RBS, XRR, XPS, TEM, AFM, VSM and SQUID are also detailed.

## **2.1 SYNTHESIS OF NANOMATERIALS**

Nanomaterials are materials with particle size of the order of few nanometers. Two different approaches are used for nano synthesis:

***Top down approach:*** The bigger particles are made into smaller and smaller by various methods like mechanical or ball milling method.

***Bottom up approach:*** The material is synthesized by atom by atom growth. Eg: chemical methods, thin film deposition etc.

Nano materials can be prepared by chemical reaction starting from the appropriate precursors. Various chemical methods widely employed for nano material synthesis are coprecipitation method, sol gel auto combustion, microemulsion, hydrothermal methods etc. In the present study, we have adopted sol gel auto combustion method which will be detailed here.

### **2.1.1 Sol gel auto combustion**

Sol gel method is an outstanding method for the synthesis of hybrid nanoparticles and nanocomposites. The sol gel route involves preparation of sol, successive gelation and solvent removal. In this method, the desired salts are first dissolved in an organic solvent like ethylene glycol or citric acid. Once the salts are dissolved, the solution is heated at 60<sup>0</sup>C or 70<sup>0</sup>C to form a thick sol. The obtained sol is heated at a temperature of around 120<sup>0</sup>C until combustion took

place, thereby removing the water content. The obtained powder is then sintered at very high temperatures to obtain phase pure samples. The organic solvents like ethylene glycol or citric acid act as combustion agents. Sol gel method has been reported to be excellent for the synthesis of various ferrites. It can provide homogeneous ultra fine nanopowders [1].

## 2.2 THIN FILM DEPOSITION

Thin films are nanostructures having a backing material and with thickness in the nano regime. The properties of thin films depend on the substrate, deposition methods, deposition conditions like pressure, temperature, atmosphere etc. A thin film evolves through the following stages: Nucleation, island growth, coalescence of islands, formation of polycrystalline islands and channels, development of continuous structure and thickness growth [2]. Nucleation is the starting stage of film growth. The individual atoms deposited on the substrate combines to form adatom. These adatoms diffuse through the substrate and the film growth takes place [2].

The different mechanisms for the growth of films (figure 1) on a substrate are [2];

***Volmer Weber island growth:*** In this type of film growth, the atoms are more strongly bound to each other than to the substrate. Thus, small clusters get nucleated to the substrate and forms islands.

***Frank Vander Merwe layer growth:*** The atoms condense on to the substrate and form a complete monolayer on the substrate. This happens when the atoms are more strongly bound to substrate.

***Stranski Krastanov layer plus island growth:*** This growth mode is a combination of layer and island growth. Initially layer is formed and then island formation takes place.

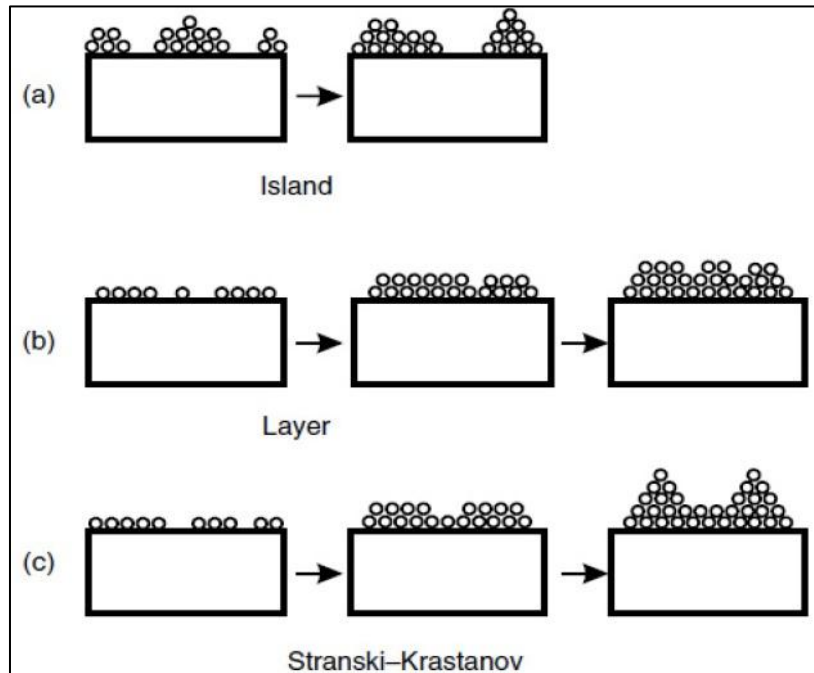


Fig. 1 Mechanisms of film growth [2]

Thermal evaporation, Pulsed Laser Deposition, sputtering, spray pyrolysis are the common methods of thin film deposition. In the present study sputtering method was adopted and will be described in detail.

### 2.2.1 Sputtering

Sputtering refers to the process of ejection of atoms from a solid surface as a result of ion bombardment. Sputtering is a physical vapor deposition process; the ions hit the target material which acts as cathode and the ejected atoms are deposited on a substrate which acts as anode. The whole process takes place in vacuum and when the required pressure is reached, inert gas is flowed in to the chamber and the electric field applied produces a plasma region where the positive ions are generated. These positive ions are attracted to the negative

Chapter 2

cathode where we have the target and collision of ions with target takes place. The momentum transfer as a result of collision ejects atoms from the material and they are subsequently deposited on the substrate. Two kinds of sputtering are commonly used DC and RF. In DC mode a voltage of 2-5kV is applied. DC sputtering cannot be used to deposit non conducting materials. In that case RF sputtering is the choice. In RF sputtering, a RF signal is used to generate the plasma. Schematic of sputtering is shown in figure 2. The sputter deposition takes place when target is negative [2].

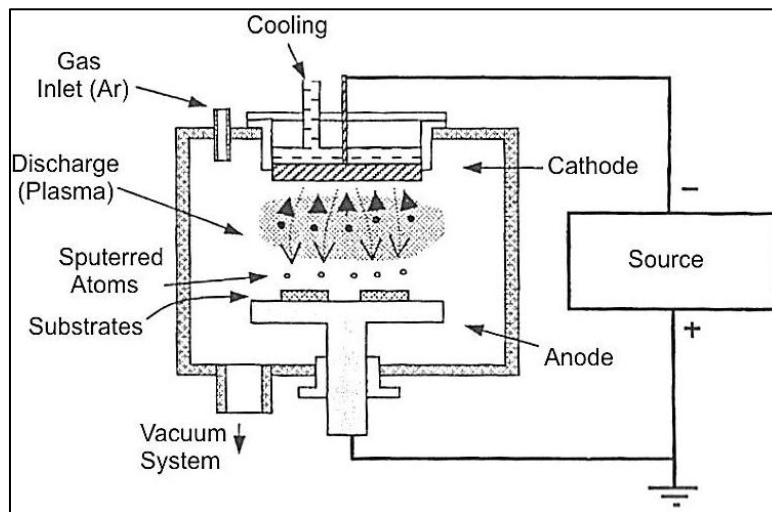


Fig. 2 Schematic of sputtering process [2]

Quantitatively, sputtering process is characterized by sputtering yield which is defined as the ratio of atoms sputtered to the number of particles incident on the target. Sputtering yield  $Y$  is given by,

$$Y = \frac{3\alpha}{4\pi^2} \frac{4m_1m_t}{(m_1 + m_t)^2} \frac{E}{U} \quad (2.1)$$

where,  $m_1$  and  $m_t$  are atomic mass of incident ion and target,  $U$  is the binding energy of surface atom of target,  $E$  is the energy of incident ion,  $\alpha$  is the parameter that depends on ratio of mass of target atom and incident ion [2].

Sputtering method is best suited to deposit alloys as the thin films deposited by sputtering retain the target composition. Suppose the target is an alloy represented by ABABABAB. If sputtering yield of A is greater than that of B, A atoms are sputtered. The target is now enriched with B, so next B atoms get sputtered. This cycle goes on and finally we obtain a film that has close resemblance to the target composition.

In the present study, thin films were deposited using a home made set up of sputtering unit at Inter University Accelerator Centre (IUAC), New Delhi. The system uses indigenously developed 500 W, 13.56 MHz with matching network as RF power supply. The vacuum system includes Turbo pump used to produce clean vacuum, backed by scroll pump.

### **2.3 ION IRRADIATION FACILITY**

The heavy ion irradiation experiment was carried out using 15 UD Pelletron accelerator at Inter University Accelerator Centre (IUAC), New Delhi. This is one of the two high energy Pelletron accelerators available, at present, in the country. A detailed description of the facility is given in the following section.

#### **2.3.1 Pelletron accelerator**

The 15 UD Pelletron accelerator at IUAC, New Delhi, is an electrostatic tandem accelerator capable of accelerating a wide range of ions, from proton to uranium up to an energy of about 200 MeV depending upon the ion species. The accelerator is installed in vertical configuration in an insulating tank of length 26.5 m and diameter 5.5 m, filled with SF<sub>6</sub> gas. The high dielectric strength and

## *Chapter 2*

high recombination rate of SF<sub>6</sub> make it an ideal medium for electrical insulation. The schematic diagram of the Pelletron accelerator is shown in figure 3.

The heavy ions of required species are produced by cesium sputtering. The source is named as Multi Cathode Source of Negative Ions by Cesium Sputtering (MC-SNICS). Inside the source volume, cesium vapours are ionized and collimated to target material, elemental or compound form of ion species; with an electrostatic field to sputter out the ions (it may be positive, negative or neutral). Later the negative ions are extracted by an extractor field (electrostatic) and transported to beam line with a pre-acceleration giving ~300keV energy. These negative ions are mass analyzed using the 90<sup>0</sup> injector magnet which bends the ions by 90<sup>0</sup> in vertical direction down to the accelerating column. Inside the vertical accelerating tank a high voltage terminal is located at the center. The terminal can be charged to potential as high as 15 MV using a pair of charging units consisting of a chain of pellets interconnected by nylon, hence the name Pelletron. The central potential is subdivided using a series of high resistors and a gradient is generated from terminal region to ground. Altogether, there are 30 units with 1 MV potential difference located 15 on either sides of the terminal. The injected negative ions get accelerated due to the increasing field up to terminal. At the terminal section, stripper foils of carbon are placed on the beam path which strips out electrons and convert it into positive ions having a distribution of charge states varying from 1+ to Z. These ions, being positive, are repelled by the terminal potential and thus gain another stage of acceleration and energy boosting [3].

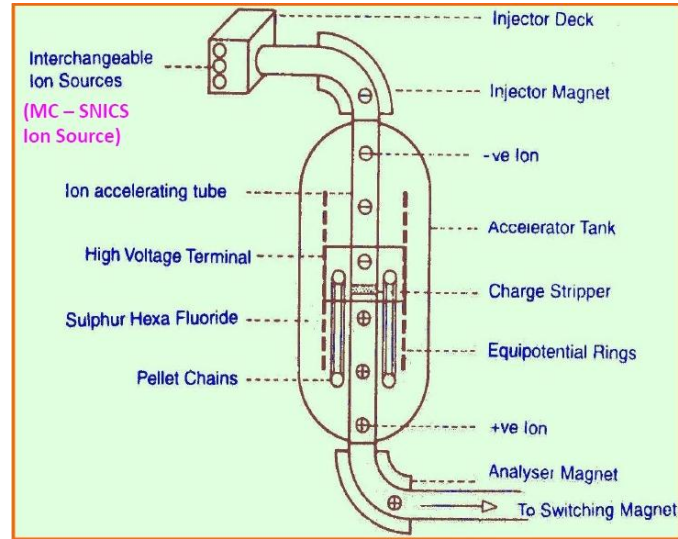


Fig. 3 Schematic of pelletron accelerator [3]

The energy of ions obtained from the pelletron accelerator is given by,

$$E = E_{inj} + (1 + q)V \quad (2.2)$$

where,  $E_{inj}$  is the energy from the source,  $q$  is the charge state of ion after stripping and  $V$  is the terminal voltage. The beam of required species and required energy is bend to horizontal direction using another bending magnet. The magnetic field can be tuned such that a particular charge state, and hence energy can be selected. This high energy beam is further switched into a specific beam line using a switcher magnet following magnetic Lorentz formula. The entire system follows Computer Automated Measurement And Control (CAMAC) standard which helps to monitor and control their performance from a remote location.

In the present study irradiation is carried out using 100 MeV Ag ions with different fluences. Fluence is defined as the number of ions impinging on the sample per unit area.

## Chapter 2

$$fluence = \frac{n}{A} \quad (2.3)$$

n is the number of ions and is related to the ion charge q.

$$q = ne \quad (2.4)$$

Ion current I is,

$$I = \frac{q}{t} \quad (2.5)$$

Therefore,

$$n = \frac{It}{e} \quad (2.6)$$

where, t is the time and e is the electronic charge.

Thus fluence can be related to time of irradiation and is given by

$$t = \frac{fluence \times A}{6.25 \times 10^9 \times I} \quad (2.7)$$

The current of ion beam from pelletron accelerator is denoted in particle nano Amperes (pnA).

### 2.4 RUTHERFORD BACKSCATTERING SPECTROMETRY (RBS)

The history of Rutherford backscattering can be traced back to 1911, when Rutherford conducted his gold foil experiment which led to the breakthrough discovery of nucleus. Many years later, the same mechanism is used as an analytical tool for material characterization in the form of RBS, which was first described by Rubin *et al.* in 1957. Nowadays, RBS is a widely used nuclear tool for analyzing thin films; which can give information about the film thickness, composition and elemental depth profile [4, 5].

In RBS, monoenergetic particles of the incident beam collide with the nuclei of the target atoms and the backscattered ions are analyzed. The incoming

ions undergo elastic collisions with nuclei of target atoms, and during this process the ions lose energy. The reduction in energy of the backscattered ions depends on masses of incident and target atoms and thus is signature of the target atoms. 2MeV He ions are best suited as the incident beam for RBS experiment.

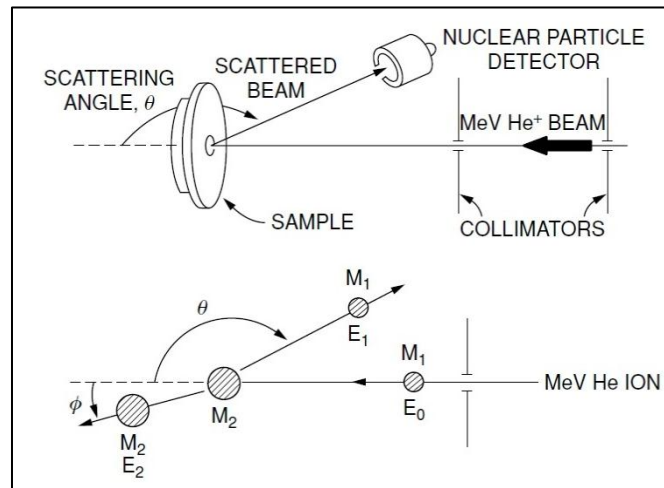


Fig. 4 Schematic of RBS [5]

The energy  $E_1$  of backscattered projectile is given by,

$$E_1 = KE_0 \quad (2.8)$$

where,  $K$  is the kinematic factor and  $E_0$  the energy of incoming ions. Kinematic factor is the ratio of energy of projectile before collision to energy after collision and is given by,

$$K = \frac{M_1^2}{(M_1 + M_2)^2} \left\{ \cos \theta \pm \left[ \left( \frac{M_2}{M_1} \right)^2 - \sin^2 \theta \right]^{1/2} \right\}^2 \quad (2.9)$$

## Chapter 2

where,  $M_1$  and  $M_2$  are the mass of incoming ion and target nuclei respectively and  $\theta$  the scattering angle. If the target contains more than one element with mass difference  $\Delta M_2$ , the energy separation  $\Delta E_1$  of particles is given by,

$$\Delta E_1 = E_0 \frac{dK}{dM_2} \Delta M_2 \quad (2.10)$$

The mass separation and energy resolution is better for lighter elements than heavier ones. The quantitative analysis of elemental composition can be obtained from the scattering cross section. Scattering cross section is defined as the probability that the ion can cause a backscattering collision and is given by,

$$\sigma(E, \theta) = \left( \frac{Z_1 Z_2 e^2}{4E} \right)^2 \times \frac{4 \left[ (M_2^2 - M_1^2 \sin^2 \theta)^{1/2} + M_2 \cos \theta \right]^2}{M_2 \sin^4 \theta (M_2^2 - M_1^2 \sin^2 \theta)^{1/2}} \quad (2.11)$$

The yield is the number of backscattered particles detected which is denoted as  $Y$  and is given by,

$$Y = \sigma(E, \theta) \Omega Q N_s \quad (2.12)$$

where,  $\Omega$  is the detector solid angle,  $Q$  is the total number of incident particles in the beam and  $N_s$  is the areal density. By knowing the atomic density, thickness can be calculated [4].

The RBS spectrum is analyzed with the help of computer simulation programs like XRUMP and SIMNRA.

Advantages of RBS:

It is a nondestructive technique

No need of any reference standards for data analysis

Film thickness, composition and depth profile can be inferred easily

Limitations:

Poor mass resolution for heavier elements

The mass resolution is poorer for thicker films

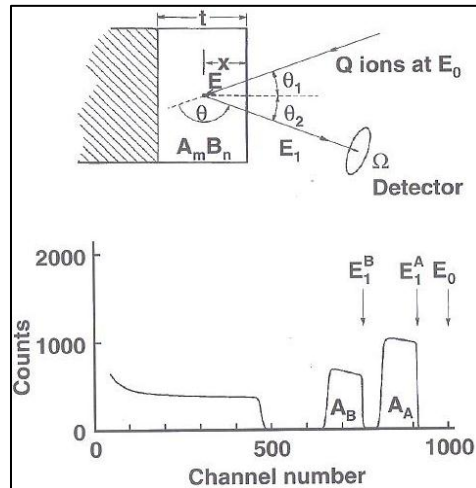


Fig. 5 Typical RBS spectrum [5]

## 2.5 X-RAY REFLECTIVITY (XRR)

X-ray reflectivity technique is a surface sensitive analytical technique used to characterize surfaces, thin films and multilayers. It can provide precise determination of film thickness and surface or interface roughness. When X-rays impinge on a flat surface, it gets reflected from the surface when the incident angle is less than the critical angle. At incident angles greater than the critical angle, the X-rays penetrate, and get reflected from interface. The rays reflected from the surface and interface interferes to produce interference fringes. This was first observed by Kiessig and these fringes are also known as Kiessig fringes [6].

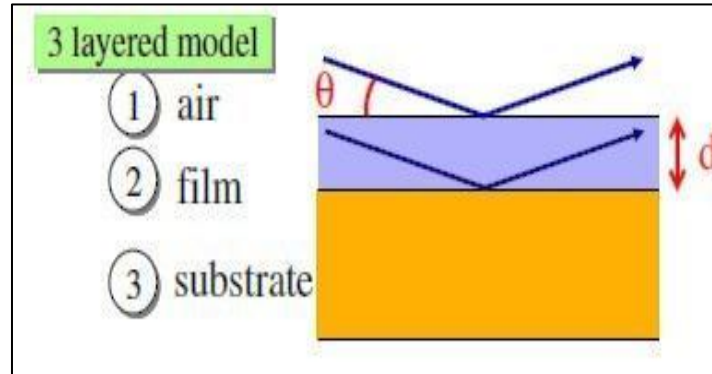


Fig. 6 Reflection of X-rays from a layered structure

The refractive index of X-rays are slightly less than 1, and is given by,

$$\eta = 1 - \delta + i\beta \quad (2.13)$$

where,  $\delta$  and  $\beta$  are the dispersion and absorption of x rays by the material and is given by,

$$\delta = \frac{r_0 \lambda^2}{2\pi} (Z + f') n_{atom} \quad (2.14)$$

$$\beta = \frac{r_0 \lambda^2}{2\pi} f'' n_{atom} \quad (2.15)$$

Where,  $r_0$  is the Bohr atomic radius,  $\lambda$  is the X ray wavelength,  $Z$  is the number of electrons per atom. The complex form factor is defined as

$$f = Z + f' + if'' \quad (2.16)$$

$n_{atom}$  is related to the material density  $\rho$  as

$$n_{atom} = \frac{N_A}{A} \rho \quad (2.17)$$

where,  $N_A$  is the Avogadro number and  $A$  the atomic weight. The film thickness is determined by the period of oscillation of interference fringes and the decay rate of reflectivity curve gives information about roughness.

The X-ray reflectivity is measured using glancing X-ray diffractometer with some modifications. The incident angle is varied and the reflectivity is measured. A monochromator is normally used in the incident beam to remove unwanted X-ray wavelengths and, in combination with slits, to collimate the incident beam. Often, the  $K\alpha_1$  emission line of a Cu anode source (1.5405 Å) is employed. Two concentric goniometers are used, with the sample mounted on one goniometer and the detector on the other. A slit is placed in front of the detector to define the angle of the reflected beam (figure 7). Alternatively, a second monochromator/slit arrangement can be used for this purpose. This can further reduce unwanted background radiation [6].

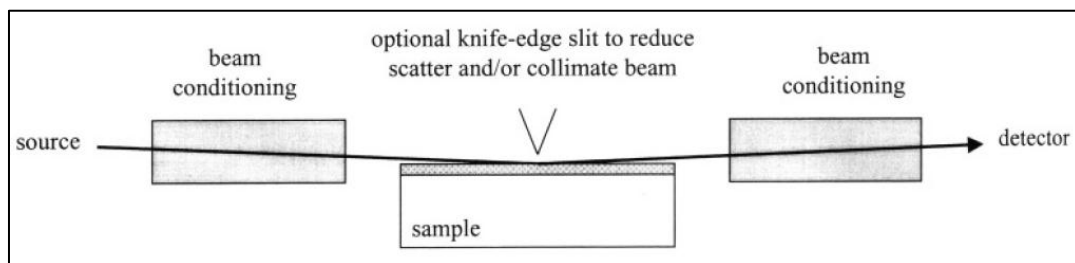


Fig. 7 Alignment of diffractometer for XRR [6]

The reflectivity versus incident grazing angle obtained after the reflectivity measurement is fitted using the Parratt software to determine thickness and roughness.

## **2.6 X-RAY DIFFRACTOMETER (XRD)**

X-ray diffraction is the classical method for determining the crystalline structure of solids. The basic principle of XRD is the Bragg's law which states that the X-rays reflected from the different planes of the crystal constructively

## Chapter 2

interfere when the path difference is an integral multiple of wavelength which is mathematically expressed as,

$$n\lambda = 2d_{hkl} \sin \theta, \quad (2.18)$$

where,  $n$  is an integer,  $\lambda$  is the wavelength of the radiation,  $d_{hkl}$  is the spacing between atomic planes and  $\theta$  is the diffraction angle. The interplanar spacing can be computed by employing the relation

$$d_{hkl} = \frac{1}{\sqrt{\frac{h^2}{a^2} + \frac{k^2}{b^2} + \frac{l^2}{c^2}}} \quad (2.19)$$

where  $a$ ,  $b$ ,  $c$  are the lattice parameters.

For cubic symmetry,  $a=b=c$

$$d_{hkl} = \frac{a}{\sqrt{h^2 + k^2 + l^2}} \quad (2.20)$$

The components of a diffractometer include a monochromatic radiation source, sample stage (goniometer), radiation detection system, enclosure, and safety features. One of the most common configurations is the  $\theta$ - $2\theta$  upright. This configuration of diffractometer has a movable detector and an X-ray source, rotating about the circumference of a circle centered on the surface of a flat powder specimen. The intensity of a diffracted beam is measured directly by an electronic solid-state detection system. The diffracted beam of X-rays generates electron-hole pairs in the detector. The electronic system converts the collected charge into voltage pulses. The number of pulses per unit of time counted by the electronic system is directly proportional to the intensity of the X-ray beam entering the detector [5].

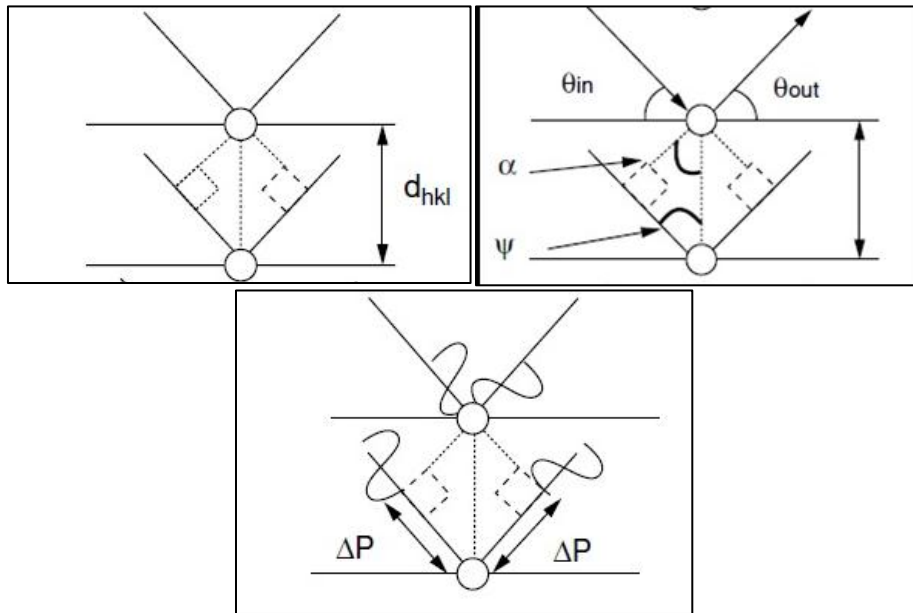


Fig. 8 Derivation of Bragg's law [5]

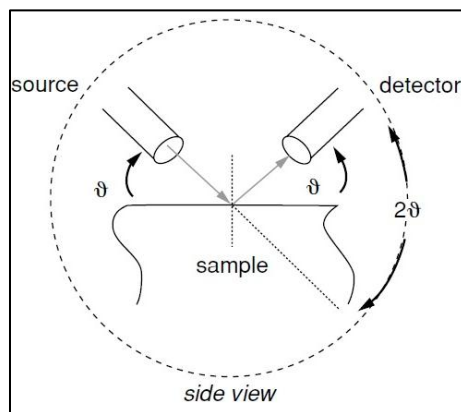


Fig. 9 Schematic view of  $\theta$ - $2\theta$  geometry of XRD [5]

Figure 9 shows the schematic of a  $\theta$ - $2\theta$  upright. The source and detector move at a constant angle  $\theta$  relative to the sample. Thus, the angle between source and detector is  $2\theta$  relative to one another. This is the conventional  $\theta$ - $2\theta$  geometry

also known as Bragg- Brentano reflection geometry. This tool is ideal for powders and large samples [5]. Once the diffraction pattern is obtained, sample can be identified by comparing with the standard International Centre for Diffraction Data (ICDD) file.

The crystallite size can be determined from the XRD pattern using the Scherrer formula given by,

$$D = \frac{0.9\lambda}{\beta \cos \theta} \quad (2.21)$$

where, D is the crystallite size,  $\beta$  is the angular width in radian which is equal to full width at half maximum.

## **2.7 GLANCING ANGLE X RAY DIFFRACTOMETER (GXR)**

In the case of thin films, significant information about its structure cannot be obtained from XRD. This is because the penetration depth of X-rays is higher than the film thickness and sample information obtained from XRD will be superimposed by that of the substrate. Thus it is necessary to limit the depth from which information is gathered. This can be realized by reducing the angle of X-rays with respect to sample surface.

In glancing angle X-ray diffraction (GAXRD) technique, the Bragg-Brentano geometry of XRD is modified to an asymmetric para-focusing Seeman Bohlin geometry (figure 10). This geometry allows the incident X-rays to impinge on the sample at a small angle,  $\gamma_G$  (usually  $1^\circ$  to  $3^\circ$ ). The diffracted X-rays are recorded by a detector that moves along the focusing circle. The X-ray path length is proportional to  $1/\sin\gamma_G$ , therefore smaller incident angles provides good sensitivity for thin films, as the increased path length in films can provide large diffracting volume of the film. By increasing the path length of the incident X-ray beam through the film, the substrate contribution drastically reduces and thus the

intensity of the diffracted planes from the film can be increased. Thus GXR D can provide proper structural information of thin films [6].

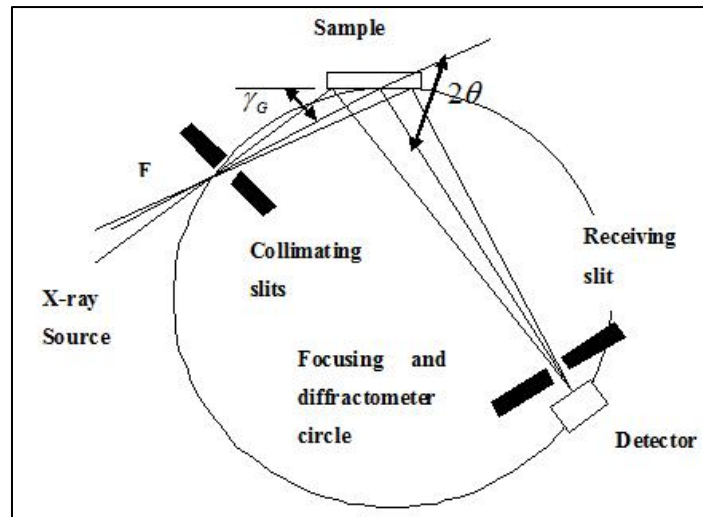


Fig. 10 Seeman Bohlin geometry for GXR D [7]

## 2.8 TRANSMISSION ELECTRON MICROSCOPE (TEM)

TEM is a highly efficient and versatile technique to view nano sized objects. TEM allows visualization of grains, grain boundaries and lattice planes. TEM is similar to an optical microscope but uses accelerated electrons instead of a light source. The wavelength of electrons is comparable with atomic planes and thus can be used to view the grains and the planes.

From De Broglie equation one can obtain the electron wave length as,

$$\lambda = \sqrt{\frac{1.5}{V}} \quad (2.22)$$

where, V is the accelerating voltage.

The four basic components of TEM are:

## *Chapter 2*

1. Electron gun that emits a beam of monochromatic electrons which act as the illumination source
2. Set of condenser lenses to focus the illumination onto the specimen
3. Objective lens to form the first image of the specimen
4. Series of magnifying lenses to create the final magnified image

The electron gun produces a beam of monochromatic electrons either by tungsten filament or using lanthanum hexa boride source. The first and second condenser lenses focus the electron beam to a thin coherent beam. The first lens controls the beam-spot size and dictates the general size range of the final spot that illuminates the sample. The second lens controls the intensity and the size of the spot on the sample. The condenser aperture removes high-angle electrons i.e. electrons far from the optic axis, thus provides a collimated beam. The beam strikes the specimen, and a portion of the beam is transmitted through the sample and other parts of the beam are diffracted. The transmitted portion of the beam is focused by the objective lens into an image. The electron image is focused by adjusting the objective focal length. The image passes through the intermediate and projector lenses and is magnified onto the viewing screen. The viewing screen is a fluorescent screen typically coated with a fine-grain ZnS. When the electrons strike the screen, fluorescence occurs and results in the formation of a visible image. Through the thicker or denser areas of the sample, only fewer electrons are transmitted and appear darker in the image. In contrast, the thinner or less dense areas allows transmission of more electrons and appear lighter in image [5].

TEM can operate in two modes; image mode and diffraction mode. The image mode produces the image of the sample that is illuminated with electrons. The diffraction mode known as selected area electron diffraction is discussed in the next section.

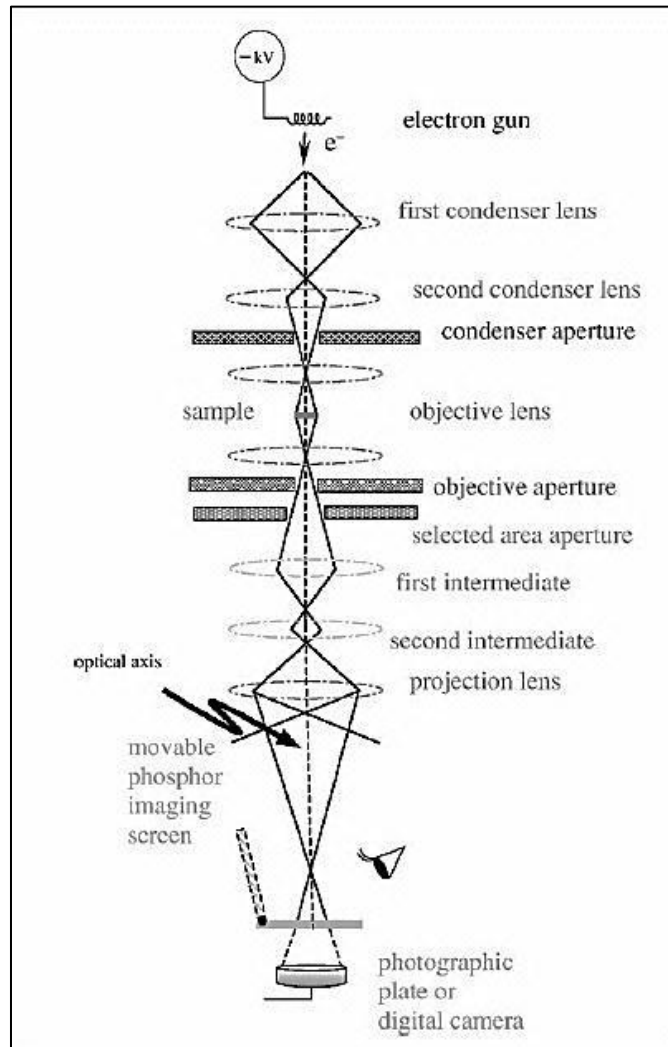


Fig. 11 Lay out of TEM [5]

## 2.9 SELECTED AREA ELECTRON DIFFRACTION (SAED)

SAED can give information about the crystallography of the sample. In SAED, an intermediate aperture is placed at the first intermediate image focal plane to specify the area from which the diffraction image is acquired. As the

electron wavelength is comparable to the inter planar distance, the lattice planes acts as diffraction grating to the electrons and diffraction patterns are obtained [5].

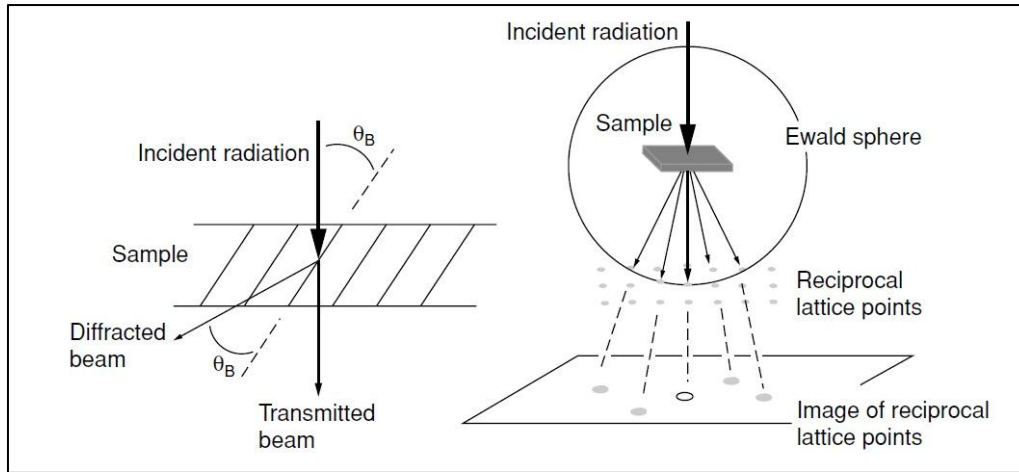


Fig. 12 View of the incident and diffracted radiation in SAED [5]

For single crystals, the diffraction pattern is obtained as a series of spots. In the case of polycrystalline material, the planes where the diffraction condition is satisfied gives a ring pattern. Each ring corresponds to one specific plane. The inter planar spacing can be calculated from the radius of rings in diffraction pattern as,

$$\lambda L = d_{hkl} R \quad (2.23)$$

where,  $\lambda L$  is camera constant and varies with the lens settings in the microscope.  $R$  is the radius of the diffraction ring. For amorphous samples, the diffraction pattern is obtained as diffused rings.

## 2.10 X-RAY PHOTOELECTRON SPECTROSCOPY (XPS)

X-Ray Photoelectron Spectroscopy (XPS) also referred as Electron Spectroscopy for Chemical Analysis (ESCA) is a common technique used for

elemental quantification of a material. It can also provide information like the oxidation state, chemical formula and electronic state of elements. XPS can provide information of the sample surface up to a depth of few nanometers. The basic principle involved is the photoelectric effect. An incident X-ray gives its energy to knock out the electron, that is to ionize and the remaining energy appears as the kinetic energy of the ejected electrons. The kinetic energy distributions of photoelectrons are characteristic of the electron shell from which it is ejected. The kinetic energy  $E_K$  of ejected electrons is given by,

$$E_K = h\nu - E_B - \varphi \quad (2.24)$$

where,  $E_B$  is the electron binding energy and  $\varphi$  is the work function. Sometimes instead of ejecting the X-ray photoelectron, auger electrons are ejected. When a vacancy is produced in one of the inner shell of the atom, it may be filled by a non radiative (Auger effect) process. The electrons emitted by Auger processes are called Auger electrons [5].

An XPS spectrum gives the photoelectron intensity as a function of electron binding energy. The basic requirements of XPS are a source of monochromatic radiation usually an X-ray source, an electron energy analyzer that can disperse the emitted electrons according to the kinetic energy, electron detector and a high vacuum environment.

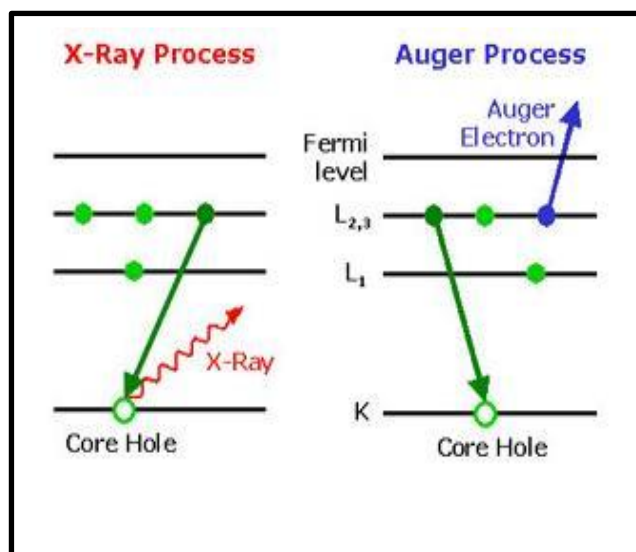


Fig. 13 X-ray photoelectron effect and Auger effect

X-rays are produced using Al or Mg targets and the energies of the Al  $K_{\alpha}$  and Mg  $K_{\alpha}$  radiations are 1486.6eV and 1253.6eV respectively. The electron energy analyzer used in XPS is a hemispherical analyzer, and the selected kinetic energies are fed to the detector. An ultra high vacuum of the order of  $10^{-9}$  Torr is usually preferred in XPS.

The XPS wide scan contains the C 1s peak since the presence of impurity carbon is usually unavoidable. The C 1s peak appears at 284.5 eV; the change in position of C 1s peak indicate shift in peak positions and then the spectrum needs to be calibrated in accordance with the C 1s peak. Once the calibration is done, peaks are identified and assigned to respective elements either manually or with the help of software. Individual elemental peaks obtained from the slow scan can be deconvoluted and chemical states of elements can be identified [5].

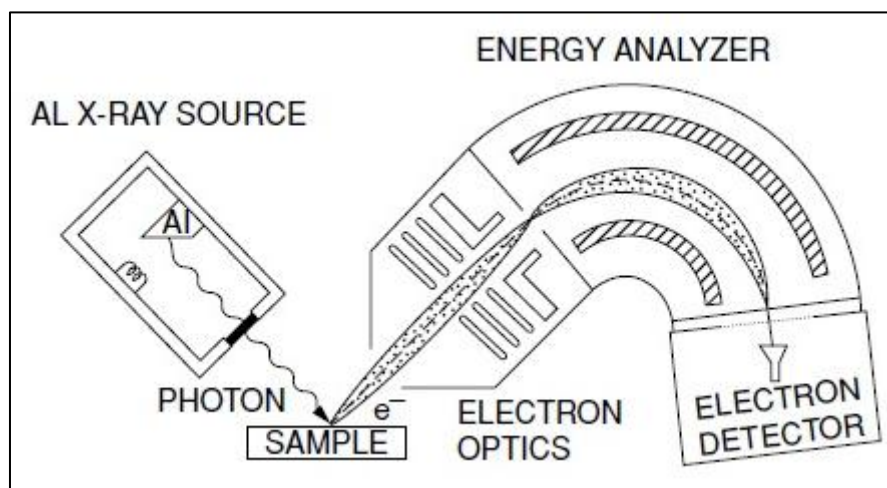


Fig. 14 Layout of XPS [5]

## 2.11 ATOMIC FORCE MICROSCOPE (AFM)

Atomic force microscopy comes under the broad category of scanning probe microscopes which began to gain momentum by early 1990s. The fundamental use of scanning probe microscopes is to image and measure surfaces on a fine scale. The major three elements of these microscopes are: a probe that interact with the surface, a detection system that monitors the probe–surface interaction and the raster scanning of probe or sample with nano scale precision.

In AFM, the probe tip is fixed to a cantilevered beam. Usually silicon nitrides are used as AFM probe. The probe interacts with the surface and the resulting force deflects the beam in a repulsive manner, given by Hooke's law. The attractive and repulsive forces between atoms of the probe and the surface can be monitored when brought extremely close to each other. At short distances (0.1 nm to 10 nm) the probe tip experiences inter-atomic forces characterized by weak Van der Waals forces. On moving away from the surface, Van der Waals forces decay rapidly and become negligible. At 100-500 nm above the surface,

## Chapter 2

long-range electric, magnetic and capillary forces are significant and can be probed. The net forces acting on the probe tip deflect the cantilever, and the tip displacement is proportional to the force between the surface and the tip. As the probe tip is scanned across the surface, a laser beam reflects off the cantilever. The deflection of cantilever is detected using a position sensitive photodiode. By monitoring the net (x, y, and z) deflection of the cantilever, a three-dimensional image of the surface is constructed [5].

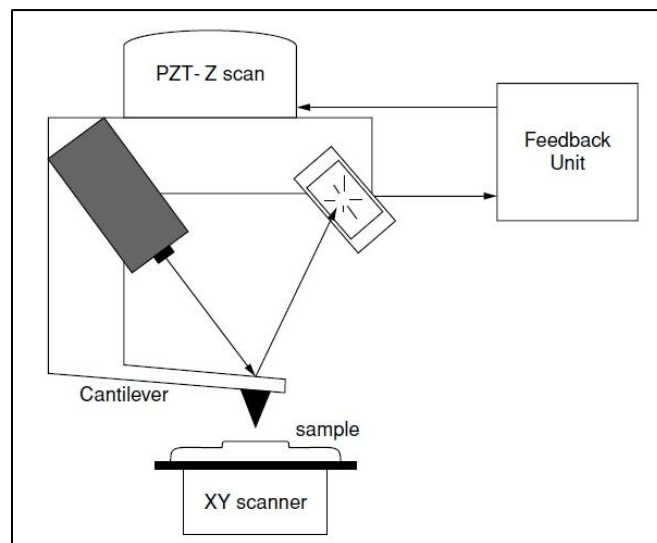


Fig. 15 Schematic of AFM [5]

AFM can be operated mainly in three different modes: Contact mode, non contact mode and tapping mode. Contact mode is the most common method of operation of the AFM. In this mode, the tip and sample are in contact and the deflection of the tip is due to repulsive forces. In the noncontact mode, the probe tip resonates at a distance above the sample surface and the forces generated are no longer in the repulsive region. In tapping mode, the tip is brought

intermittently into contact with the surface during scanning. The basic idea is that the cantilever is brought into oscillation and changes in oscillation amplitude or phase are detected as the vibrating tip sweeps across and interacts with the surface. The tapping mode can overcome the limitations of contact and non contact mode [5, 7, 8].

The AFM images can provide insight about surface roughness, grain size distribution and uniformity of surface features.

## **2.12 VIBRATING SAMPLE MAGNETOMETER (VSM)**

Vibrating Sample Magnetometer is the most commonly adopted technique to study the magnetic property of materials. The idea of VSM was first proposed by S Foner in 1959. The basic principle of VSM is the electromagnetic induction. Accordingly, when a magnetic sample is vibrated, the change in flux can induce an emf and the induced emf will be proportional to the magnetic moment of the sample.

The sample is attached to the end of a nonmagnetic rod and placed in between the pole pieces of a magnet and the other end of rod is fixed to a loudspeaker cone or other mechanical vibrator. The oscillating magnetic field of the moving sample induces an alternating emf which is detected by the pick up coils and its magnitude is proportional to the magnetic moment of the sample. A lock-in amplifier amplifies the signal from the pick up coils (figure 16) [9].

The amount of magnetic flux  $\phi$  linked to the coil due to the dipole moment of sample placed in the magnetic field  $M$  is given by

$$\phi = \mu_0 N \alpha M \quad (2.25)$$

where,  $\mu_0$  is the permeability of free space,  $N$  is the number of turns per unit length of coil and  $\alpha$  represents the geometric moment decided by position of

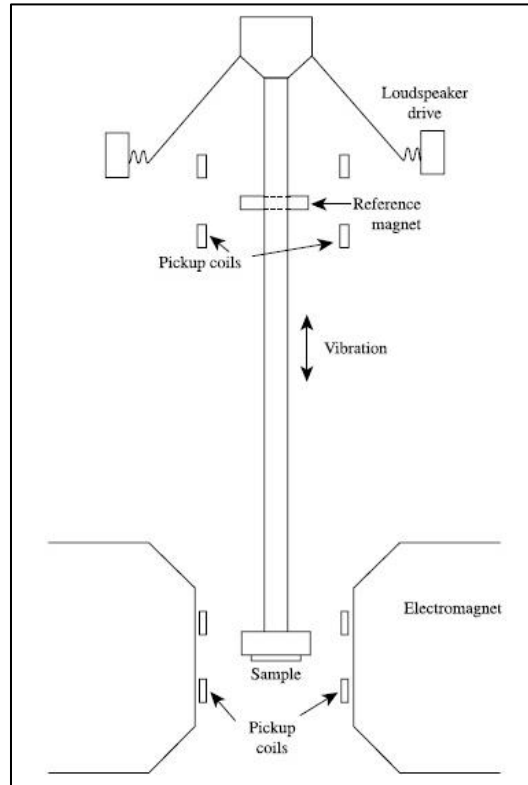


Fig. 16 Schematic of VSM [9]

moment with respect to coil as well as shape of coil. An anharmonic oscillator of the type  $z = z_0 + Ae^{j\omega t}$  induces an emf in the stationary detection coil.

The induced emf is given by

$$V = -\frac{d\phi}{dt} = -j\omega\mu_0 nMA \left( \frac{\partial \alpha}{\partial z} \right) e^{j\omega t} \quad (2.26)$$

where, A is the amplitude of vibration and  $\omega$  is the frequency of vibration.

Amplitude of vibration, frequency and  $\left( \frac{\partial \alpha}{\partial z} \right)$  are constants. Therefore, the

induced voltage is proportional to the magnetic moment of the sample.

Low temperature magnetic studies can be performed by attaching suitable cryogenic set ups. Usually the sensitivity of VSM to low temperature measurements is poor. More advanced techniques to study both room temperature and low temperature magnetic moments with great accuracy and sensitivity have been developed.

### **2.13 SUPER CONDUCTING QUANTUM INTERFERENCE DEVICE (SQUID) MAGNETOMETER**

SQUID employs the principle of superconductivity which is based on the tunneling of superconducting electrons across a Josephson junction. Josephson junction is formed by two superconductors separated by a thin insulating layer. Two Josephson junctions are used in SQUID. A superconducting measuring current flows through the ring and gets equally divided so that equal currents pass through each of two Josephson junctions. According to Faraday's law, a changing magnetic flux through the ring generates a voltage and a current in the ring. This induced current adds to the measuring current in one junction, and subtracts in the other. Because of the wave nature of the superconducting current, the resistance and the voltage between points A and B in the superconducting circuit appears periodically. Each voltage step corresponds to the passage of a single flux quantum across the boundary of the ring. The device is linked to a coil to measure the flux from the sample, and thus the magnetization. A superconducting Josephson device requires low temperature operation, and it is used in conjunction with a superconducting solenoid [9]. The sensitivity of SQUID magnetometers is of the order of  $10^{-14}$  T.

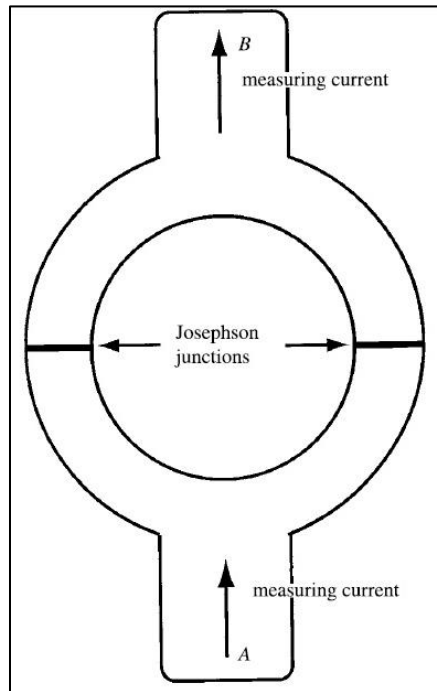


Fig. 17 SQUID flux sensor [9]

### 2.13.1 Modes of Magnetic Measurements:

According to the requirements of our study, magnetic measurements can be carried out in different ways.

**MH measurements:** The most common magnetic measurement is the hysteresis loop measurement usually denoted as MH measurements at room temperature. Apart from room temperature MH, we have also carried out MH studies at 10K. For this the system is cooled to 10K and then the hysteresis is measured.

**FC-ZFC measurements:** FC-ZFC is the acronym of Field Cooled-Zero field cooled measurements. These measurements are carried out to study the low temperature magnetic behavior. The system is initially cooled from room temperature to low temperature (usually liquid Helium temperature), then a

constant magnetic field is applied and the moment is measured by warming the sample to room temperature. This is the ZFC measurement. The system is now cooled to low temperature in the presence of an applied field and the moment is measured during warming the sample. This is the FC measurements. The FC state of a system is considered to be the equilibrium state and ZFC state is the metastable state. The difference between FC and ZFC moments indicate irreversibility in the system which is due to the anisotropy present. In nanoparticles the competing magnetic interactions can give rise to irreversibility. This kind of irreversibility can disappear above a particular temperature and at a particular cooling field. When the irreversibility disappears, the system has only one magnetic state. The ZFC curve usually shows a maximum at some particular temperature denoted as the blocking temperature  $T_B$ . At this temperature, more moments align with applied field minimizing the Zeeman energy. Above  $T_B$ , the thermal vibrations become stronger and randomize the magnetic moments reducing the magnetisation. Depending upon the variation of irreversibility temperature and blocking temperature with the cooling field, significant information about magnetic ordering can be obtained.

***MH measurements with FC:*** In order to study the exchange bias in ferromagnetic-antiferromagnetic (FM-AFM) systems, it is necessary to field cool the system. Initially MH measurements are taken at room temperature. Now the system is cooled in the presence of a field below the Neel temperature of the AFM, and then the hysteresis measurement is performed. In the case of exchange bias system, one can observe a hysteresis loop shift in the field cooled measurements.

**REFERENCES:**

- [1] Francesco Branda, The Sol-Gel Route to Nanocomposites, Advances in Nanocomposites - Synthesis, Characterization and Industrial Applications, Dr. Boreddy Reddy (Ed.), InTech **2011)**
- [2] Edgar Alfonso, Jairo Olaya and Gloria Cubillos, Thin Film Growth Through Sputtering Technique and Its Applications, Crystallisation Science and technology, InTech
- [3] [www.iuac.res.in](http://www.iuac.res.in)
- [4] M. Mayer, Lectures at the Workshop on Nuclear Data for Science and Technology: Materials Analysis Trieste, 2003
- [5] Terry L. Alford, Leonard C. Feldman, James W. Mayer, Fundamentals of Nanoscale Film Analysis, Springer 2007]
- [6] P. Neil Gibson Edited by Gernot Friedbacher and Henning Bubert, Surface and Thin Film Analysis, Wiley-VCH Verlag & Co. KGaA 2011
- [7] Hysen Thomas (2013) On the Tailoring of Magnetic Properties of Fe-Based Alloy Thin Films by Swift Heavy Ion Irradiation and Thermal Annealing, PhD Thesis, Cochin University of Science and Technology, India
- [8] Geetha P (2014) Tailoring magnetic properties of Co-Fe thin films by topographical modifications using thermal annealing and swift heavy ion irradiation and fabrication of magnetoelectric multilayers for device applications, PhD Thesis, Cochin University of Science and Technology, India
- [9] B.D. Cullity, C.D. Graham, Introduction to Magnetic Materials, 2nd ed., John Wiley and Sons Inc., 2008

## Chapter 3

### **Fabrication of RF sputtered FeNiMoB thin films and modification of its structural, topographical and magnetic properties by thermal annealing**

#### 3.1 Introduction

#### 3.2 Experimental Methods

#### 3.3 Results and Discussions

- Thickness measurement: X Ray Reflectivity (XRR)
- Structural Characterization: Glancing angle X-ray Diffractometer (GXRD), Transmission Electron Microscope (TEM) & Selected Area Electron Diffraction (SAED)
- Compositional analysis: X-ray Photoelectron Spectroscopy (XPS)
- Topographical Studies: Atomic Force Microscope (AFM)
- Magnetic studies: Super conducting Quantum Interferometer Device -Vibrating Sample Magnetometer (SQUID-VSM)

#### 3.4 Conclusion

#### References

*Lisha R. et al. Materials Research Express 1 (2014) 015707*

*Chapter 3*

### **3.1 INTRODUCTION**

The research and development of amorphous and nanocrystalline soft magnetic alloys have gained impetus during the past few decades. These soft magnetic alloys have supplemented and replaced conventional soft magnetic ferrites and permalloy cores in industrial electronics [1]. This new class of materials was invented in 1959 by Paul Duwez, and exhibited superlative soft magnetic properties. The magnetic properties of these materials are attributed to their biphasic microstructure consisting of soft magnetic nanocrystals embedded in a paramagnetic amorphous matrix [2]. The magnetic properties of these materials are determined by their alloy composition, grain size and exchange correlation length. The variation of magnetic properties with grain size can be explained using Herzer's Random Anisotropy Model (RAM), according to which, when the grain size  $D$  is less than the exchange length, the anisotropies are averaged [3]. As a result, the coercivity scales as the sixth power of grain size. For Fe based nanocrystalline alloys, the grain size as well as intergrain separation are about 5-25 nm, and exchange length is about 35-40 nm.

$\text{Fe}_{40}\text{Ni}_{38}\text{Mo}_4\text{B}_{18}$ , belongs to the family of metallic glass amorphous alloys. They exhibit excellent soft magnetic properties, with a saturation magnetization of 87emu/g and are commercially available in the form of ribbons, with a typical thickness of 20 $\mu\text{m}$  and a few centimeters in length [4]. The amorphous structure can be devitrified into a nanocrystalline state by thermal annealing or ion irradiation [5-7]. Nanocrystalline morphology has been observed to be more favorable for superior soft magnetic properties compared to their amorphous counterparts [8]. The combination of various physical properties resulting from nanocrystallization makes them ideal for various sensor applications.

### Chapter 3

There exists ample work on the kinetics of crystallization of  $\text{Fe}_{40}\text{Ni}_{38}\text{Mo}_4\text{B}_{16}$ . [6- 7, 9-11] .The enthalpy of formation and activation energy can be evaluated by employing various methods like Kissinger [12] Moynihan [13] and Marseglia [14] techniques.  $\text{Fe}_{40}\text{Ni}_{38}\text{Mo}_4\text{B}_{16}$  follows two stage crystallization processes [6, 7, 10]. The first stage is the Fe-Ni phase, which crystallizes by primary crystallization and the second phase is  $(\text{FeNiMo})_{23}\text{B}_6$ , which crystallizes via polymorphic crystallization. The enthalpy of formation and activation energy are 19.39J/g and 3.49eV/atom for Fe-Ni phase and 54.09J/g and 4.5eV/atom, for  $(\text{FeNiMo})_{23}\text{B}_6$  phase [6, 7, 10]. The as prepared ribbons are amorphous and crystallisation takes place with suitable heat treatments. The Fe-Ni phase usually precipitates above 673K and  $(\text{FeNiMo})_{23}\text{B}_6$  above 773K [6, 7].

Thin film forms of metallic glasses find variety of applications as magnetic sensors since they can be integrated in to Micro Electro Mechanical Systems (MEMS) and Nano Electro Mechanical Systems (NEMS) devices, as pinning layers in magnetic tunnel junctions and magnetic read heads [15-16]. The studies on thin films of metallic glasses are significant both from an applied angle and fundamental perspective. Attempts to fabricate thin film forms of  $\text{Fe}_{40}\text{Ni}_{38}\text{Mo}_4\text{B}_{18}$  were reported earlier by many researchers [17-18]. Jyothi *et al.* deposited thin films by flash evaporation technique and the deposited films were found to be crystalline in nature [17]. Senoy *et al.* and Hysen *et al.* reported the fabrication of thin films from composite targets using vacuum evaporation [19-20]. They also studied the effect of annealing and swift heavy ion irradiation on these films and reported the formation of Fe-Ni nanocrystals on annealing [21-22]. However, they could not retain the stoichiometry of the original target in

films, owing to the variations in the vapour pressure of the different alloying elements in the target during the physical vapour deposition process. Annealing the films resulted in the precipitation of only the magnetic Fe-Ni phase, while annealing the ribbon resulted in the precipitation of both ferromagnetic Fe-Ni phase and paramagnetic  $(\text{FeNiMo})_{23}\text{B}_6$  [9-10, 19].

In metallic glasses, each target element has its own role in controlling the microstructure and thereby the magnetic properties. Retaining the stoichiometry of target in the thin film is of great interest as the stoichiometry of films can affect the structure, kinetics of phase transformation and magnetic properties. The mismatch in composition of target and film could be avoided by using techniques like RF sputtering or pulsed laser deposition. In this chapter, we discuss the fabrication of Fe-Ni-Mo-B thin films by RF sputtering and the evolution of their microstructure and magnetic properties with thermal annealing.

### **3.2 EXPERIMENTAL METHODS**

The bulk  $\text{Fe}_{40}\text{Ni}_{38}\text{Mo}_4\text{B}_{18}$  ribbons having a thickness of 20  $\mu\text{m}$  were severed into a circle of diameter 2 inch which is subsequently used as the cathode for RF sputtering. The substrates used were naturally oxidised silicon. The deposition was carried out with RF power of 100 watts for 30 minutes in an argon atmosphere. Base pressure of  $9 \times 10^{-5}$  Torr was attained, using a turbo pump backed by a scroll pump, which elevated to  $5 \times 10^{-2}$  Torr during deposition. The as deposited films were vacuum annealed for 1 hour at temperatures of 673K and 873K. The film thickness was estimated from X Ray Reflectivity (XRR) measurements carried out using Bruker Discover D-8 with  $\text{CuK}\alpha$  ( $\lambda=1.5406\text{\AA}$ ) radiation. The experimental data was fitted employing the Parratt

software [23]. The structural characterization of pristine and annealed films were carried out using Glancing Angle X Ray Diffractometer (GXRD) Bruker Discover D-8 with  $\text{CuK}\alpha$  ( $\lambda=1.5406\text{\AA}$ ) radiation. The measurement was carried out at a grazing incidence of  $0.5^\circ$  and in the range  $30^\circ$  to  $55^\circ$  at a scan speed of  $0.5^\circ$  per minute. The crystallite size was calculated using the Scherrer formula

$$D = \frac{0.9\lambda}{\beta \cos \theta} \quad (3.1)$$

where, D is the crystallite size,  $\lambda$  wavelength of X rays,  $\beta$  full width at half maximum in radians and  $2\theta$ , the diffraction angle. The micro structure were examined using a Transmission Electron Microscope (TEM) (FEI F20) operated at 200 kV. The composition of the films was estimated using X ray Photoelectron Spectroscopy (XPS).  $\text{Al K}\alpha$  radiation having an energy of 1486.6 eV was used as the source for XPS. The obtained XPS spectrum was quantified using Casa XPS program (Casa software ltd. USA). Surface studies were carried out with Atomic Force Microscope (AFM) Digital Instruments Nanoscope. The analysis of AFM images was done using the software Nanoscope 7.2 (Veeco Scientific Ltd.). 7 Tesla MPMS Super conducting Quantum Interferometer Device (SQUID)-Vibrating Sample Magnetometer (VSM) was employed to measure the magnetic properties. Room temperature magnetisation measurements were carried out for magnetic fields ranging from -5 kOe to +5 kOe. Field cooled and zero field cooled (FC-ZFC) measurements were performed in the range of 10 K to 300 K in an applied field of 200 Oe.

### 3.3 RESULTS AND DISCUSSIONS

The thickness of the films is obtained by fitting the XRR data using PARRATT1.6 software. The incident glancing angle is converted to the

corresponding wave vector and plotted with reflectivity. The thickness is found to be ~52 nm (figure 1).

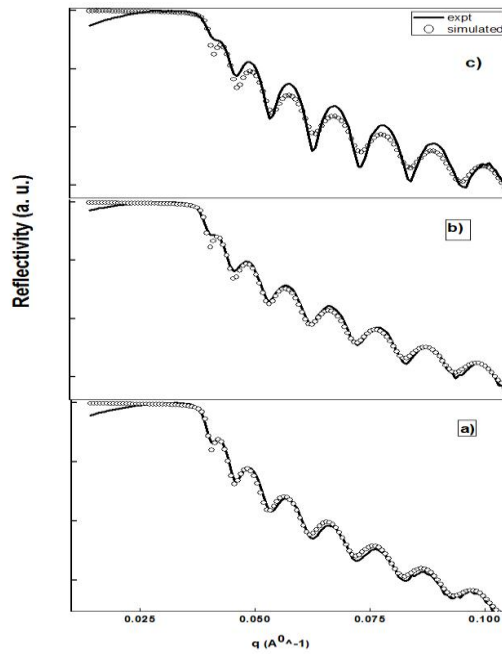


Fig.1 XRR of FeNiMoB film a) pristine b) film annealed at 673K and c) 873K

The GXR D results of the films are shown in figure 2. Contrary to the bulk ribbons, [7, 9] the deposited film is found to be crystalline. Annealing the films does not change the peak position in GXR D. The crystallite size calculated from the Scherrer formula is found to be 35.3nm, 33.2 nm and 35.9nm for pristine and samples annealed at 673K and 873K respectively. It is observed that, there is no significant change in the crystallite size with annealing. Ramanujan *et al.* reported the effect of molybdenum on the crystallization of FeNiMoB ribbons [10]. They observed that Mo inhibits the crystal growth by getting accumulated

at the interface of Fe-Ni crystallites [10]. The pristine film itself is crystalline, and we have observed that on annealing, no new phases are precipitated and the Mo might have inhibited further grain growth. Since Fe-Ni and  $(\text{FeNiMo})_{23}\text{B}_6$  phases have overlapping planes, it is difficult to identify the phase from GXR. To ascertain the crystalline phase, Selected Area Electron Diffraction (SAED) was carried out on the samples.

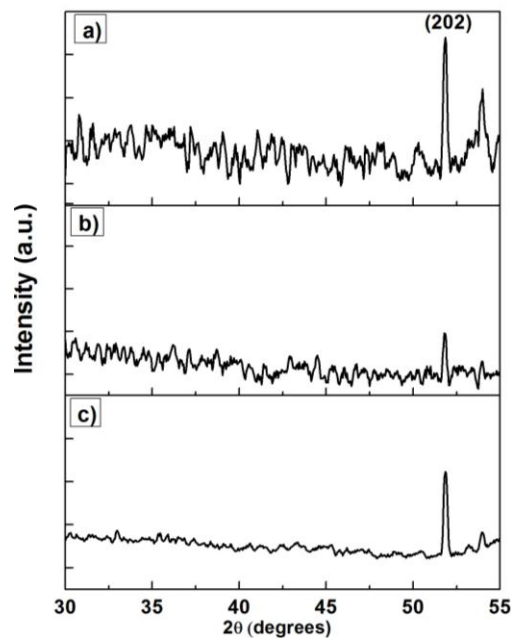


Fig.2 GXR of FeNiMoB film a) pristine b) film annealed at 673K and c) 873K

The SAED images (figure 3a-3b) shows well defined rings signifying the poly crystalline nature of the film. The rings are indexed and compared with the standard data. The inter planar spacing for the pristine film is  $2.46\text{\AA}$ ,  $2.01\text{\AA}$  and  $1.45\text{\AA}$  which corresponds to the (420) plane of  $(\text{FeNiMo})_{23}\text{B}_6$  [ICDD No: 380888], (111) plane of Fe-Ni [ICDD No: 471417] and (440) plane of  $\text{Fe}_{2.92}\text{O}_4$

[ICDD No: 861362] respectively. For the film annealed at 873K, the d values are 1.98Å, 1.68Å and 1.20Å which corresponds to (200) plane of Fe-Ni, [ICDD No: 471417] (620) plane of (FeNiMo)<sub>23</sub>B<sub>6</sub> [ICDD No: 380888] and (444) plane of Fe<sub>2.92</sub>O<sub>4</sub> [ICDD No: 861362] respectively. From GXR and SAED, the crystalline nature of films is confirmed. By employing RF sputtering, both Fe-Ni phase and (FeNiMo)<sub>23</sub>B<sub>6</sub> phase are formed in thin film. The activation energy required for the precipitation of (FeNiMo)<sub>23</sub>B<sub>6</sub> phase is larger than that required for the Fe-Ni phase [6, 7]. However, the RF power of 100W was sufficient for the formation of (FeNiMo)<sub>23</sub>B<sub>6</sub> phase. Liang *et al.* have reported magnetostrictive metallic glass sensors by RF sputtering [24]. They have supplied an RF power of 30W and reported Fe-Ni phase in thin films deposited at 10 mTorr [24, 18]. The RF power of 100W results in the precipitation of both Fe-Ni and (FeNiMo)<sub>23</sub>B<sub>6</sub> phase. TEM of the pristine and film annealed at 873K is shown in figure 3c-3d. The grain size of the films is found to be 10.8±1.9 nm and 11.6±1.5 nm for pristine and film annealed at 873K respectively. The difference in grain size obtained from GXR and TEM is due to the limitation of the Scherrer formula.

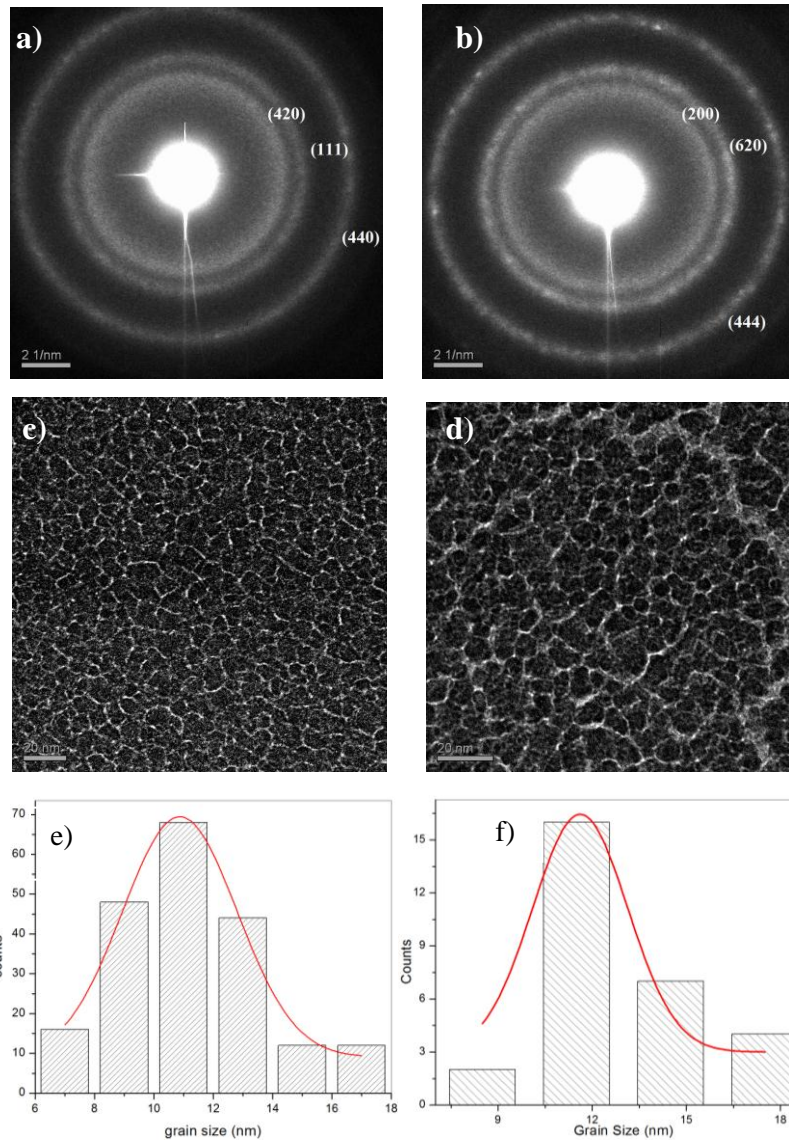


Fig.3 SAED of a) Pristine and b) film annealed at 873K. TEM of FeNiMoB film c) Pristine and d) film annealed at 873K. Crystallite size distribution of e) Pristine and f) film annealed at 873K.

XPS of pristine and films annealed at 873K is shown in figure 4. Since film surface contains unavoidable oxygen and carbon, XPS scan was carried out

after sputtering the film surface for 30 minutes using 500 eV argon ions. From the XPS spectra it is possible to confirm the presence of Fe, Ni, Mo and B. XPS investigation was also carried out on the 873K annealed sample to investigate changes in surface composition with annealing. The composition of the pristine sample is 29.3% Fe, 12.7% Ni, 1.8% Mo, 0.9% B and 55% O. For the sample annealed at 873K, the composition is 9.6% Fe, 11.1% Ni, 3.1% Mo, 0.2% B and 75% O. Along with Fe and Ni, B and Mo are also present in thin film prepared by RF sputtering and these elements play an important role in controlling the grain size and magnetic properties. Even after sputtering the film for 30 minutes, there is presence of carbon and oxygen in the film. The presence of carbon and oxygen emanates from hydrocarbon contamination from XPS unit. In annealed sample, the oxygen content has increased, while the iron content has reduced. Ciang *et al.* reported that the presence of oxygen and carbon in the bulk is due to surface absorption while the presence of these in thin films was due to both absorption and deposition [24]. The target elements were present in thin film; however, the composition could not be retained due to oxygen contamination.

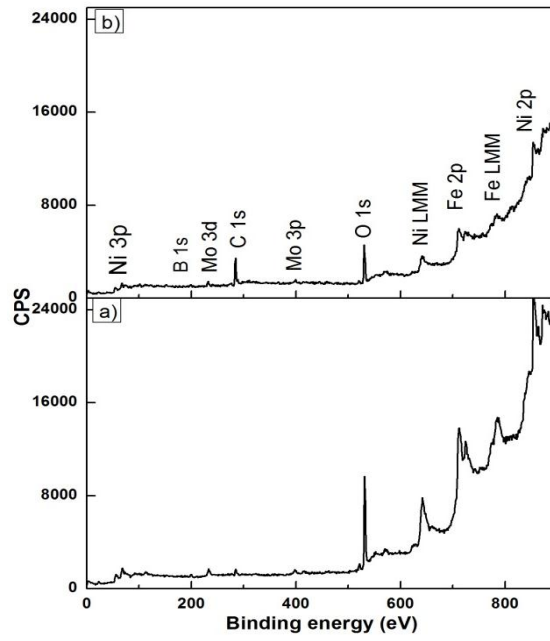


Fig.4 XPS of FeNiMoB film a) pristine film and b) annealed at 873K

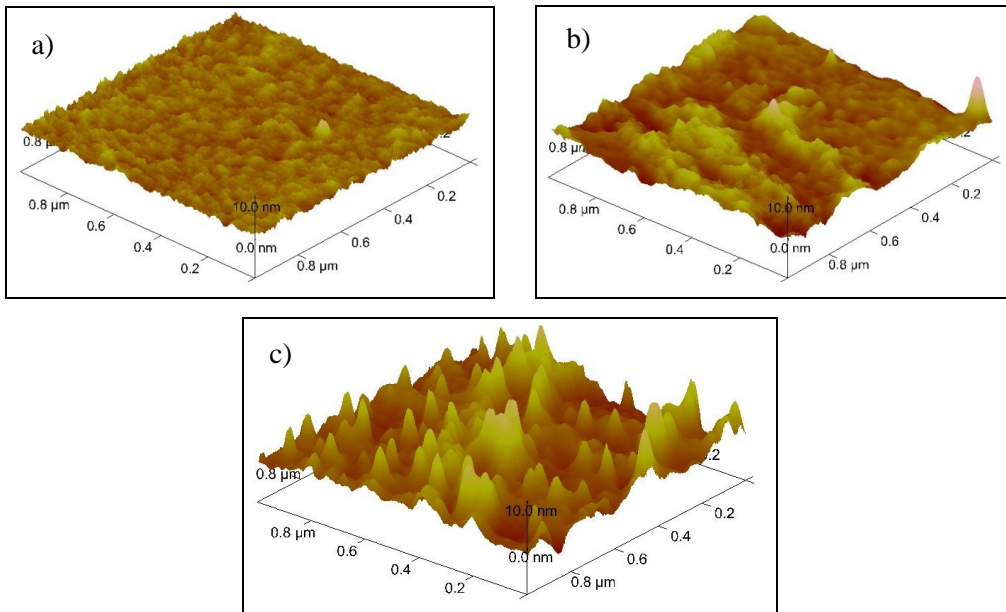


Fig.5 AFM images of FeNiMoB films a) Pristine b) annealed at 673K and c) 873K

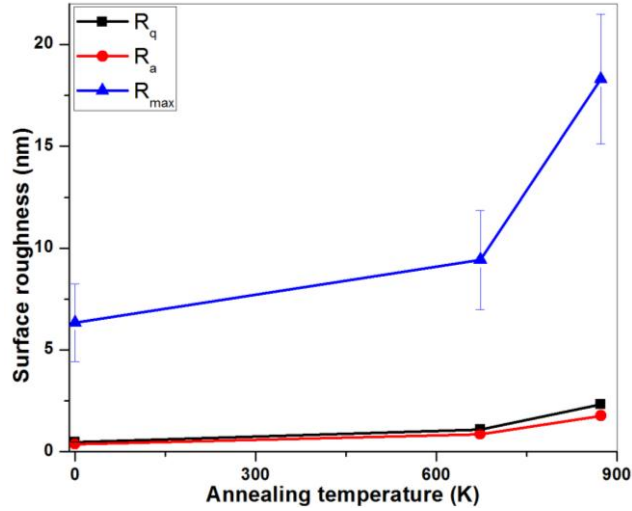


Fig.6 Variation of Surface Roughness with annealing temperature

AFM images of pristine and annealed films are shown in figure 5. The scan area was  $1\mu\text{m} \times 1\mu\text{m}$ . It is clear that significant surface evolution takes place with annealing. The variation of surface roughness with annealing is plotted in figure 6. The surface roughness is found to increase with annealing temperature. RMS roughness ( $R_q$ ) is a statistical parameter which gives the root mean square height of the film surface. However, it does not give any idea about the lateral distribution of surface features. This information can be obtained by power spectral density (PSD) analysis which decomposes the surface profile into spatial spectral frequencies [25]. The PSD function is obtained by Fourier transform of the surface and is given by, [26]

$$PSD(f) = \frac{1}{L^2} \left| \iint \frac{d^2r}{2\pi} e^{-if \cdot r} \langle h(r) \rangle \right|^2 \quad (3.2)$$

### Chapter 3

PSD spectra of the pristine and annealed films are shown in figure 7. The low frequency region represents uncorrelated noise and the high frequency region obeys a power law [27],

$$PSD(f) = Af^{-\xi} \quad (3.3)$$

where,  $\xi$  is the slope.  $\xi$  for pristine film, films annealed at 673K and 873K are 1.6, 1.8 and 2.1, respectively. The slope is related to growth exponent  $\alpha$  according to the relation, [28]

$$\alpha = \frac{\xi - d}{2} \quad (3.4)$$

where,  $d$  is the scan dimension. The growth exponent was calculated and found to be 0.3, 0.4 and 0.55 for the pristine and film annealed at 673K and 873K respectively. Xu *et al.* reported that decrease in growth exponent indicates surface smoothing as a result of surface diffusion, while increase of growth exponent indicates surface roughening due to shadowing or oriented grain growth [28]. For films annealed at 873K, the increased roughness could be due to oriented grain growth as a result of annealing.

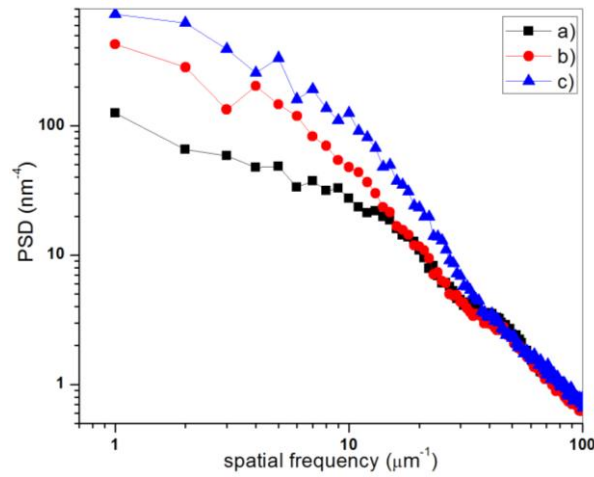


Fig.7 PSD spectra of a) pristine and film annealed at b) 673K and c) 873K

The hysteresis loops of the pristine as well as annealed samples were recorded at room temperature (figure 8) and the variation of coercivity with annealing is shown in figure 9.

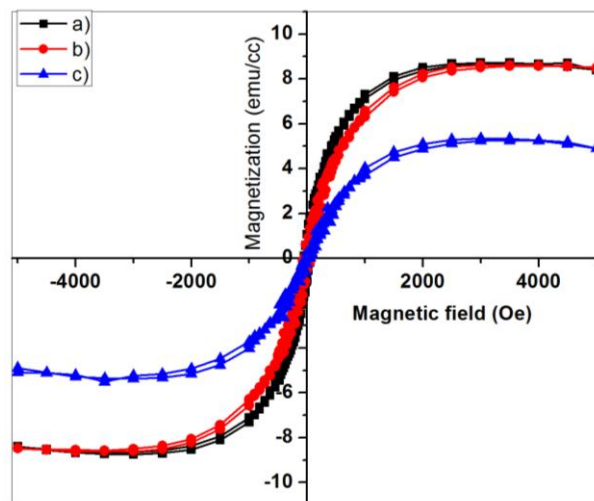


Fig.8 Hysteresis loops of FeNiMoB films a) pristine b) film annealed at 673K and c) 873K

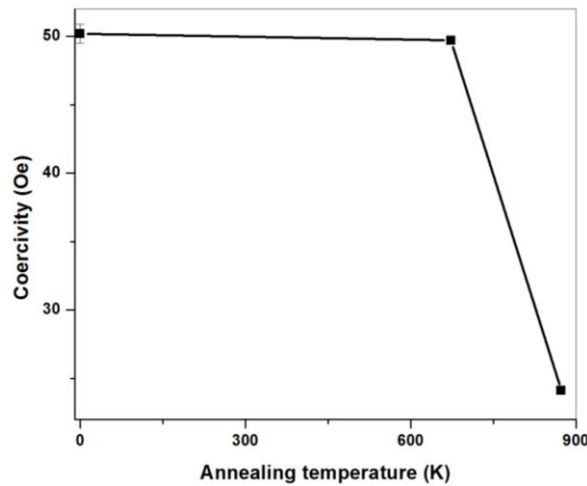


Fig. 9 Variation of coercivity with annealing temperature

FeNiMoB films prepared by RF sputtering exhibited a saturation magnetization ( $M_s$ ) of 8emu/cc and  $M_s$  decreases on annealing at 873K. Compared to bulk ribbons and films deposited by thermal evaporation, the value of  $M_s$  is relatively low. This is because in films prepared by thermal evaporation the predominant phase is Fe-Ni [19-20]. The low value of saturation magnetization of RF sputtered films is due to the presence of predominantly non-magnetic crystalline phase namely  $(\text{FeNiMo})_{23}\text{B}_6$ . The XPS results indicate that the films annealed at 873K have higher oxygen impurity and this further reduces the saturation magnetization. However, the FeNiMoB films exhibited a saturation and hysteresis due to the small fraction of Fe-Ni.

Field cooled and zero field cooled (FC-ZFC) studies were conducted with a view to confirming the ferromagnetic behavior of the films. The results are shown in figure 10. The zero field susceptibility increases with temperature, which is characteristic of a ferromagnetic material.  $T_{\text{irr}}$ , the temperature above

where FC and ZFC bifurcate, was not observed until room temperature. This suggests that the material is ferromagnetic at room temperature and its Curie temperature is above 300K. Even though the predominant phase is  $(\text{FeNiMo})_{23}\text{B}_6$ , a small fraction of Fe-Ni phase contributes to the ferromagnetic behavior of the films.

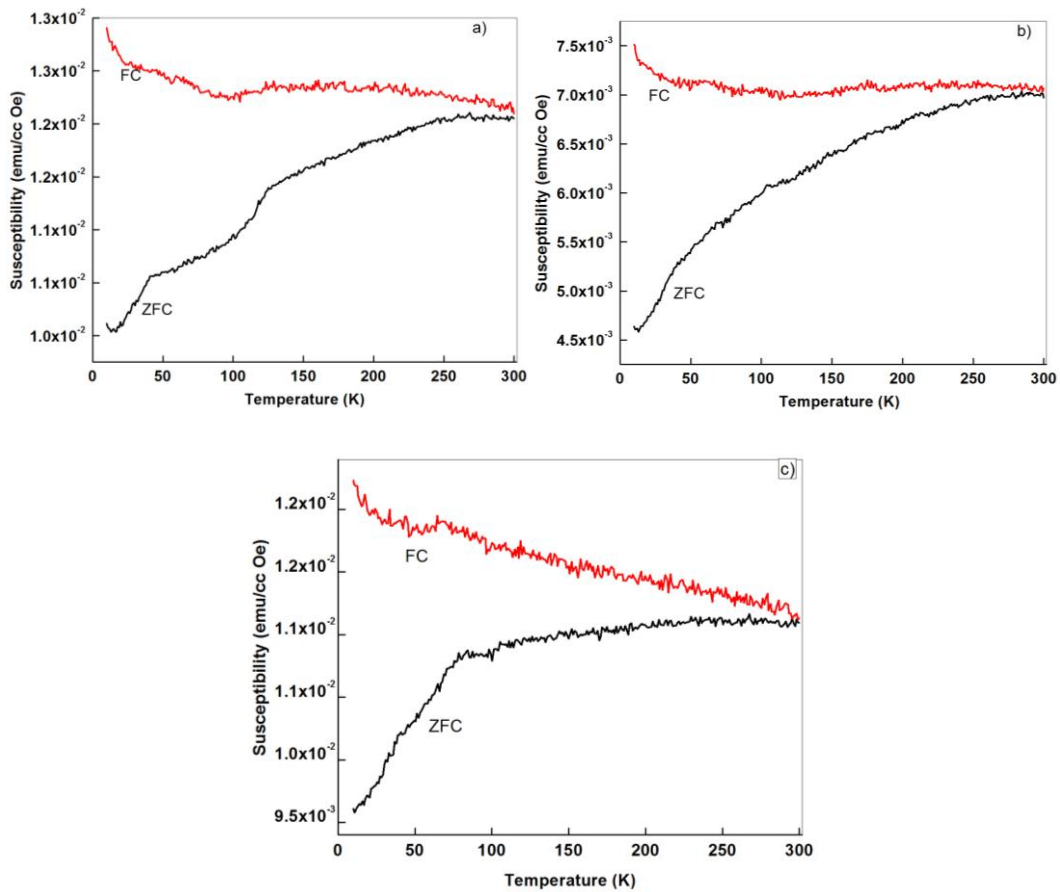


Fig.10 FC- ZFC curves of FeNiMoB film a) pristine b) film annealed at 673K and c) 873K

### 3.4 CONCLUSION

Thin films of FeNiMoB with thickness 52 nm were prepared by RF sputtering and were annealed at 673K and 873K. X ray Photoelectron Spectroscopy studies have confirmed the presence of iron, nickel, boron and molybdenum in thin film. The pristine film was crystalline and predominant phase is  $(\text{FeNiMo})_{23}\text{B}_6$ . GXR D and TEM results indicate that molybdenum has inhibited grain growth in the annealed films. The surface roughness increases with annealing and is due to oriented grain growth. The films were ferromagnetic at room temperature and exhibited hysteresis, but the value of saturation magnetization was low due to the presence of significant volume fraction of the  $(\text{FeNiMo})_{23}\text{B}_6$  phase.

### REFERENCES

- [1] Akihiro Makino, Takashi Hatanai, Yutaka Naitoh, Teruo Bitoh, IEEE Trans. Magn. **33** (1997) 3793
- [2] W. Clement, R.H. Willens, P. Duwez, Nature **187** (1960) 869.
- [3] Giselher Herzer, J. Magn. Magn. Mat. **294** (2005) 99.
- [4] R. Krishnan, Shiva Prasad and K. Branska, J. Appl. Phys. **50** (1979) 7639
- [5] McHenry M E, Willard M A and Laughlin D E, Prog. Mater. Sci. **44** (1999) 291
- [6] S.W. Du, R.V. Ramanujan, J. Non-Cryst. Solids **351** (2005) 3105
- [7] Thomas Hysen, Thomas Senoy, R. V. Ramanujan, M. R. Anantharaman, J Mater. Sci. **43** (2008) 635
- [8] G. Herzer, IEEE Trans. Magn. **26** (1990) 1397
- [9] S.W. Du, R.V. Ramanujan, Mater. Sci. Eng. A **375** (2004) 1040

- [10] R.V. Ramanujan, S.W. Du, J. Alloys Compd. **425** (2006) 251
- [11] Kai-Yuan He, Yu-Hua Zhao, Guo-Gang Li, Li-Zhi Cheng, Bo Wu, Man-Ling Sui, Wen-Zhi Chen, J. Magn. Magn. Mat. **316** (2007) 34
- [12] Kissinger HE, Anal. Chem. **29** (1957) 1702
- [13] Moynihan CT, Eastal AJ, Wilder J, Tucker J, J. Phys. Chem. **78** (1974) 267
- [14] Marseglia EA, J. Non-Cryst. Solids **41** (1980) 31
- [15] Senoy Thomas, Jinesh Mathew, P. Radhakrishnan, V.P.N. Nampoori, A.K. George, S.H. Al Harthi, R.V. Ramanujam, M R Anantharaman, Sens. Actuators A **161** (2010) 83.
- [16] Plamen G. Stoyanov, Craig A. Grim, Sens. Actuators **80** (2000) 8
- [17] Jyothi M and Suryanarayana, C Z. Metallk. **76** (1985) 802
- [18] Cai Liang, Jing Hu, Bart Prorok, Chinthaka Gooneratne, Jürgen Kosel, Mater. Sci. Forum **667** (2011) 1207
- [19] T Hysen, S Deepa, S Saravanan, R V Ramanujan, D K Avasthi, P A Joy, S D Kulkarni and M R Anantharaman, J. Phys. D: Appl. Phys. **39** (2006) 1993
- [20] Senoy Thomas, S H Al-Harthi, D Sakthikumar, I A Al-Omari, R V Ramanujan, Yasuhiko Yoshida and M R Anantharaman, J. Phys. D: Appl. Phys. **41** (2008) 155009
- [21] Hysen Thomas, Senoy Thomas, Raju V. Ramanujan , D.K. Avasthi , I.A. Al- Omari, Salim Al-Harthi, M.R. Anantharaman, Nucl. Instrum. Methods Phys. Res., Sect. B **287** (2012) 85
- [22] Senoy Thomas, Hysen Thomas, D. K. Avasthi, A. Tripathi, R. V. Ramanujan and M. R. Anantharaman, J. Appl. Phys. **105** (2009) 033910

*Chapter 3*

- [23] Parratt L G, Phys. Rev. **95** (1954) 359
- [24] Cai Liang, Development of bulk-scale and thin film magnetostrictive sensor, PhD thesis 2007, Auburn University,
- [25] R. Gavrilă, A. Dinescu, D. Mardare, Rom. J. Inf. Sci. Tech. **10** (2007) 291
- [26] R. Petri, P. Brault, O. Vatel, D. Henry, E. Andre, P. Dumas, F. Salvan, J. Appl. Phys. **75** (1994) 7498
- [27] P. Dash, P. Mallick, H. Rath, A. Tripathi, Jai Prakash, D.K. Avasthi, S. Mazumder, S. Varma, P.V. Satyam, N.C. Mishra, Appl. Surf. Sci. **256** (2009) 558
- [28] Junhua Xu, Lihua Yu, Isao Kojima, J. Appl. Phys. **94** (2003) 6827

## Chapter 4

### **Tailoring topographical and magnetic properties of FeNiMoB films by 100 MeV Ag ions Swift Heavy Ion irradiation**

#### 4.1 Introduction

#### 4.2 Experimental Methods

#### 4.3 Results and Discussions

- Simulation Studies: Stopping Range of Ions in Matter (SRIM)
- Thickness and Compositional analysis: Rutherford backscattering Spectrometry (RBS)
- Structural Characterization: Glancing Angle X Ray Diffractometer (GXRD)
- Topographical Studies: Atomic Force Microscope (AFM)
- Magnetic studies: Super conducting Quantum Interferometer Device-Vibrating Sample Magnetometer (SQUID-VSM)

#### 4.4 Conclusion

#### References

*Chapter 4*

#### **4.1 INTRODUCTION**

The properties of metallic glasses and preparation of FeNiMoB based thin films by RF sputtering have been discussed in Chapter 3. Even though we have succeeded in retaining all the target elements in thin film, the magnetization obtained was quite low. With a view to improving the magnetic properties, the films are subjected to swift heavy ion irradiation. The technique of using ion irradiation to tailor properties of metallic glasses have been reported earlier [1-2]. Ion irradiation can generate highly localized damage to the target material. Energy of 1eV corresponds to 11000 K of temperature; ions having energy of the order of MeV transmit much higher temperatures to the target material, which can melt material along the ion track. Subsequent cooling (within ~100ps) as soon as ions pass through occurs and this can cause amorphisation of target material [3]. This highly non equilibrium process cannot be achieved by any other technique.

Apart from amorphisation, ion irradiation also causes significant changes in topography. When ions are bombarded on a target surface, many processes take place like sputtering, defect formation, ion implantation, track formation and ionization. When the incoming ions transmit higher energies to the target atom on the surface, the atoms can overcome the surface binding energy and sputtering of atoms from the surface takes place. Usually, sputtering results in surface roughening. When the atoms do not acquire enough energy, they diffuse through the surface and causes surface smoothing. This was observed in many systems [10-14].

The structural and topographical changes induced as a result of ion irradiation can cause significant changes in magnetic properties of materials [4]. Inducing amorphisation in material can enhance the magnetic properties. Metallic

glass with a composition of  $\text{Fe}_{40}\text{Ni}_{38}\text{Mo}_4\text{B}_{18}$  is a well known soft magnetic material. They are amorphous in nature and their nanocrystalline structures exhibit good soft magnetic properties, as the grain size is less than the exchange correlation length. In the previous chapter, we discussed preparation of FeNiMoB films by RF sputtering which exhibited crystalline nature contrary to the amorphous nature of target used and the crystalline FeNiMoB phase is non magnetic in nature. The magnetisation obtained was relatively low compared to the bulk and there are possibilities that magnetisation can enhance on amorphisation. Keeping this in mind, swift heavy ion irradiation was adopted as a tool to modify the properties.

In the present chapter we report preparation of FeNiMoB films from  $\text{Fe}_{40}\text{Ni}_{38}\text{Mo}_4\text{B}_{18}$  and subsequent irradiation with 100 MeV Ag ions. The structural, topographical and magnetic evolution with ion irradiation is discussed.

## 4.2 EXPERIMENTAL METHODS

Films based on FeNiMoB were prepared from  $\text{Fe}_{40}\text{Ni}_{38}\text{Mo}_4\text{B}_{18}$  employing RF sputtering method on naturally oxidized silicon substrate. An RF power of 100 W for 30 minutes in an argon atmosphere was utilized for deposition. The thickness and composition of the deposited films were determined using RBS. The films were irradiated at fluences of  $1 \times 10^{12}$ ,  $1 \times 10^{13}$  and  $3 \times 10^{13}$  ions/cm<sup>2</sup> using 100 MeV Ag ions. The energy loss and range of ions in the material was simulated using Stopping Range of Ions in Matter- SRIM 2008 [5]. The films were characterized using Glancing X-Ray Diffractometer (GXR D Bruker Discover D-8) with Cu K $\alpha$  ( $\lambda=1.5406\text{\AA}$ ) at a glancing angle of  $0.5^\circ$ . The crystallite size was estimated using Scherrer relation. The topographical studies were carried out using Atomic Force Microscope (AFM Digital Instruments

Nanoscope). A detailed study on surface roughness and Power Spectral Density (PSD) analysis were done with the help of offline software. The magnetic hysteresis loop at room temperature was measured using 7T MPMS Quantum Design Interferometer Device-Vibrating Sample Magnetometer (SQUID-VSM).

### **4.3 RESULTS AND DISCUSSIONS**

The electronic energy loss and range of ions was determined using SRIM software and is depicted in figure 1. The electronic energy loss is estimated as 0.016 MeV/nm and range of ions was 11 $\mu$ m. The range is much greater than film thickness and therefore ions get buried deep in the substrate.

The film thickness estimated from RBS (figure 2) is found to be 450 nm. The composition of the film is 18.4% Fe, 18.4% Ni, 2.3% Mo and 61% O.

GXRD pattern of pristine film (figure 3) indicate formation of FeNiMoB phase. This phase is reported to be nonmagnetic [6-7]. The crystallite size of pristine film was found to be 70 nm. On irradiation, this peak disappears owing to amorphisation of the films. SHI induced amorphisation in materials is quite common and has been explained using the thermal spike model [8-9].

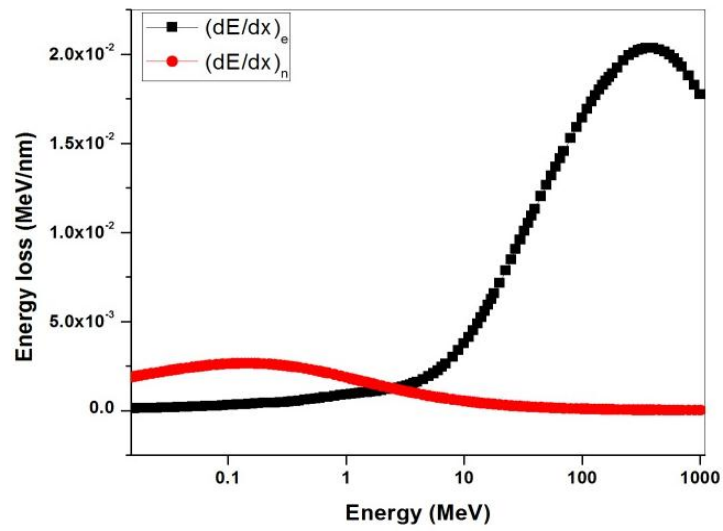


Fig. 1 SRIM simulation of 100 MeV Ag ions in FeNiMoB

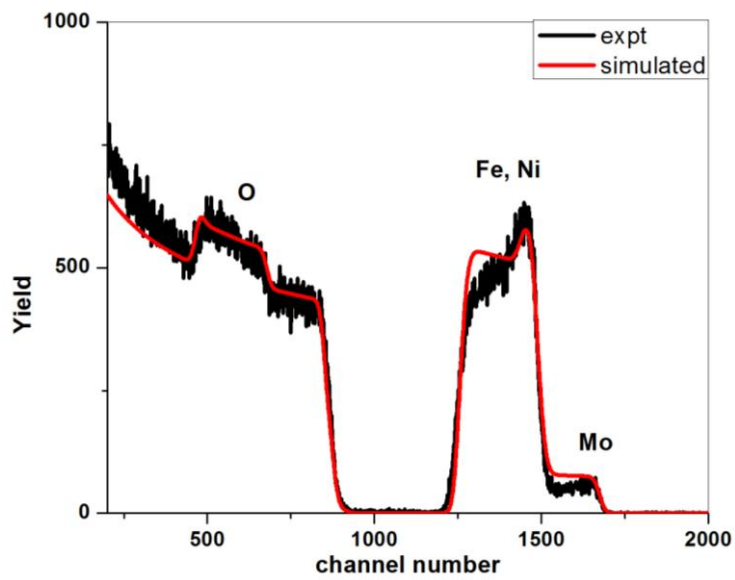


Fig. 2 RBS spectrum of pristine film

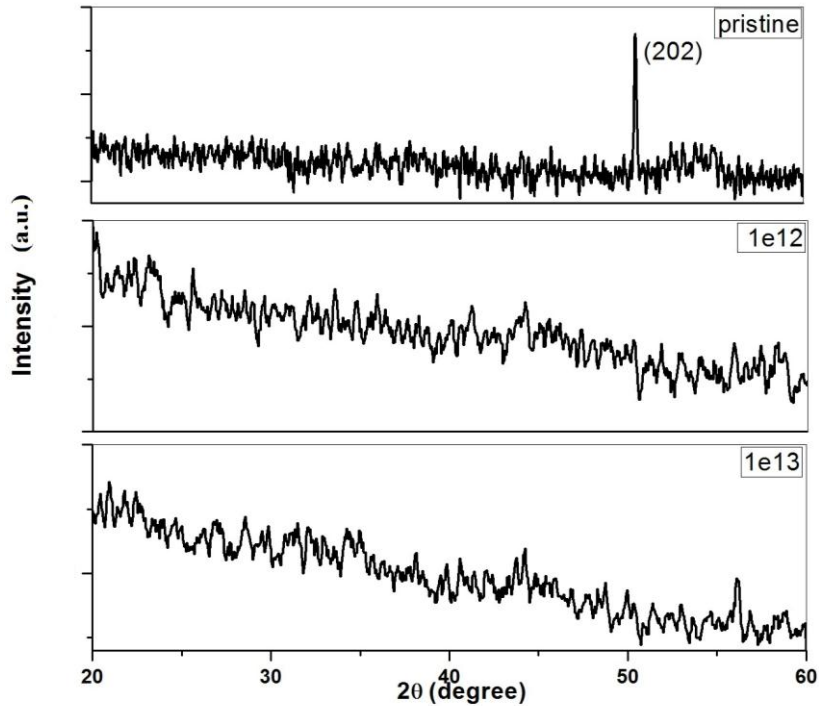


Fig. 3 GXR D pattern of FeNiMoB a) pristine film and films irradiated at fluences of b)  $1 \times 10^{12}$  and c)  $1 \times 10^{13}$  ions/cm<sup>2</sup>

AFM images of pristine and irradiated films shown in figure 4 indicate modification of surface topography with ion fluence. From the 3D AFM images (figure 5), we can observe that the density of hill like structures decreased at lower fluences and increased at higher fluence.

The variation of roughness and grain size with ion fluence is plotted in figure 6. Initially, a grain growth was observed with fluence and at higher fluence the grain size decreases. The surface roughness decreases with ion fluence, and then at the highest fluence, the roughness increases.

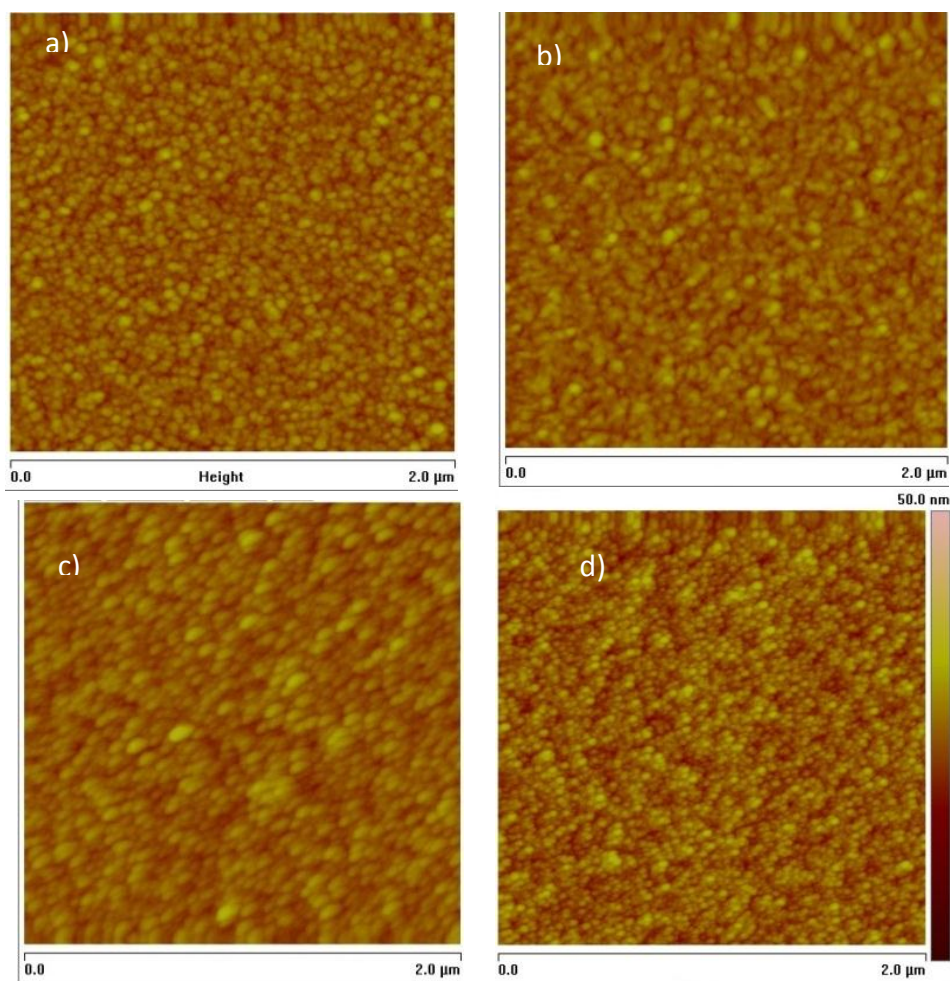


Fig. 4 AFM images of a) pristine film and film irradiated at fluences of b)  $1 \times 10^{12}$   
c)  $1 \times 10^{13}$  d)  $3 \times 10^{13}$  ions/cm<sup>2</sup>

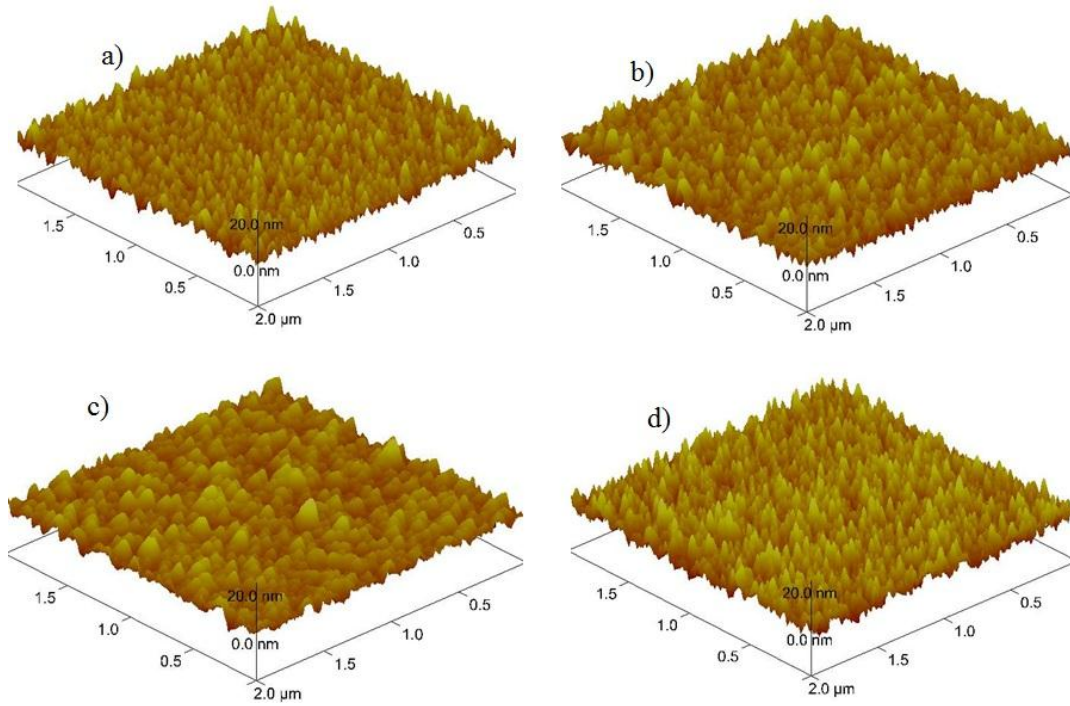


Fig. 5 3D AFM images of a) pristine film and film irradiated at fluences of b)  $1 \times 10^{12}$  c)  $1 \times 10^{13}$  d)  $3 \times 10^{13}$  ions/cm<sup>2</sup>

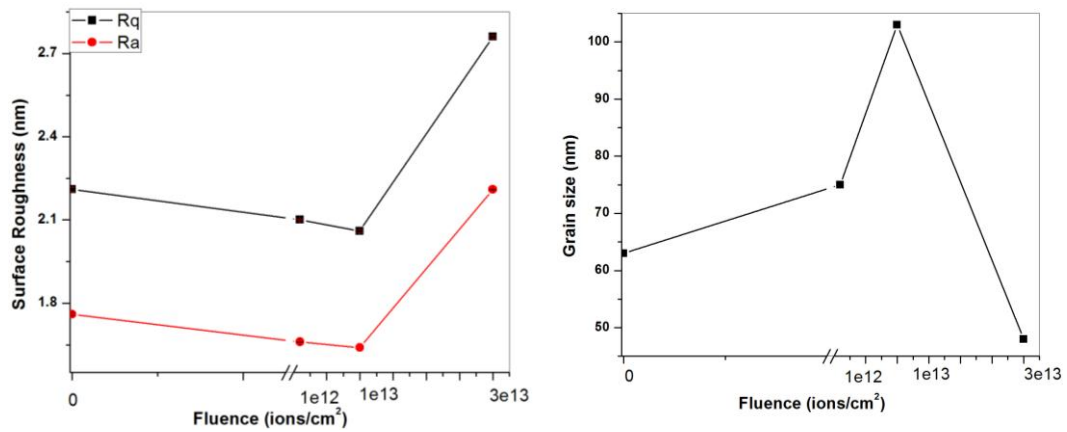


Fig. 6 Variation of roughness and grain size with ion fluence

## Chapter 4

During ion irradiation, sputtering of the film surface occurs and if energy of the sputtered atoms is greater than surface binding energy, atoms escape from the surface. This causes evaporation and results in surface roughening. If the energy of atoms is not enough to escape the binding force, the atoms drift through the surface which results in surface smoothing [10]. Depending upon fluence, energy of ion used, energy loss and type of material, one may observe either surface roughening or surface smoothing. We observe surface smoothing at low fluence and surface roughening at higher fluence. Same behavior was observed by Hysen *et al.* on thermally evaporated metallic glass thin films [11]. P Mallick *et al.* has observed surface roughening at low fluence and smoothing at higher fluence on NiO thin films [12]. Carter *et al.* have reported that at normal incidence conditions surface smoothing occurs as sputtering yield is low under these conditions [13]. Gupta *et al.* have also observed similar behavior on gold films [14]. In our case at lower fluences, surface smoothing occurs due to diffusion and at higher fluence, sputtering of the surface occurs and results in surface roughening. To elucidate the possible surface mechanism AFM images were subjected to PSD analysis.

Depending upon the slope  $\delta$  of PSD curve, Herring and Mullins have defined four different transport mechanisms [17-18].  $\delta$  values of 1, 2, 3, 4 indicate plastic flow driven by surface tension, evaporation-condensation, volume diffusion and surface diffusion respectively as the transport mechanisms. PSD spectra of pristine and irradiated films are shown in figure 7. The  $\delta$  values obtained in our case are nearly 2 for initial fluence and between 2 and 2.5 at the highest fluence. This suggests that the dominant mechanism for smoothing at

lower fluence is plastic flow driven by surface tension, while evaporation-condensation at highest fluence causes an increase in surface roughness.

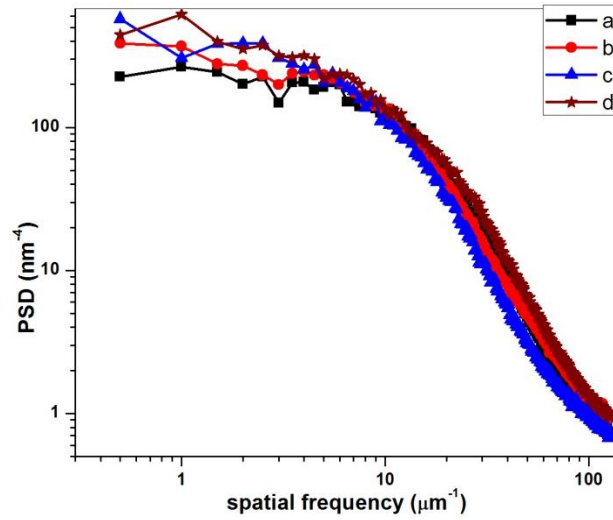


Fig. 7 Power spectral density of a) pristine film and film irradiated at fluences of b)  $1 \times 10^{12}$  c)  $1 \times 10^{13}$  d)  $3 \times 10^{13}$  ions/cm<sup>2</sup>

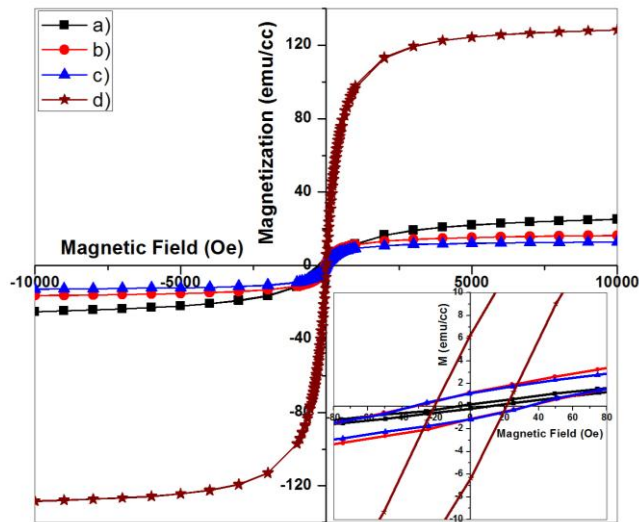


Fig. 8 Room temperature hysteresis of a) pristine film and film irradiated at fluences of b)  $1 \times 10^{12}$  c)  $1 \times 10^{13}$  d)  $3 \times 10^{13}$  ions/cm<sup>2</sup>

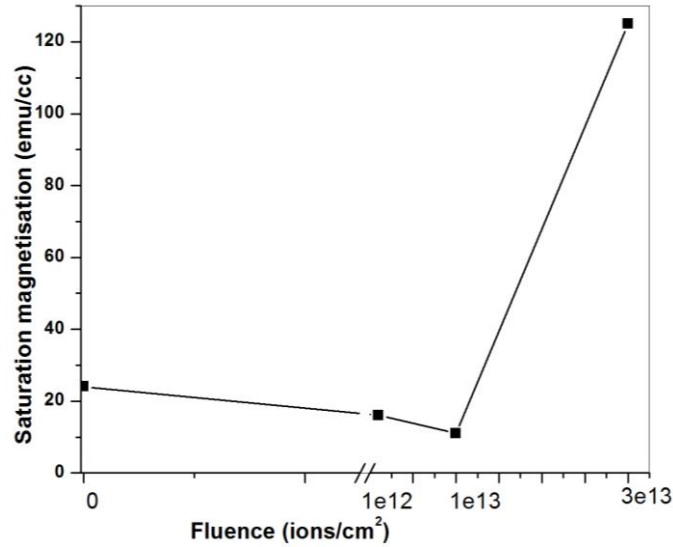


Fig. 9 Variation of saturation magnetization with ion fluence

Room temperature magnetic measurements of the pristine and irradiated samples are shown in figure 8. The pristine film exhibited a saturation magnetization of 24emu/cc. On irradiation at lower fluences,  $M_s$  decrease and then increase to 125emu/cc for the highest fluence of  $3 \times 10^{13}$  ions/cm<sup>2</sup>. The variation of coercivity cannot be quantified, as the coercivity values are small (~25 Oe) and variation will be within the error bars. An increase in remanent magnetization is observed with ion fluence. The amorphisation of films with ion irradiation have weakened the non magnetic FeNiMoB phase, and the amorphousity could enhance the magnetisation [4]. If that is the case, magnetization should also increase at lower fluences of  $1 \times 10^{12}$  and  $1 \times 10^{13}$  ions/cm<sup>2</sup>. More than amorphisation, the effect of grain size plays a prominent role in influencing

magnetization. From AFM images, the grain size was found to increase at lower fluence and then substantial decrease was observed for the highest fluence of  $3 \times 10^{13}$  ions/cm<sup>2</sup>. According to Herzer model for amorphous alloys, if grain size is less than the exchange length, saturation magnetization and coercivity scales as the sixth power of grain size D, and for larger grains, coercivity and magnetization is inversely proportional to D [19]. Usually for Fe based alloys exchange length is less than 40 nm [20]. In the present case, from AFM studies grain sizes were greater than 50 nm, and hence the magnetization should inversely vary with D. The smallest grain size obtained is for the highest fluence, and at this particular fluence magnetization is maximum.

#### **4.4 CONCLUSION**

Films of FeNiMoB alloy having thickness 450 nm was prepared from a composite target of Fe<sub>40</sub>Ni<sub>38</sub>Mo<sub>4</sub>B<sub>18</sub> employing RF sputtering and were irradiated with 100MeV Ag ions at fluences of  $1 \times 10^{12}$ ,  $1 \times 10^{13}$  and  $3 \times 10^{13}$  ions/cm<sup>2</sup>. The pristine film was crystalline in nature and on ion irradiation, amorphisation was induced. The surface roughness initially decreases and then increases for the highest fluence indicating surface smoothing at lower fluence and roughening at higher fluence. The grain size calculated from AFM indicates initial increase and then decreases for the highest fluence. The as deposited films were exhibiting low magnetisation due to the presence of crystalline FeNiMoB phase. On irradiation the phase disappears and along with decrease in grain size for the highest fluence a very high magnetization was observed for the sample irradiated at  $3 \times 10^{13}$  ions/cm<sup>2</sup>. The enhancement of magnetization on irradiation at a particular fluence is rather intriguing and needs extensive investigation.

**REFERENCES:**

- [1] T. Hysen, P. Geetha, S. Al-Harathi, I. A. Al-Omari, R. Lisha, R.V. Ramanujan, *J. Magn. Magn. Mater.* **372** (2014) 224
- [2] G. Pookat, T. Hysen, S. Al-Harathi, I.A. Al-omari, R. Lisha, D.K. Avasthi, *Nucl. Instru. Methods Phys. Res. Sect. B Beam Interact. with Mater. Atoms* **310** (2013) 81
- [3] *Swift heavy ions for materials engineering and nanostructuring*, D K Avasthi, G K Mehta, Springer series (2011)
- [4] J P Nozieres, M. Ghidini, N.M. Dempsey, B. Gervais, D. Givord, G. Suran, J.M.D. Coey **146** (1998) 250
- [5] Ziegler J F, Biersack, J P, Littmark U, *The Stopping and Range of Ions in Solids* (New York: Pergamon) SRIM code: <http://www.srim.org> (1985)
- [6] R. Lisha, T. Hysen, P. Geetha, D.K. Avasthi, R. V Ramanujan, M.R. Anantharaman, *Mater. Res. Express.* **1** (2014) 015707.
- [7] S.W. Du, R. V Ramanujan, *J. Non-cryst. Solids.* **351** (2005) 3105
- [8] G. Szenes, Z. Horváth, B. Pécz, F. Pászti, L. Tóth, *Phys. Rev. B.* **65** (2002) 045206
- [9] C. Dufour, E. Paumier, M. Toulemonde, *Nucl. Instru. Methods Phys. Res. Sect. B Beam Interact. with Mater. Atoms* **122** (1997) 68
- [10] D. Goswami, B. Dev, *Phys. Rev. B.* **68** (2003) 033401
- [11] H. Thomas, S. Thomas, R. V. Ramanujan, D.K. Avasthi, I. a. Al- Omari, S. Al-Harathi, *Nucl. Instru. Methods Phys. Res. Sect. B Beam Interact. with Mater. Atoms* **287** (2012) 85.
- [12] P. Mallick, D.C. Agarwal, C. Rath, D. Behera, D.K. Avasthi, D. Kanjilal, *Radiat. Phys. Chem.* **81** (2012) 647

- [13] G. Carter, V. Vishnyakov, Phys Rev B. **54** (1996) 647
- [14] A. Gupta, D. Avasthi, Phys. Rev. B. **64** (2001) 155407.
- [15] R. Gavrilă, A. Dinescu, D. Mardare, Rom. J. Inf. Sci. Technol. **10** (2007) 291
- [16] P. Dash, P. Mallick, H. Rath, A. Tripathi, J. Prakash, D.K. Avasthi, Appl. Surf. Sci. **256** (2009) 558.
- [17] C. Herring, J. Appl. Phys. **21** (1950) 301
- [18] W.W. Mullins, J. Appl. Phys. **30** (1959) 77
- [19] G. Herzer, V. Gmbh, D.- Hanau, F.R. Germany, IEEE Trans. Magn. **2626** (1990) 139
- [20] G. Herzer, Proceedings of the NATO Advanced Study Institute on Magnetic Hysteresis in Novel Materials, 1996

*Chapter 4*

## Chapter 5

### **On the room temperature ferrimagnetism in RF sputtered zinc ferrite thin films and disorder effects at low temperature**

#### 5.1 Introduction

#### 5.2 Experimental Methods

#### 5.3 Results and discussions

- Thickness and compositional analysis: Rutherford Backscattering Spectrometry (RBS)
- Structural Characterization: Glancing angle X-ray Diffractometer (GXRD), Transmission Electron Microscope (TEM) & Selected Area Electron Diffraction (SAED)
- Topographical studies: Atomic Force Microscope (AFM)
- Magnetic studies: Super conducting Quantum Interferometer Device-Vibrating Sample magnetometer (SQUID-VSM)

#### 5.4 Conclusion

#### References

*Lisha R. et al. Journal of Magnetism and Magnetic Materials 385 (2015) 265–271*

*Chapter 5*

## 5.1 INTRODUCTION

Zinc ferrite is an antiferromagnet with a Neel temperature of 10 K and exhibits a normal spinel structure with  $\text{Zn}^{2+}$  ions having exclusive tetrahedral site (A site) preference while  $\text{Fe}^{3+}$  ions occupy the octahedral site (B site) in an fcc close packed oxygen sub lattice [1]. The magnetic ions are present in the B site and the magnetic property is due to interaction of ions in B site ( $J_{\text{BB}}$ ) and the antiferromagnetism is attributed to weak  $J_{\text{BB}}$  interaction. Zinc ferrite with a normal spinel structure can be represented by  $\text{Zn}^{2+}_{\text{A}}\text{Fe}^{3+}_{\text{B}}\text{O}_4^{2-}$ . Several anomalies exist as regards the magnetic properties of zinc ferrite. Kamazawa *et al.* reported that normal spinel zinc ferrite is not an antiferromagnet but a three dimensional spin frustrated magnet [2]. In the nano scale, zinc ferrite exhibits altogether different properties and has been attributed to cation redistribution where in some amount of  $\text{Zn}^{2+}$  ions migrate to the B site and an equal amount of  $\text{Fe}^{3+}$  ions migrate to the A site resulting in a  $J_{\text{AB}}$  interaction. The varied properties of nano zinc ferrite can also be ascribed to surface effects or surface magnetism [3, 4, 5]. Low Energy Ion Scattering (LEIS) studies on spinel structures revealed that it is the octahedral site that is preferentially exposed on the surface [6]. The cation distribution in the nano regime was observed to be synthesis specific [7-9]. The cation redistributed spinels can be represented by  $[\text{Zn}_{1-x}^{2+}\text{Fe}_x^{3+}]_{\text{A}}[\text{Zn}_x^{2+}\text{Fe}_{2-x}^{3+}]_{\text{B}}\text{O}_4^{2-}$ , where x represents the degree of cation disorder/percolation depth.

Studies on zinc ferrites are still a hot topic of research due to the varied and inconsistent results obtained by different groups [10-16]. For example, Nakashima *et al.* prepared zinc ferrite thin films by RF sputtering and they observed coexistence of ferrimagnetic ordering and glassy behavior [9]. Bohra *et*

*al.* carried out systematic studies on zinc ferrite thin films prepared by RF sputtering and pulsed laser deposition and they obtained high magnetization but the film do not saturate even in the highest applied field [17]. Yamamoto *et al.* realized room temperature cluster glass state in zinc ferrite thin films prepared by Pulsed Laser Deposition. They investigated the role of deposition rate on the magnetic properties of these thin films. The room temperature spin glass property has been found useful in making magneto optic memory devices [7]. Recently Liang *et al.* reported deposition of zinc ferrite thin films on various substrates. They obtained a saturation magnetization of  $1.5 \times 10^{-3}$  emu/cc for a 120 nm film [18] which is very small for any useful application.

It is in this context that a thorough investigation on zinc ferrite thin films assumes importance. Thermal annealing of RF sputtered zinc ferrite thin films can modify structural, surface and magnetic properties substantially. Moreover the effect of annealing on the cation redistribution, if any, can also be investigated. In the present study, zinc ferrite thin films were prepared by RF sputtering. The structural and magnetic properties of zinc ferrite thin films and the effect of thermal annealing on the magnetic properties were investigated.

## **5.2 EXPERIMENTAL METHODS**

Zinc ferrite thin films were coated on silicon substrate by RF sputtering from a phase pure zinc ferrite target. The phase pure target employed for sputtering was in turn prepared by sol gel auto combustion technique using zinc nitrate and ferric nitrate as precursors. This was dissolved in ethylene glycol by adding the solvent under constant stirring at 343K and the obtained sol was heated at 393K until auto combustion took place. The powder thus obtained was then annealed at 973K for 24 hours and then pressed into pellets of 2 inch diameter.

*On the room temperature.....*

The sputtering was carried out in an Argon atmosphere with an RF power of 150 watts for 90 minutes. Vacuum of  $5 \times 10^{-5}$  Torr was attained with the help of a turbo pump backed by a scroll pump and during deposition the pressure increased to  $2 \times 10^{-2}$  Torr. The films thus obtained were annealed at 673K and 873K for 1 hour in air. Rutherford Backscattering spectrometry (RBS) was employed to determine the thickness and composition of films. The experimental results are fitted using XRUMP software to obtain thickness and composition [19]. Structural characterization of films were carried out using Glancing X-Ray Diffractometer (GXRD) Bruker Discover D-8 with Cu  $K\alpha$  ( $\lambda=1.5406\text{\AA}$ ) radiation at a glancing angle of  $1^\circ$ . The crystallite size was calculated using Scherrer formula. Micro structural characterization was carried out using Transmission Electron Microscope (TEM) and Selected Area Electron Diffraction (SAED). Nanoscope IIIa Digital Instruments, Veeco was employed for surface morphology studies. Room temperature and low temperature magnetic measurements were conducted employing a 7 Tesla MPMS SQUID - VSM. MH loops at room temperature and at 10K were traced. Field cooled –Zero field cooled (FC-ZFC) measurements were carried out at a cooling field of 100 Oe and 1000 Oe.

### **5.3 RESULTS AND DISCUSSIONS**

The thickness of the pristine film estimated using RBS data is around 120 nm. The weight percentage of elements is found to be 12.5% Zn, 25% Fe, 62.5 % O. A ratio of 1:2 of Zn:Fe is achieved in thin films, which is identical to the target composition. The thickness and composition of films do not vary on annealing which suggest that the films are uniform. RBS spectra for pristine and annealed films are depicted in Figure 1.

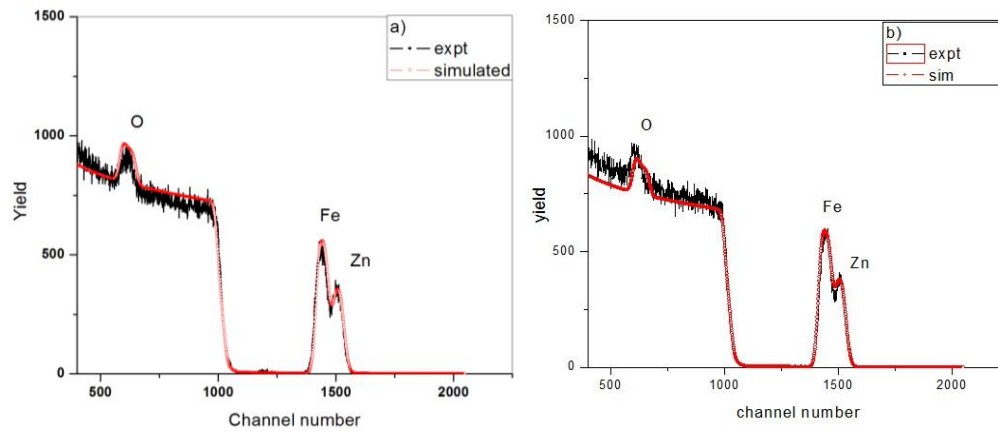


Fig. 1 RBS Spectrum zinc ferrite film a) pristine and b) annealed at 873K

The GXR D pattern is shown in figure 2. GXR D results of pristine film exhibits a broad peak at  $35^{\circ}$  and on annealing at 873K, the peak corresponding to (311) plane becomes prominent and the crystallite size calculated using Scherrer formula was  $\sim 18.2$  nm. To support the results from GXR D, SAED measurements were performed and are shown in figure 3a and 3b. The d values are compared with the standard d values of zinc ferrite and are in good agreement. The (311) planes are clearly visible in the SAED pattern of pristine film, which could not be detected in the case of GXR D [20]. The particle size calculated from TEM is  $12 \pm 1.3$  nm and  $16 \pm 1.9$  nm for pristine and film annealed at 873K respectively (fig 3c-3f). Thus we observe that zinc ferrite films are crystalline in nature and the grains grew in size with increase in annealing temperature which is on expected lines.

*On the room temperature.....*

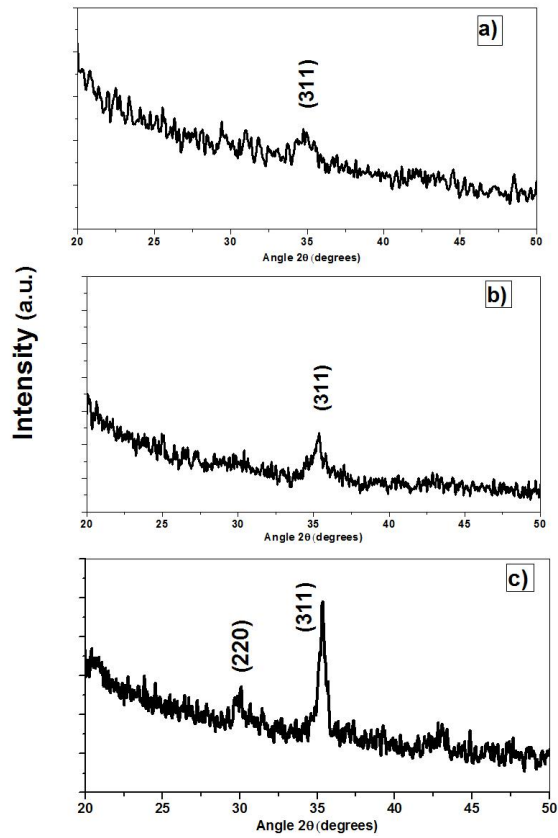


Fig. 2 GXR D pattern of zinc ferrite film a) pristine b) film annealed at 673K and c) 873K

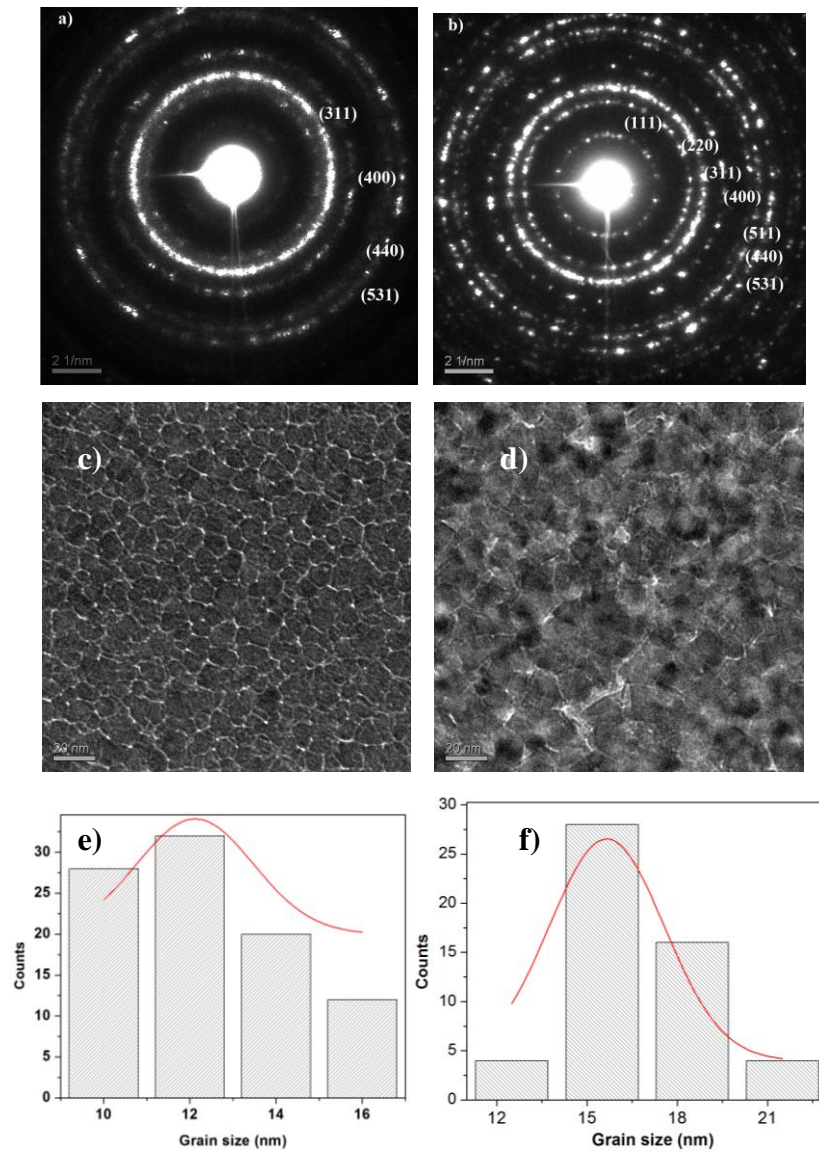


Fig. 3 SAED images of zinc ferrite film a) pristine and b) annealed at 873K. TEM image of c) pristine and d) film annealed at 873K. Grain size distribution of e) pristine and f) film annealed at 873K

*On the room temperature.....*

AFM images of pristine and film annealed at 873K are shown in figure 4. The pristine film is smooth with an rms roughness of  $0.7\pm 0.01$  nm and on annealing at 873K, the roughness increases to  $2.8\pm 0.2$  nm. This increase in surface roughness is indicative of a annealing assisted grain growth which was also observed from TEM images.

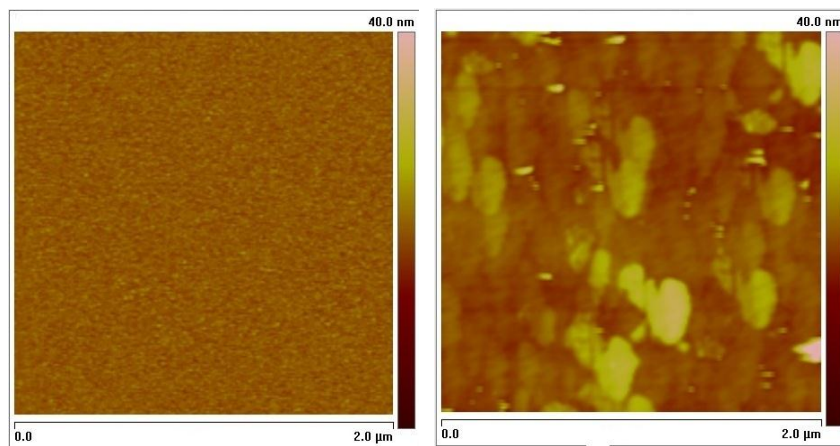


Fig. 4 AFM images of pristine and film annealed at 873K

Room temperature magnetic measurements (Figure 5) indicate that zinc ferrite films exhibit saturated hysteresis loops, saturating at low magnetic field and are therefore ferrimagnetic in nature. The ferrimagnetic behavior could be due to the random arrangement of  $\text{Fe}^{3+}$  ions in both A and B sites as a result of sputtering, which leads to a strong A-O-B interaction. The highest value of saturation magnetization ( $M_s$ ) obtained in our case is 18 emu/cc for the pristine film, which is relatively high. Liang *et al.* deposited zinc ferrite films on various substrates and found that zinc ferrite deposited on silicon substrate yielded an  $M_s$

of  $1.5 \times 10^{-3}$  emu/cc for a thickness of 120 nm and the film were not saturating even at an applied field of 8000 Oe [18]. It must be noted here that in our case pristine zinc ferrite thin film exhibited a much higher  $M_s$  than that of the samples (same thickness) cited in ref. 18.

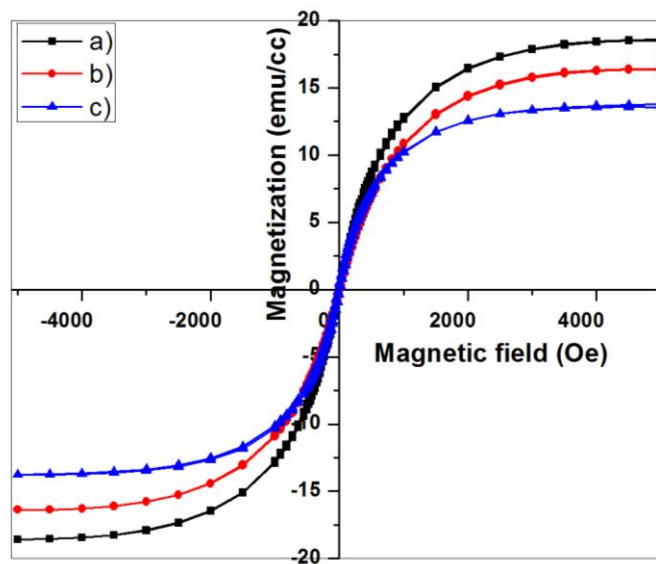


Fig. 5 Room temperature hysteresis curves of zinc ferrite film a) pristine b) film annealed at 673K and c) 873K

A monotonous decrease in saturation magnetization was observed with annealing (fig 6). Other researchers have also observed a similar trend and have explained this due to the remigration of  $Fe^{3+}$  ions to B site with annealing and revert to the normal spinel structure [10]. D Guo *et al.* reported that the saturation magnetization decreased on annealing at 673K, and at 873K, the films tend to be paramagnetic at room temperature. These changes on annealing were attributed to redistribution of ions back to normal spinel structure [21]. In the present study,

even though  $M_s$  decreases on annealing, zinc ferrite thin films retained its ferrimagnetic characteristics even after annealing at 873K which suggest that  $J_{AB}$  interaction is dominating and the ions have not completely reverted back to the normal spinel configuration.

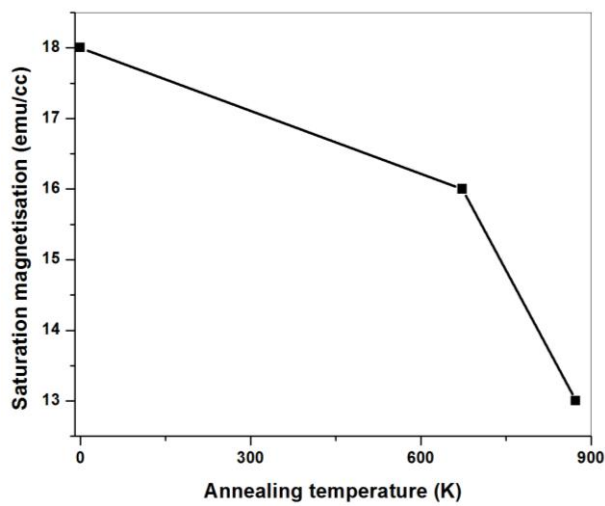


Fig. 6 Variation of saturation magnetization with annealing temperature (Lines are guide to the eye).

Hysteresis loops at 10K (figure 7) was measured to understand the low temperature magnetic ordering. The films exhibited well defined hysteresis loops with large remanence and coercivity characteristic of a ferrimagnetic ordering at 10K. The saturation magnetization, remanence and coercivity decreases on annealing at 873K.

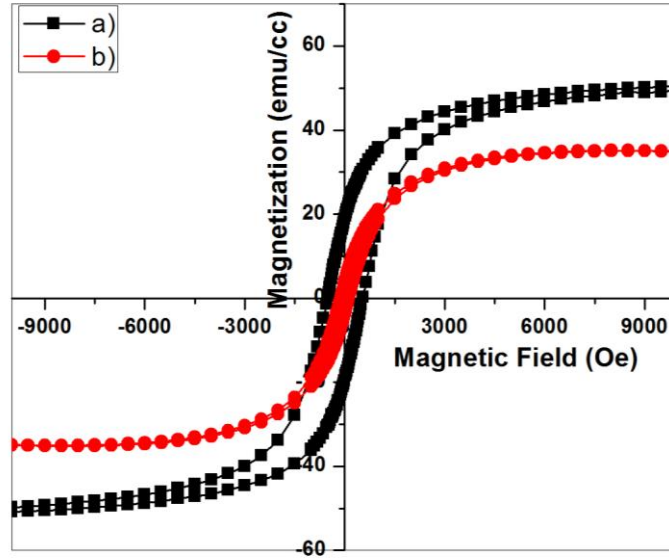


Fig. 7 MH at 10K of zinc ferrite film a) pristine and b) annealed at 873K

To inspect the existence of magnetic ordering in zinc ferrite thin films, they were subjected to FC-ZFC measurements at cooling fields of 100 Oe and 1000 Oe. FC-ZFC studies (figure 8) indicate that the maximum of the ZFC curve which is called the blocking temperature  $T_B$ , shifts to lower temperatures with annealing.  $T_B$  for the pristine film is 85 K and for the film annealed at 873K is 30 K. Blocking temperature for pristine film is higher than that of bulk zinc ferrite which is indicative of a cation redistribution. The shift in blocking temperature with annealing temperature has been attributed to cation disorder in zinc ferrite samples [5]. Disordered zinc ferrite is represented as  $[Zn_{1-x}^{2+}Fe_x^{3+}]_A [Zn_x^{2+}Fe_{2-x}^{3+}]_B O_4^{2-}$ . Nakashima *et al.* had carried out theoretical and experimental studies on the disordered cation distribution in zinc ferrite thin films [22]. They obtained an  $x$  value for normal spinel as  $x=0$  and  $x=0.66$  for completely disordered spinel.

They observed that for film deposited using sputtering the x value corresponds to 0.66 and with annealing the value of x decreases. This change in x was correlated with change in blocking temperature. From the above discussion it is clear that in our work also value of x changes with annealing which is evident from the shift in  $T_B$ .

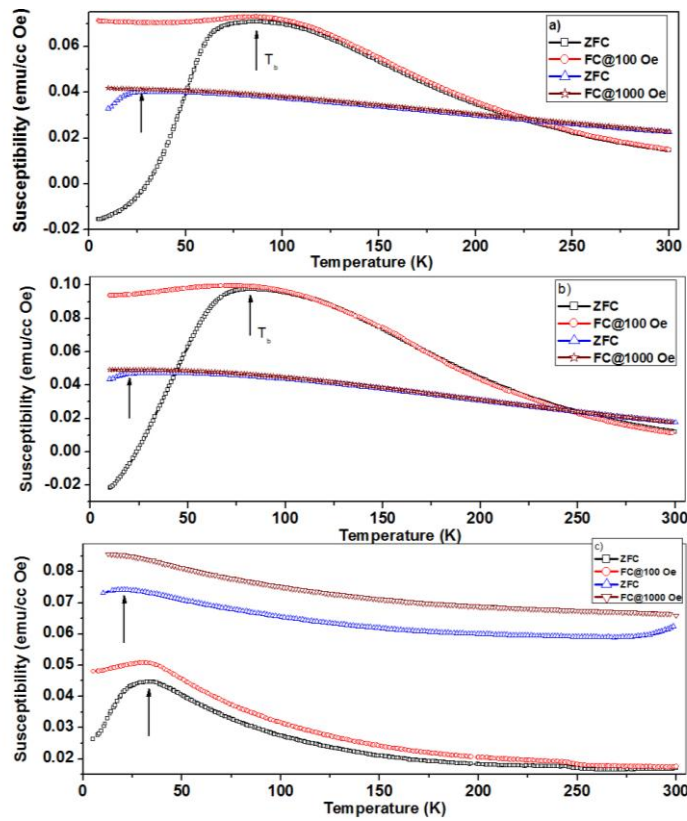


Fig. 8 FC-ZFC curves of zinc ferrite film a) pristine b) film annealed at 673K and c) 873K

$T_{irr}$  which is the temperature, at which FC and ZFC curve bifurcate, also undergo changes with annealing. For films annealed at 873K,  $T_{irr}$  is greater than room temperature. The wide difference between FC and ZFC below  $T_{irr}$  is typical

of disordered systems.  $T_B$  and  $T_{irr}$  shifts to lower temperatures with increase in cooling field. R N Bhowmik *et al.* has attributed this to blocking phenomena in ferrimagnetic nanoparticles [23]. For the pristine and 673K annealed sample, the shift in  $T_B$  is quite large, while for the sample annealed at 873K the shift is very less. However the samples annealed at 873K show marked deviation in FC-ZFC behavior from other samples. The behavior of FC-ZFC curves of this sample is similar to that of bulk zinc ferrite. S Nakashima *et al.* also encountered a similar observation for the zinc ferrite film annealed at 873K [10]. Also around 230K, FC-ZFC susceptibilities almost become constant which is due to ferrimagnetic ordering. Ferrimagnetic ordering was also observed from magnetic measurements at room temperature. The increase in FC with decrease in temperature is indicative of a ferrimagnetic behavior of the system.

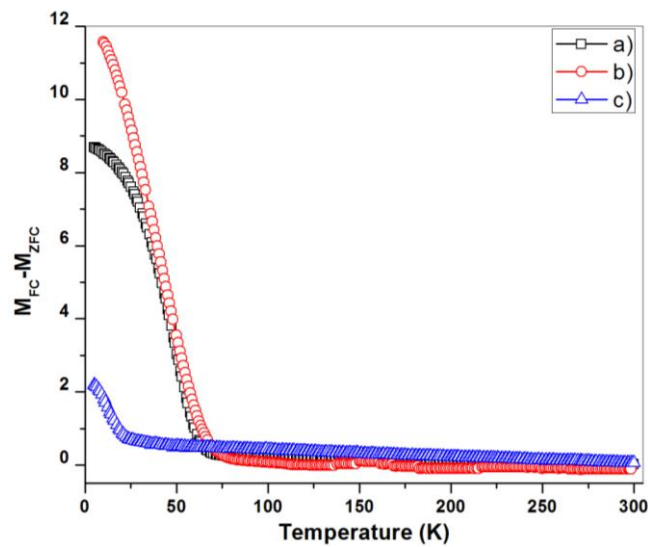


Fig. 9 ( $M_{FC}-M_{ZFC}$ ) v/s Temperature of zinc ferrite thin films a) pristine b) film annealed at 673K and c) 873K

*On the room temperature.....*

The difference between  $M_{FC}$  and  $M_{ZFC}$  ( $\Delta M$ ) is plotted against temperature and is shown in figure 9. The difference is found to be highest for film annealed at 673K. In pristine and film annealed at 673K, the value of  $\Delta M$  starts to increase around 70K. In the film annealed at 873K,  $\Delta M$  increases below 30K. The large magnitude of  $\Delta M$  is indicative of disorder effects [23]. The onset of disorder changes with annealing. At 5K the disorder is highest for film annealed at 673K. At room temperature  $\Delta M$  is highest for film annealed at 873K

Thus we observe that zinc ferrite thin film exhibits ferrimagnetic ordering at room temperature and at 10K. The FC-ZFC data indicate the presence of blocking behavior and disorder effects. These disorders could be leading to superparamagnetism or spin glass behaviour. At room temperature and at 10K, the films are not found to be superparamagnetic because of the non zero values of coercivity and remanence. The large discrepancy between FC and ZFC and the shift in  $T_B$  with increase in cooling field indicates spin glass behavior in zinc ferrite thin films. The ferrimagnetic ordering decreases on annealing at 873K, due to partial reversal to normal spinel structure.

#### **5.4 CONCLUSION**

Zinc ferrite thin films of thickness 120 nm were prepared by RF sputtering. The structural characterization using GXRD and SAED revealed that the films are crystalline. From TEM it was observed that grain size increases on annealing at 873K. The magnetization studies show that the films exhibit hysteresis at room temperature and saturates at low fields. An highest magnetization of 18emu/cc was obtained for the pristine film. The magnetic saturation and high magnetization indicates the ferrimagnetic property of films at room temperature. The observed change in magnetic properties is attributed to

redistribution of cations in A and B site. On annealing the magnetic properties deteriorated due to the tendency of ions to revert back to a normal spinel configuration. FC-ZFC measurements indicate spin glass behavior in zinc ferrite thin films at low temperature.

**REFERENCES:**

- [1] F. G. Brockman, Phys. Rev. **77** (1950) 841.
- [2] Kamazawa K, Tsunoda Y, Kadowaki H and Kohn K, Phys. Rev. B **68** (2003) 024412-1.
- [3] Tanaka K, Nakashima S and Fujita K, J. Phys.: Condens. Matter, **15** (2003) L469.
- [4] Shenoy S D, Joy P A and Anantharaman M R, J. Magn. Magn. Mater. **269** (2004) 217.
- [5] Anantharaman M R, Jagatheesan S, Malini K A., Sindhu S, Narayanasamy A., Chinnasamy C N, Jacobs J P, Reijne S, Seshan K, Smits R H H and Brongersma H H, J. Magn. Magn. Mater. **189** (1998) 83.
- [6] Anantharaman M R, Reijne S, Jacobs J P and Brongersma H H, J. Mater. Sci. **4** (1999) 4279.
- [7] Yamamoto Y, Tanaka H and Tawai K, Jpn. J. Appl. Phys. Part 2 **40** (2001) L545.
- [8] Hofmann M, Campbell S J, Ehrhardt H and Feyerherm R, J. Mater. Sci. **39** (2004) 5057.
- [9] Nakashima S, Fujita K, Tanaka K and Hirao K, J. Phys. Condens. Matter **17** (2005) 137.
- [10] Nakashima S, Fujita K, Tanaka K, Hirao K, Yamamoto T and Tanaka I, J. Magn. Magn. Mater. **310** (2007) 2543.

- [11] Murtaza Bohra , Shiva Prasad , N. Venkataramani , S. C. Sahoo , Naresh Kumar , R. Krishnan, IEEE Trans. Magn. **49** (2013) 4249.
- [12] Li G, Zhu X, Song W, Yang Z, Dai J, Sun Y and Fu Y, J. Am. Ceram. Soc. **94** (2011) 2872.
- [13] Raghavender A. T., Mater. Lett. **65** (2011) 3636.
- [14] Sultan M and Singh R, J. Phys. D. Appl. Phys. **42** (2009) 115306-1.
- [15] A. Pradeep, P. Priyadharsini, G. Chandrasekaran, J. Alloys and Comp. **509** (2011) 3917.
- [16] M. Atif, S.K. Hasanain, M. Nadeem, Solid State Commun. **138** (2006) 416.
- [17] Bohra M, Prasad S, Kumar N, Misra D S and Sahoo S C, Appl. Phys. Lett. **88** (2006) 262506-1.
- [18] Liang Y and Hsia H, Nanoscale Research Letters **1** (2013) 1.
- [19] Doolittle R, Nucl. Inst. and Methods in Phys. Res. **B9** (1985) 344.
- [20] M. Desai, J. Dash, I. Samajdar, N. Venkataramani, Shiva Prasad, P Kishan, Nitendar Kumar, J. Magn. Magn. Mater. **231** (2001) 108.
- [21] Guo D, Zhu J, Yang Y, Fan X, Chai G, Sui W, Zhang Z and Xue D, J. Appl. Phys. **107** (2010) 043903-1.
- [22] Nakashima S, Fujita K, Tanaka K, Hirao K, Yamamoto T and Tanaka I, Phys. Rev. B **75** (2007) 174443-1.
- [23] Bhowmik R, Ranganathan R and Nagarajan R, Phys. Rev. B **73** (2006) 144413-1.

*Chapter 5*

## **Chapter 6**

### **Evolution of structural, topographical and magnetic properties of zinc ferrite thin films by Swift Heavy Ion irradiation**

#### 6.1 Introduction

#### 6.2 Experimental Methods

#### 6.3 Results and Discussion

- Simulation studies: Stopping Range of Ions in Matter (SRIM)
- Thickness measurement: Cross section Transmission Electron Microscope (TEM)
- Structural characterization: Glancing Angle X ray Diffractometer (GXRD)
- Topographical studies: Atomic Force Microscope (AFM)
- Magnetic studies: Super conducting Quantum Interferometer Device (SQUID)-Vibrating Sample Magnetometry (VSM)

#### 6.4 Conclusion

#### References

*Chapter 6*

## **6.1 INTRODUCTION**

Ion irradiation is a versatile tool for material modification and nanostructuring. Swift heavy ion irradiation induces amorphisation, recrystallisation and nanostructuring in materials [1-2]. The formation of ion tracks by swift heavy ions is increasingly sought after by researchers for ion induced modification and depends on both the material properties and the energy of the incoming ion [3]. The track formation occurs beyond a particular threshold of electronic energy loss and size of the tracks can be controlled by a judicious choice of ion energy and fluence [3-4]. The formation of ion tracks can greatly influence the magnetic properties as the stress generated by tracks can affect the anisotropy and permeability [5-7]. Ferrites are an important class of materials having spinel, inverse spinel or mixed spinel structure. Ion induced modifications of ferrites have been studied extensively by researchers [3, 6, 8-11]. The magnetic properties are structure sensitive and the degree of structure disorder determines the magnetic order in the system. The magnetic properties are determined by magnetic interaction among A and B site. The interaction of ions in A and B site result in  $J_{AB}$  interaction leading to ferrimagnetic ordering, while,  $J_{AA}$  and  $J_{BB}$  lead to antiferromagnetic ordering. The threshold electronic energy loss for track formation in ferrites is 20 keV/nm [12]. Many studies have been carried out on the ion induced modification in inverse and doped ferrites which are already ferrimagnetic in nature [6, 8, 11]. Swift heavy ion irradiation in Nickel zinc ferrite and magnesium ferrites, are reported to be modifying structural and magnetic properties [8, 11].

Zinc ferrite is a normal spinel and exhibits antiferromagnetic properties in the bulk [13]. However, thin film and nano forms of zinc ferrite exhibits altogether different properties and this has been attributed to cation redistribution

[14-19]. Shenoy *et al.* have observed room temperature superparamagnetic behavior in ball milled zinc ferrite [14]. Hoffmann *et al.* observed glassy behavior in nano zinc ferrite and the blocking temperature was found to be influenced by the particle size [20]. Jeong *et al.* reported nanocrystalline zinc ferrite to exhibit ferrimagnetism up to 460K and co existent ferrimagnetic and antiferromagnetic ordering at 10K. The competition between Fe ions to interact via  $J_{AB}$  and  $J_{BB}$  results in canted spin structure of Fe ions in B site [21]. Nakashima *et al.* have reported high magnetization in zinc ferrite thin films prepared by RF sputtering [15]. Bohra *et al.* have studied the properties of zinc ferrite thin films prepared by RF sputtering and Pulsed Laser Deposition [19]. Recently Liang *et al.* have observed a magnetization of 1 milli emu/cc in zinc ferrite thin films [22]. In the previous chapter, we have reported a magnetisation of 18 emu/cc in zinc ferrite thin films of thickness 120 nm prepared by RF sputtering [23]. The altogether different properties of zinc ferrite which depends mainly on cation redistribution make zinc ferrite an interesting candidate for further investigations. The effect of amorphisation induced as a result of SHI in zinc ferrite thin films have not been thoroughly studied yet and this is one of the objectives of this investigation. The structural and morphological changes induced as a result of ion irradiation is also looked at.

## 6.2 EXPERIMENTAL METHODS

Zinc ferrite thin films were prepared by RF sputtering from a phase pure target synthesized by sol gel auto combustion method. The films were deposited on naturally oxidized silicon substrates at an RF power of 150 watts for 90 minutes. The films were annealed at 873K and then irradiated using 100MeV Ag ions at fluences of  $1 \times 10^{12}$ ,  $1 \times 10^{13}$ ,  $3 \times 10^{13}$  ions/cm<sup>2</sup>. The range and energy loss of 100 MeV AG ions in zinc ferrite films were simulated using the SRIM code [24].

The structural characterization was done using Glancing Angle X-Ray Diffractometer (GXRD) Bruker Discover D-8 with Cu K $\alpha$  ( $\lambda=1.5406\text{\AA}$ ) at a glancing angle of  $1^\circ$ . The crystallite size  $D$  is calculated using Scherrer formula. Atomic Force Microscope (AFM) Nanoscope IIIa Digital Instruments, Veeco was employed to study the morphology of sample on ion irradiation. Roughness and Power Spectral Density (PSD) were deduced from AFM images. Magnetic hysteresis at room temperature and at 5K, and FC-ZFC measurements from 300K to 5K at a cooling field of 500e and 1000e were carried out using SQUID VSM.

### 6.3 RESULTS AND DISCUSSIONS

The electronic energy loss of 100 MeV Ag ions in zinc ferrite as calculated using SRIM software was 0.015 MeV/nm. The range of ions was 11  $\mu\text{m}$  which is much greater than the film thickness. The film thickness was calculated from cross sectional TEM (figure 2) and was 320 nm.

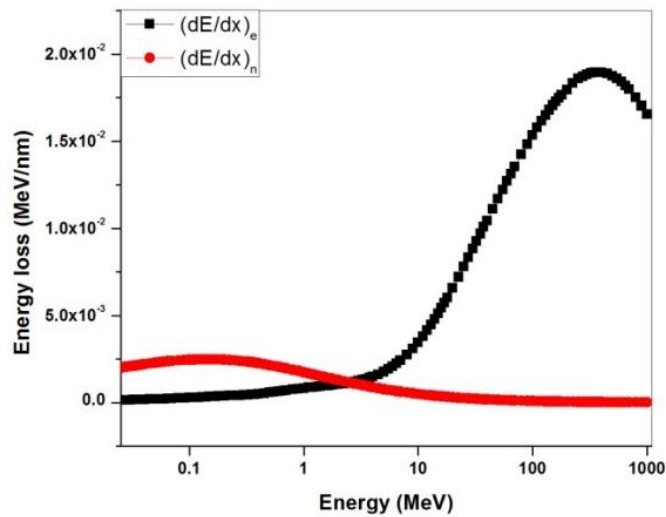


Fig. 1 SRIM simulation of electronic and nuclear energy loss of 100 MeV Ag ions in zinc ferrite

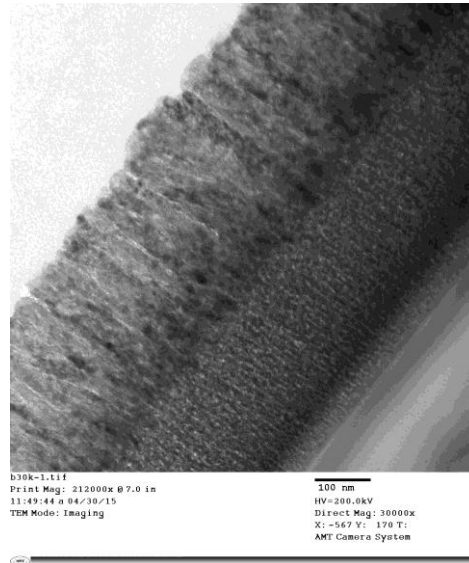


Fig. 2 Cross sectional TEM image of pristine zinc ferrite film

The GXRD pattern of pristine and irradiated films is shown in figure 3. Each sample was subjected to GXRD before and after irradiation to avoid sample to sample variation. The crystallite size calculated using Scherrer formula was found to be 21 nm for pristine film. The crystallite size was observed to vary with ion fluence. At a fluence of  $1 \times 10^{12}$  ions/cm<sup>2</sup>, crystallite size reduced to 15 nm and at the highest fluence of  $3 \times 10^{13}$  ions/cm<sup>2</sup> crystallite size further increased to 17nm. The decrease in crystallite size with ion fluence is due to amorphisation of the material and has been observed in many other systems [8, 25]. The amorphisation of the crystalline material can be explained in accordance with the thermal spike model, where in, the high energy imparted by ions creates localized high temperature zones ( $10^5$  K) along the ion path, which can melt the material which is followed by sudden cooling ( $\sim 10^{-13}$  ps) resulting in amorphisation along the ion path [26-27]. This high energy imparted can cause breakage of crystallites. The observed increase in crystallite size at higher fluence can be attributed to

agglomeration of the broken crystallites [6, 28]. The crystallite can flow along the melted track and rejoin to form slightly bigger crystallites.

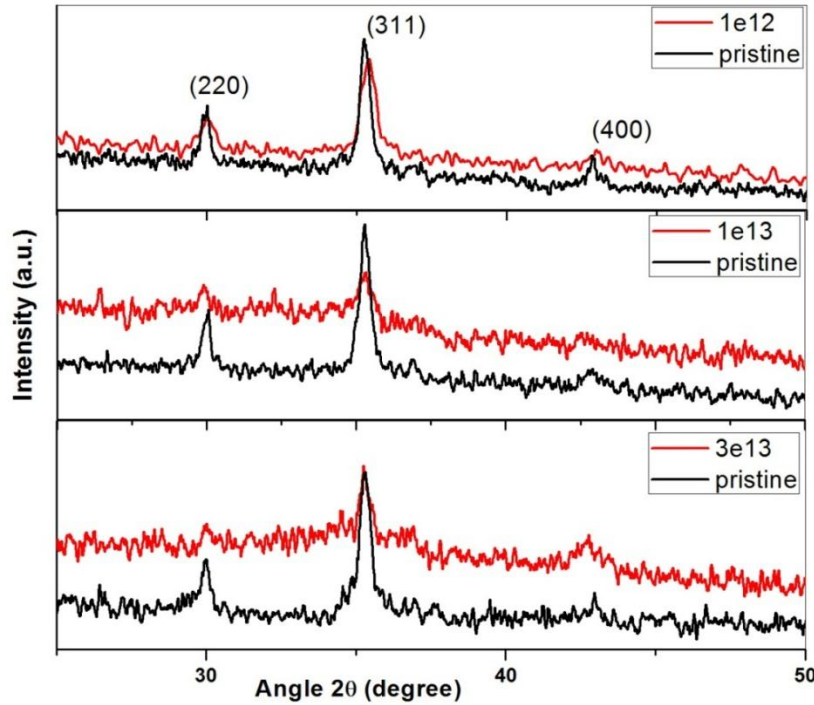


Fig. 3 GXR D pattern of pristine and irradiated films

The 2D and 3D AFM images are shown in figure 4 and 5. The grain size was observed to decrease at lower fluence and increase at the highest fluence consistent with the GXR D studies. For the samples irradiated at a fluence of  $3 \times 10^{13}$  ions/cm<sup>2</sup> one can observe agglomeration of grains which are responsible for the increase in grain size.

From AFM analysis we can obtain information regarding rms roughness  $R_q$ , maximum roughness  $R_{max}$ , average roughness  $R_a$ , skewness and kurtosis.  $R_a$  is the arithmetic average of the absolute values of the surface height deviations measured from the mean plane.  $R_{max}$  is the maximum vertical distance between

## Chapter 6

the highest and lowest data points in the image following the plane fit.  $R_q$  is the root mean square average of height deviations taken from the mean image data plane. Skewness is indicative of symmetry in distribution of surface features. For a symmetric distribution of surface features having a Gaussian distribution, the skewness value is 0. A surface with flat peaks and deep valleys has a negative skewness while a surface with wide distribution of peaks has a positive skewness. The sharpness of surface features is given by the kurtosis value. The kurtosis value tends to 3 for a Gaussian surface; whereas a higher value of kurtosis indicates the presence of sharper surface features in the films. When the surface features are more or less flatly distributed, the kurtosis value will be less than 3 [29].

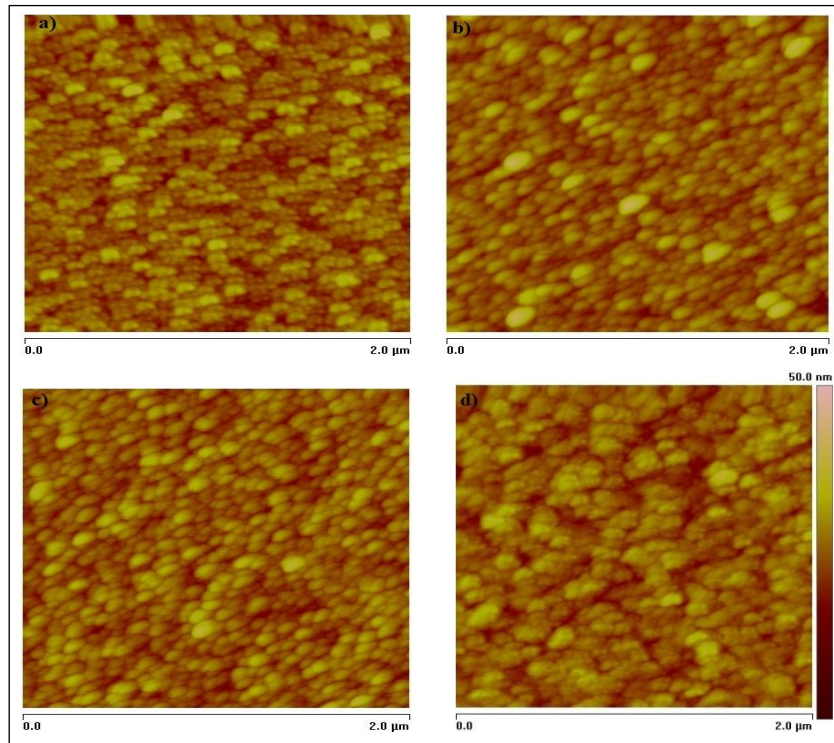


Fig. 4 AFM images of a) pristine and film irradiated at fluences b)  $1 \times 10^{12}$  c)  $1 \times 10^{13}$  and d)  $3 \times 10^{13}$  ions/cm<sup>2</sup>

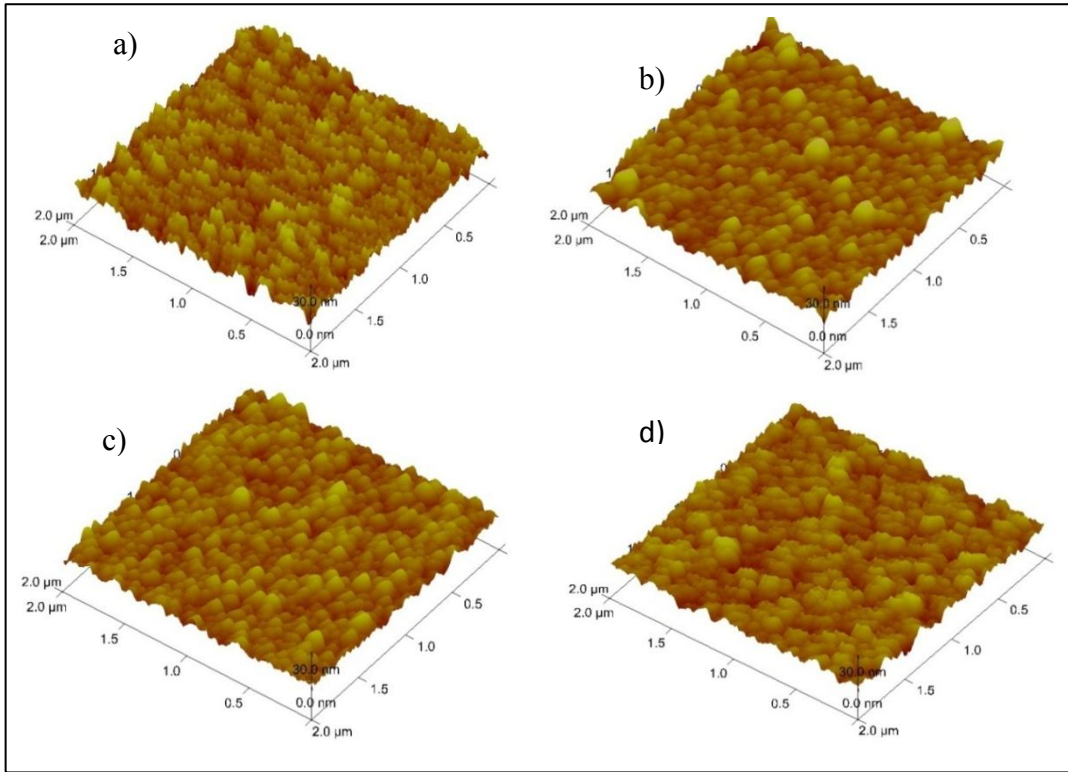


Fig. 5. 3D AFM images of a) pristine and film irradiated at fluences b)  $1 \times 10^{12}$  c)  $1 \times 10^{13}$  and d)  $3 \times 10^{13}$  ions/cm<sup>2</sup>

Sample	$R_q$	$R_a$	$R_{max}$	Skewness	Kurtosis
Pristine	$3.61 \pm 0.02$	$2.88 \pm 0.01$	$27.6 \pm 2.7$	$0.220 \pm 0.01$	$3.01 \pm 0.06$
$1 \times 10^{12}$	$3.37 \pm 0.01$	$2.58 \pm 0.01$	$28.5 \pm 2.6$	$0.834 \pm 0.01$	$4.77 \pm 0.02$
$1 \times 10^{13}$	$3.31 \pm 0.01$	$2.64 \pm 0.01$	$25.9 \pm 2.7$	$0.286 \pm 0.01$	$3.11 \pm 0.05$
$3 \times 10^{13}$	$3.46 \pm 0.04$	$2.76 \pm 0.03$	$27.4 \pm 3.7$	$-0.0197 \pm 0.01$	$2.97 \pm 0.01$

Table 1: Roughness values of pristine and irradiated films

The rms roughness  $R_q$ , maximum roughness  $R_{max}$ , average roughness  $R_a$ , skewness and kurtosis are tabulated in table 1.  $R_q$  and  $R_{max}$  decreases at lower fluences and thereafter increases. At the highest fluence the grains are

## Chapter 6

agglomerated and cause an increase in surface roughness. The high energy imparted to the material initially breaks the grain and at higher fluence they diffuse through the surface and the grains are agglomerated. The formation of hills and valleys are also predominant at a fluence of  $3 \times 10^{13}$  ions/cm<sup>2</sup>. This may be because of surface diffusion as a result of irradiation. The skewness value increases at lower fluence and decrease for the higher fluence. The film irradiated at  $3 \times 10^{13}$  ions/cm<sup>2</sup> shows a skewness value slightly less than 0 and kurtosis value less than 3. The negative skewness indicates presence of hills and valleys on the film surface. A kurtosis value of 3 is obtained for the pristine and films irradiated at  $1 \times 10^{13}$  ions/cm<sup>2</sup> and show a skewness value 0.2 which is indicative of symmetry in surface distribution.  $1 \times 10^{12}$  ions/cm<sup>2</sup> irradiated sample has a skewness of 0.8 and kurtosis of 4. This denotes sharpness in the distribution of surface features.

To understand the mechanism of surface evolution due to ion irradiation, the AFM images were subjected to power spectral density analysis. PSD spectra of pristine and irradiated films are shown in figure 6. The low frequency region represents noise and the high frequency region obeys a power law and the slope  $\xi$  values indicate various surface evolution mechanisms.  $\xi$  values of 1, 2, 3 and 4 represents surface evolution due to plastic flow driven by surface tension, evaporation-condensation, volume diffusion and surface diffusion [30-33]. For the pristine film, the slope value is 2.4 and on increasing the fluence the slope decrease. The possible surface mechanism is evaporation-condensation and the decrease in slope with fluence indicates change of surface mechanism to plastic flow as a result of irradiation.

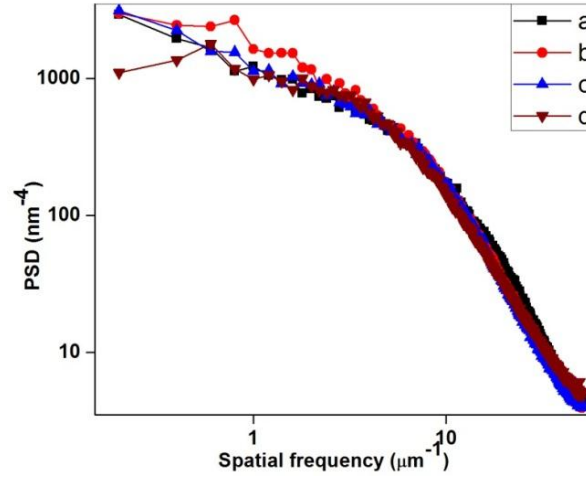


Fig. 6 PSD spectra of a) pristine and film irradiated at fluences b)  $1 \times 10^{12}$  c)  $1 \times 10^{13}$  and d)  $3 \times 10^{13}$  ions/cm<sup>2</sup>

Hysteresis loops were traced at room temperature and at 5K for pristine and irradiated films (figure 7). The pristine films show a near saturation with a magnetisation of 40 emu/cc indicating ferrimagnetic behaviour of films. The  $1 \times 10^{12}$  ions/cm<sup>2</sup> irradiated samples show almost similar behaviour that of pristine sample. On irradiating the sample at a fluence of  $1 \times 10^{13}$  ions/cm<sup>2</sup> magnetization was lowered and at fluence of  $3 \times 10^{13}$  ions/cm<sup>2</sup> magnetization increased to 22 emu/cc. The variation of  $M_s$  and  $H_c$  with fluence is shown in figure 8 . MH loops at 5K is shown in figure 7b . Contrary to room temperature ferrimagnetic behaviour, the loops of pristine film and films irradiated at  $1 \times 10^{12}$  ions/cm<sup>2</sup> were not saturating even at the maximum applied field of 60000 Oe. However films irradiated at  $1 \times 10^{13}$  ions/cm<sup>2</sup> and  $3 \times 10^{13}$  ions/cm<sup>2</sup> saturated at a field of 15000 Oe. The variation of magnetization with fluence at 5K was similar to that of room temperature magnetization and the pristine sample exhibited higher saturation magnetization.

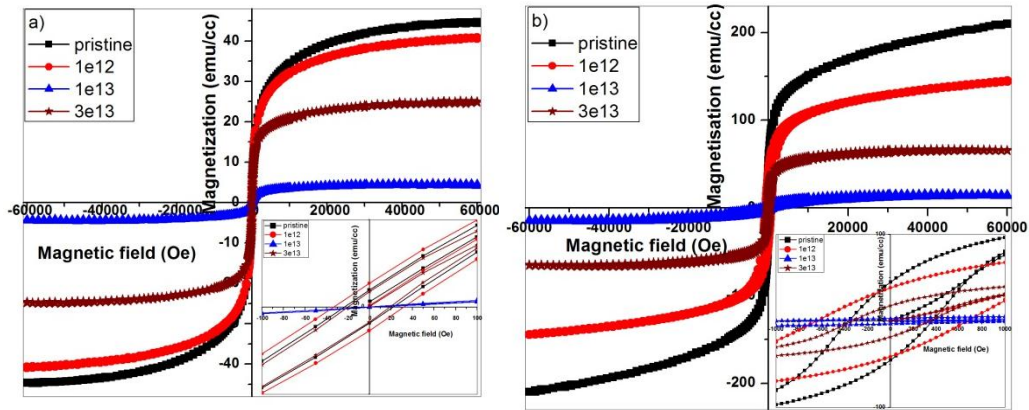


Fig. 7 MH loops of pristine and irradiated films a) at room temperature and b) at 5K

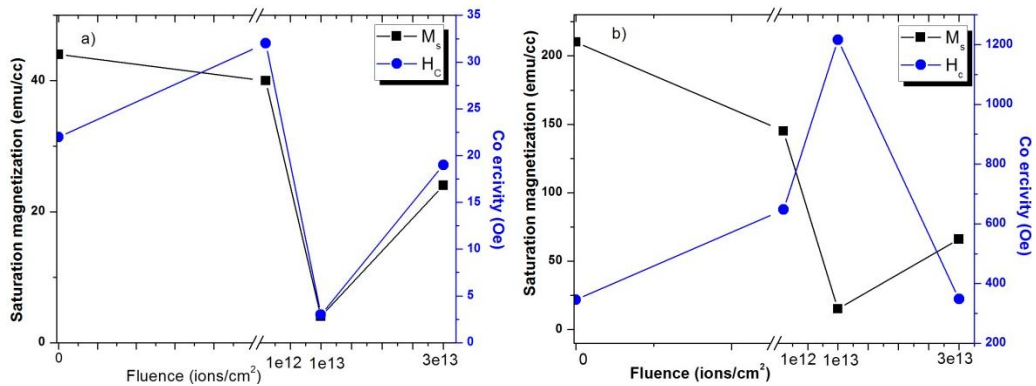


Fig. 8 Variation of  $M_s$  and  $H_c$  with fluence a) at room temperature and b) at 5K

Nakshima *et al.* have observed room temperature ferrimagnetism in zinc ferrite thin films [15] while Bohra *et al.* have observed that the films were paramagnetic at room temperature [19]. Our earlier studies on zinc ferrite thin films prepared by RF sputtering exhibited ferrimagnetism at room temperature [23]. The magnetism of zinc ferrite thin films is greatly influenced by the cation distribution in the octahedral and tetrahedral sites. The ferrimagnetic behaviour of

zinc ferrite thin films is due to redistribution of  $\text{Fe}^{3+}$  ions into A site which leads to strong A-O-B interaction. The decrease in magnetization with ion fluence can be attributed to ion induced defects in the system which alters the cation distribution. GXR and AFM results indicate that the crystallite size decrease at initial fluence and increase at highest fluence. The decrease in crystallite size leads to surface state pinning of domains which results in decrease in magnetization. At the fluence of  $3 \times 10^{13}$  ions/cm<sup>2</sup>, crystallite size increases and surface state pinning of domains is released which can enhance the magnetization [6, 34]. The lack of saturation at 5K can be attributed to the antiferromagnetic ordering of the films below the Neel temperature.

FC-ZFC curves of pristine and irradiated samples for cooling fields of 50Oe and 100Oe are shown in figure 9.  $T_{\text{irr}}$  the bifurcation point of FC and ZFC shifts to lower temperatures on increasing the cooling field. For the sample irradiated at  $1 \times 10^{12}$ , the ZFC maxima also shifts to lower temperature on increasing cooling field indicative of a glassy behaviour. For pristine and  $3 \times 10^{13}$  irradiated sample, the ZFC maxima exhibits a very broad peak. Tung *et al.* reported that ZFC peaks becomes broader with increase in particle size in zinc ferrite nanoparticles due to the presence of wide distribution of relaxation times for metastable magnetic state [35]. In the present case, the pristine sample have highest grain size and on irradiation at  $1 \times 10^{12}$ , the grain size reduces and at higher fluence of  $3 \times 10^{13}$ , the grain size increases. The broadness of ZFC curve can be attributed to variation in grain size.

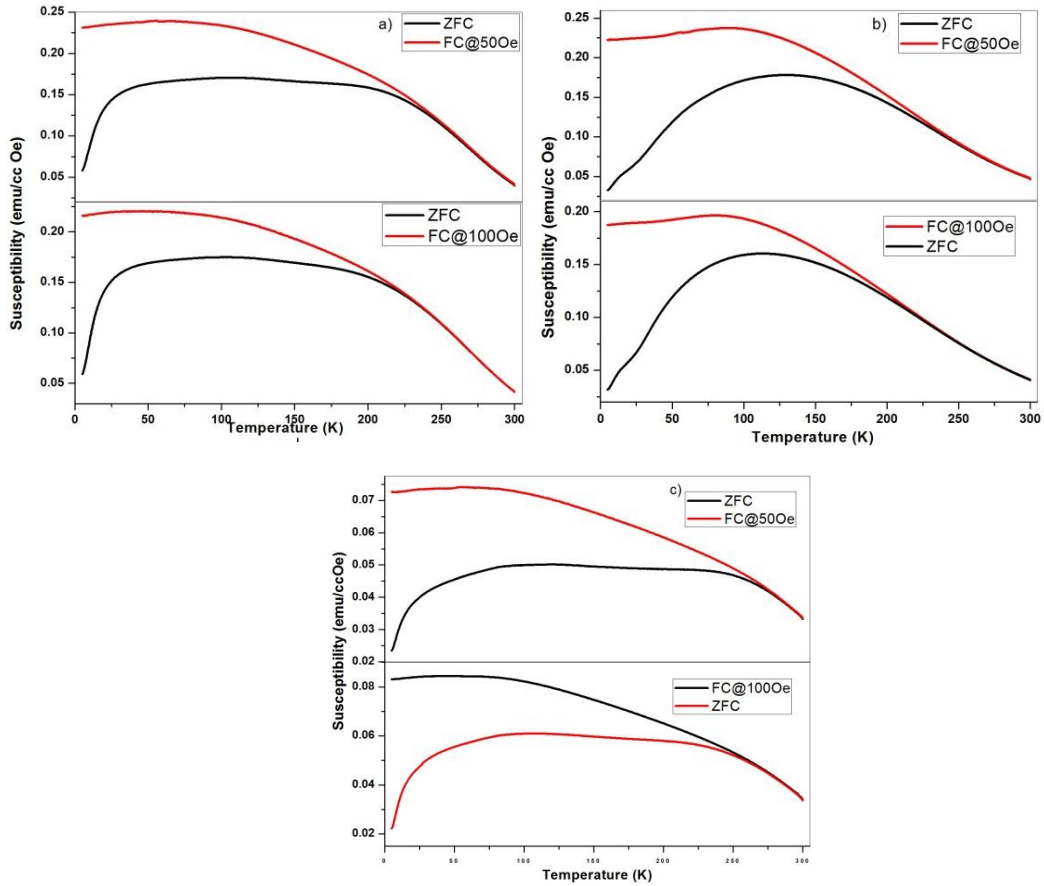


Fig. 9 FC-ZFC of zinc ferrite films a) pristine b) irradiated at fluence of  $1 \times 10^{12}$  and c)  $3 \times 10^{13}$  ions/cm<sup>2</sup> at cooling fields of 50Oe and 100Oe

#### 6.4 CONCLUSION

Zinc ferrite films of thickness 320 nm were prepared by RF sputtering; the films were annealed at 873K and then irradiated with 100 MeV Ag ions at fluences of  $1 \times 10^{12}$ ,  $1 \times 10^{13}$  and  $3 \times 10^{13}$  ions/cm<sup>2</sup>. Amorphisation of films were observed with irradiation, and for the highest fluence of  $3 \times 10^{13}$  ions/cm<sup>2</sup>, there was an increase in crystallite size. AFM images also indicate an initial reduction and an increase of grain size with ion fluence. Power spectral density analysis

indicates the possible mechanism of surface evolution as evaporation-condensation for the pristine film and on irradiation at higher fluences the mechanism changes to plastic flow. The saturation magnetization was observed to decrease with ion fluence which is due to surface state pinning of domains as a result of reduced particle size. FC-ZFC studies indicate spin glass behavior in pristine and irradiated films, and the ZFC curve was influenced by the grain size. Thus the structural, topographical and magnetic properties of zinc ferrite thin films were tailored by swift heavy ions.

## **REFERENCES**

1. Jain I P and Agarwal G, Surf. Sci. Rep. **66** (2011) 77
2. D K Avasthi, G K Mehta, Swift heavy ions for materials engineering and nanostructuring, Springer series 2011
3. Zinkle S J, Nucl. Instrum. Methods Phys. Res. Sect. B Beam Interact. with Mater. Atoms **141** (2008) 737
4. Colder a., Marty O, Canut B, Levalois M, Marie P, Portier X, Ramos S M M and Toulemonde M, Nucl. Instrum. Methods Phys. Res. Sect. B Beam Interact. with Mater. Atoms **174** (2001) 491
5. Costantini J-M, Studer F and Peuzin J-C, J. Appl. Phys. **90** (2001) 126
6. Sharma S K, Kumar R, Siva Kumar V V, Knobel M, Reddy V R, Gupta A. and Singh M, Nucl. Instrum. Methods Phys. Res. Sect. B Beam Interact. with Mater. Atoms, **248** (2006) 37
7. J P Nozieres, M. Ghidini, N.M. Dempsey, B. Gervais, D. Givord, G. Suran, J.M.D. Coey, Nucl. Instrum. Methods Phys. Res. Sect. B Beam Interact. with Mater. Atoms, **146** (1998) 250

## Chapter 6

8. Dixit G, Singh J P, Srivastava R C and Agrawal H M, Nucl. Instrum. Methods Phys. Res. Sect. B Beam Interact. with Mater. Atoms, **269** (2011) 133
9. Srivastava R C, Singh J P, Agrawal H M, Kumar R, Tripathi a, Tripathi R P, Reddy V R and Gupta A, J. Phys. Conf. Ser. **217** (2010) 012109
10. Shinde S R, Bhagwat A, Patil S I, Ogale S B, Mehta G K, Date S K and Mareest G, J. Magn. Magn. Mater. **186** (1998) 342–348
11. Rao B P, Rao K H, Subba Rao P S V, Mahesh Kumar a., Murthy Y L N, Asokan K, Siva Kumar V V, Kumar R, Gajbhiye N S and Caltun O F, Nucl. Instrum. Methods Phys. Res. Sect. B Beam Interact. with Mater. Atoms, **244** (2006) 27
12. Studer F, Houpert C, Groult D, Meftah A, Toulemonde M and Cedex C, Nucl. Instrum. Methods Phys. Res. Sect. B Beam Interact. with Mater. Atoms **82** (1993) 91
13. F. G Brockman, Phys. Rev. **77** (1950) 841
14. Shenoy S D, Joy P A. and Anantharaman M R, J. Magn. Magn. Mater. **269** (2004) 217
15. Nakashima S, Fujita K, Tanaka K and Hirao K, J. Phys. Condens. Matter **17** (2005) 137
16. Tanaka K, Nakashima S, Fujita K and Hirao K, J. Appl. Phys. **99** (2006) 106103
17. Nakashima S, Fujita K, Tanaka K, Hirao K, Yamamoto T and Tanaka I, J. Magn. Magn. Mater. **310** (2007) 2543
18. Guo D, Zhu J, Yang Y, Fan X, Chai G, Sui W, Zhang Z and Xue D, J. Appl. Phys. **107** (2010) 043903

19. Bohra M, Prasad S, Kumar N, Misra D S, Sahoo S C, Venkataramani N and Krishnan R, *Appl. Phys. Lett.* **88** (2006) 262506
20. Hofmann M, Campbell S J, Ehrhardt H and Feyerherm R, *J. Mater. Sci.* **39** (2004) 5057
21. Shim J, Lee S, Park J, Han S-J, Jeong Y and Cho Y, *Phys. Rev. B* **73** (2006) 064404
22. Liang Y and Hsia H, *Nanoscale Research Letters* **1** (2013) 1
23. Raghavan L, Pookat G, Thomas H, Ojha S, Avasthi D K and Anantharaman M R, *J. Magn. Magn. Mater.* **385** (2015) 265
24. Ziegler J F, Biersack, J P, Littmark U, *The Stopping and Range of Ions in Solids* (New York: Pergamon) SRIM code: <http://www.srim.org> (1985)
25. Shukla D K, Kumar R, Mollah S, Choudhary R J, Thakur P, Sharma S K, Brookes N B and Knobel M, *Phys. Rev. B* **82** (2010) 174432
26. Szenes G, Horváth Z, Pécz B, Pászti F and Tóth L, *Phys. Rev. B* **65** (2002) 045206
27. Dufour C, Paumier E and Toulemonde M, *Nucl. Instrum. Methods Phys. Res. Sect. B Beam Interact. with Mater. Atoms* **122** (1997) 68
28. Pal J, Dixit G, Kumar H, Srivastava R C, Agrawal H M and Kumar R, *J. Magn. Magn. Mater.* **352** (2014) 36
29. Yildirim G, Bal S, Gulen M, Varilci , Budak E and Akdogan M, *Cryst. Res. Technol.* **47** (2012) 195
30. Gavrilă R, Dinescu A and Mardare D, *Rom. J. Inf. Sci. Technol.* **10** (2007) 291
31. Dash P, Mallick P, Rath H, Tripathi A, Prakash J, Avasthi D K, Mazumder S, Varma S, Satyam P V and Mishra N C, *Appl. Surf. Sci.* **256** (2009) 558

*Chapter 6*

32. Herring C, J. Appl. Phys. **21** (1950) 301
33. Mullins W W, J. Appl. Phys. **30** (1959) 77
34. Kumar R, Sharma S K, Dogra A, Siva Kumar V V., Dolia S N, Gupta A, Knobel M and Singh M , Hyperfine Interact. **160** (2005) 143
35. L.D. Tung, V. Kolesnichenko, G. Caruntu, D. Caruntu, Y. Remond, V.O. Golub, C.J. O'Connor, L. Spinu, Physica B **319** (2002) 116

## Chapter 7

### Exchange bias in FeNiMoB-Zinc Ferrite bilayer films

#### 7.1 Introduction

#### 7.2 Experimental Methods

#### 7.3 Results and Discussions

##### 7.3.1 Dependence of thickness and annealing on exchange bias

- Thickness and Compositional analysis: Rutherford Backscattering Spectrometry (RBS)
- Magnetic studies: Super conducting Quantum Interferometer Device -Vibrating Sample magnetometer (SQUID VSM)

##### 7.3.2 Dependence of SHI irradiation on exchange bias

- Simulation studies: Stopping Range of Ions in Matter (SRIM)
- Structural Analysis: Glancing angle X-ray Diffractometer (GXRD)
- Magnetic studies: Super conducting Quantum Interferometer Device -Vibrating Sample magnetometer (SQUID VSM)

#### 7.4 Conclusions

#### References

*Lisha et al. AIP Conference Proceedings 1665 (2015) 130045*

*Lisha et al. (accepted for publication in Nuclear Instruments and Methods in Physics Research B)*

*Chapter 7*

## **7.1 INTRODUCTION**

The studies on single layer films of FeNiMoB and zinc ferrite and the modification of their properties by thermal annealing and ion irradiation was discussed in the previous chapters. The formation of bilayer system always gives rise to new properties and is highly influenced by the interface. Studies on bilayer of FeNiMoB and zinc ferrite are discussed in the present chapter. Exchange bias effect is an interface phenomenon and was observed earlier at ferromagnet (FM) and antiferromagnet (AFM) interface. Exchange bias effect is the phenomenon wherein the spins of ferromagnet (FM) and antiferromagnet (AFM) interact at the FM-AFM interface, and thereby forces the AFM spins to align parallel with FM spins at the interface on field cooling. The alignment of AFM spins exerts a torque which the FM spins has to overcome on reversal of applied magnetic field resulting in an apparent shift of hysteresis loop along the field axes when field cooled below the Neel temperature of AFM [1]. Along with hysteresis loop shift one may also observe vertical shift and enhancement of the hysteresis loop. Exchange bias effect is observed in FM-AFM layers, FM-AFM core shell systems and also in systems having ferromagnetic domain, spin glass (SG) or disordered surface spins [2]. In FM-SG systems the spin glass is modeled as a diluted AFM with long range interactions [3]. The exchange biased structures find application as spin valves, magnetic tunnel junctions and spintronic devices [1]. Applications involving exchange bias necessitate tailoring bias and coercive fields by appropriate techniques [4].

Many models have been proposed to explain the exchange bias effect [5, 6, 7]. Some models consider exchange bias solely as an interface phenomenon, [8] while some others assume exchange bias to be dependent on the whole of AFM [5, 6]. Many researchers have observed that the bias and coercive fields are

## Chapter 7

greatly influenced by both the FM and AFM thickness [9-12]. The most well studied exchange bias system is FeNi-FeMn. In this system it was reported that the bias field obeys a power law with AFM thickness as  $1/t^\lambda$ , where the exponent  $\lambda$  ranges from 0 to 0.3 [12]. The inverse relation of exchange bias with AFM thickness was also observed in various other systems namely IrMn<sub>3</sub>/Co, La<sub>2/3</sub>Ca<sub>1/3</sub>MnO<sub>3</sub>/La<sub>1/3</sub>Ca<sub>2/3</sub>MnO<sub>3</sub>, Ta/Py/IrMn/Pt [10, 11, 13]. In most of the studies carried out so far, the optimum thickness of the AFM layer is ~20 nm, the bias field disappears for thickness values greater than this optimum thickness [13-16]. In some other systems like CuMn-Co, it was observed that bias field increases with thickness and attains saturation [3, 17]. The effect of thickness on the exchange bias is not universal and found to vary from system to system. Thus the dependence of thickness on the exchange bias field is of great significance.

The exchange bias can be tailored by diluting the AFM with suitable non magnetic impurities or by creating defects by ion irradiation or other techniques [15, 18]. Ion irradiation offers unique possibilities in modifying exchange bias [1]. The changes in exchange bias with ion fluence have been modeled based on a competition between defect creation and interfacial mixing [19]. Most of the ion induced modification studies on exchange bias systems are found in the low energy regime [14, 15, 20, 21]. It must be noted here that low energy ions are suitable for modification of materials when the film thickness is small (~1-10nm). For larger film thickness (~ 100-1000 nm) the less energetic ions get embedded in the film; while, high energy ions can create amorphous tracks in films of much larger thickness. Contrary to low energy ions, where high fluences ( $\sim 10^{16}$ ) are required, high energy ions can produce the same effects at much lower fluences, three to four orders smaller than that of low energy ions. Mougín *et al.* studied the effect of 10keV He ions on 5nm-10 nm FeNi-FeMn thin films [15]. They observed

an enhancement of exchange bias at lower fluences and a decrease at higher fluence. Effect of high energy ions on the exchange bias properties would be an interesting research area since it offers an ideal template to investigate the effect of electronic energy loss on exchange bias properties. As mentioned earlier, the dominant mechanism of material modification at low energies is via nuclear energy loss, while in the case of high energy ions it is through electronic energy loss and hence effect of high energy ions on exchange bias properties is also interesting from a fundamental perspective.

The system under investigation is zinc ferrite- metallic glass. Zinc ferrite is an antiferromagnet with a Neel temperature of 10K, while metallic glass, an alloy of Fe, Ni, Mo, B is an excellent soft ferromagnetic material with a Curie temperature of 600K. Zinc ferrite in the nano regime is purported to be exhibiting anomalous magnetic behavior namely, ferrimagnetic, superparamagnetic, antiferromagnetic or even glassy behavior depending on cation distribution in the A and B sites of the spinel structure [22-27]. Hysen *et al.* and Senoy *et al.* reported soft magnetic properties in thin films of Fe-Ni alloys and the properties could be tailored by thermal annealing and swift heavy ion irradiation [28- 30]. Substantial amount of work has been carried out in the past on these materials namely, zinc ferrite and Fe-Ni alloys in our laboratory, [26-30] and it was thought fit to look at the possibilities of inducing exchange bias on a bilayer consisting of zinc ferrite and FeNiMoB alloys fabricated using RF sputtering. The effect of swift heavy ion irradiation, layer thicknesses and thermal annealing on the exchange bias field and coercivity is of interest to the scientific community and are the motives of the present investigation.

The present chapter is divided into two sections; the first part deals with the dependence of film thickness and thermal annealing on exchange bias effect;

## Chapter 7

the role of swift heavy ions in tailoring the exchange bias properties is probed in the second part.

### 7.2 EXPERIMENTAL METHODS



Fig.1. Schematic of the bilayer structure

The bilayer film of FeNiMoB-zinc ferrite was prepared by RF sputtering using targets of Fe<sub>30</sub>Ni<sub>48</sub>Mo<sub>4</sub>B<sub>18</sub> ribbon and zinc ferrite (prepared by sol gel auto combustion technique). The films were deposited on naturally oxidized Si substrate. The schematic is shown in figure 1. FeNiMoB was deposited initially on natively oxidized Si substrate for 30 minutes at an RF power of 100 Watts. Subsequent to that zinc ferrite was deposited at an RF power of 150 watts for 90 minutes. The thickness was controlled by varying the Ar gas flow. For both depositions the pre deposition pressure in the chamber was  $6 \times 10^{-6}$  Torr which reduced to  $5 \times 10^{-2}$  Torr during deposition. The films of higher thickness were annealed at 873K for 1 hour. Rutherford Backscattering Spectrometry (RBS) was carried out to determine the film thickness and composition. The obtained experimental results were simulated using the XRUMP software. The magnetisation measurements at room temperature and at 10 K were carried out employing SQUID VSM. The low temperature magnetic measurements were performed by field cooling at 5000 Oe.

The films of higher thicknesses annealed at 873K were subjected to swift heavy ion irradiation employing 100 MeV  $\text{Ag}^{8+}$  ions at fluences of  $1 \times 10^{11}$ ,  $1 \times 10^{12}$ ,  $1 \times 10^{13}$  and  $3 \times 10^{13}$  ions / $\text{cm}^2$ . The range and energy loss of ions was calculated using Stopping Range of Ions in Matter (SRIM) code [31]. The structural characterization was done using Glancing X-Ray Diffractometer (GXRD). Magnetic measurements were carried out as described earlier.

## **7.3 RESULTS AND DISCUSSION**

### ***7.3.1 Dependence of film thickness and thermal annealing on Exchange Bias***

From RBS (figure 2), zinc ferrite layer was found to be 120 nm thick with a composition of Zn 11.1%, Fe 22.2% and O 66.7% and FeNiMoB was 60 nm thick with a composition of Fe 19.1%, Ni 19.1%, Mo 1.5% and O 58.8%. This set of film is coded as FNMB-ZF1.

The film of higher thickness is coded as FNMB-ZF2. The zinc ferrite layer has a thickness of ~350 nm and a composition corresponding to Zn 12.5 %, Fe 25 %, O 62.5 %. The Fe-Ni-Mo-B layer was ~270 nm thick and has a composition of Fe 17 %, Ni 17 %, Mo 3% and O 63%.

Chapter 7

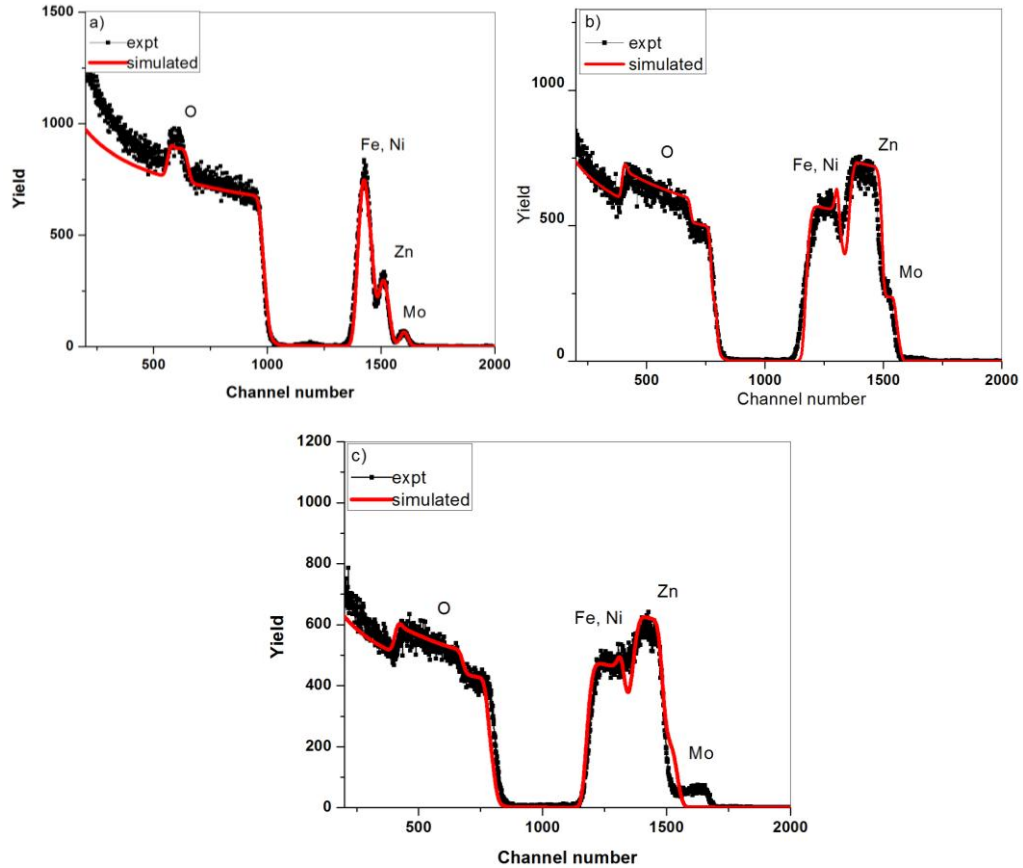


Fig. 2 RBS spectrum of a) FNMB-ZF1 b) FNMB-ZF2 c) FNMB-ZF2 annealed at 873K

Hysteresis curve at room temperature and at 10K with field cooling of films of different thickness and film annealed at 873K is shown in figure 3. It is evident that MH at 10K with field cooling exhibits an enhancement of the hysteresis loop along with field shift. The exchange field  $H_E$  value for FNMB-ZF1 was 75 Oe. FNMB-ZF2 exhibited an exchange field of 50 Oe and on annealing the exchange field increased to 63 Oe. No major changes in exchange field was observed with film thickness and annealing.

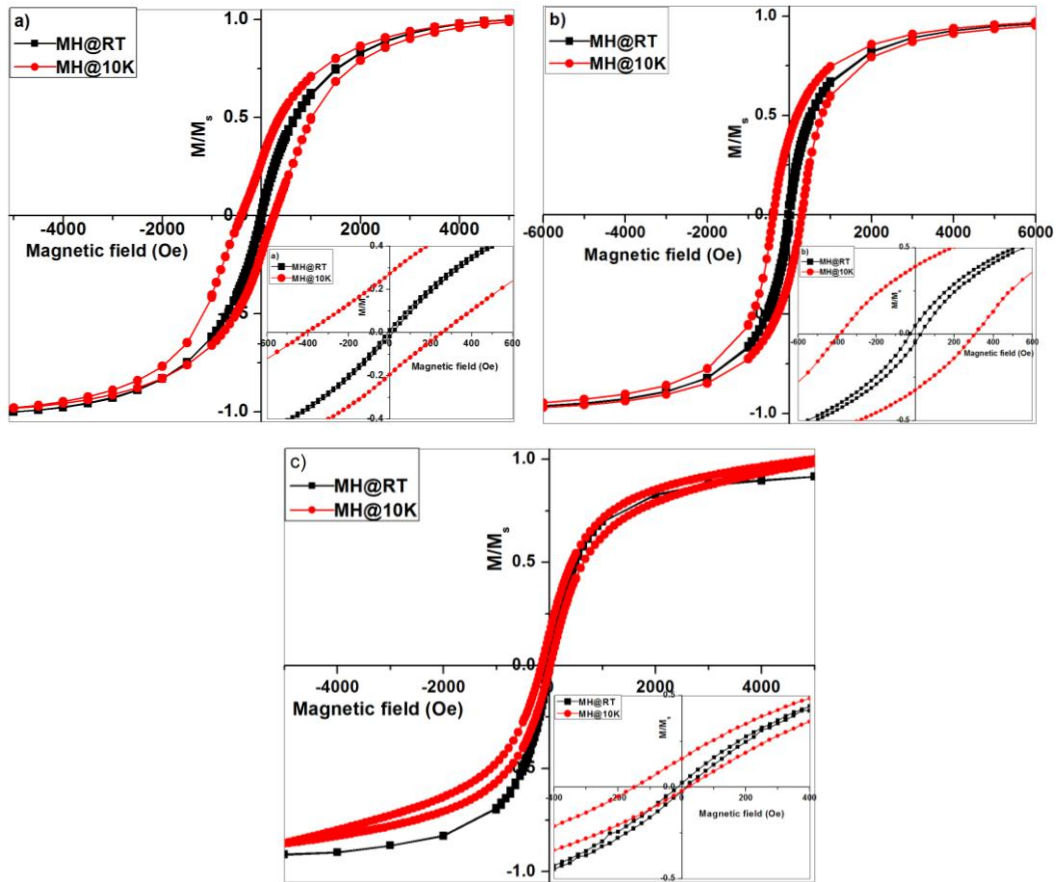


Fig. 3 Hysteresis loops recorded at room temperature and at 10K of a) FNMB-ZF1 b) FNMB-ZF2 and c) FNMB-ZF2 annealed at 873K

The observed exchange bias effect in FeNiMoB-Zinc ferrite bilayer film is not due to FM-AFM interaction, because thin film forms of zinc ferrite are not antiferromagnetic at 10K. They exhibit ferrimagnetic ordering along with glassy behavior [22, 32]. Studies on zinc ferrite thin films presented in previous chapters also suggest the existence of glassy behavior. Many groups have reported exchange bias in spin glass ferromagnetic system [3, 17, 33]. In such cases the spin glass is considered to be diluted AFM system with long range interaction [3].

## Chapter 7

All related effects of exchange bias in FM-AFM systems are observed in FM-SG systems also. Thus the exchange bias observed in the present system could also be attributed to FM-SG interaction. The wide discrepancy between FC and ZFC in the MT curve (figure 4) also indicates glassy state of the system. The blocking temperature  $T_B$  for pristine film is 100K and is found to be independent of thickness.

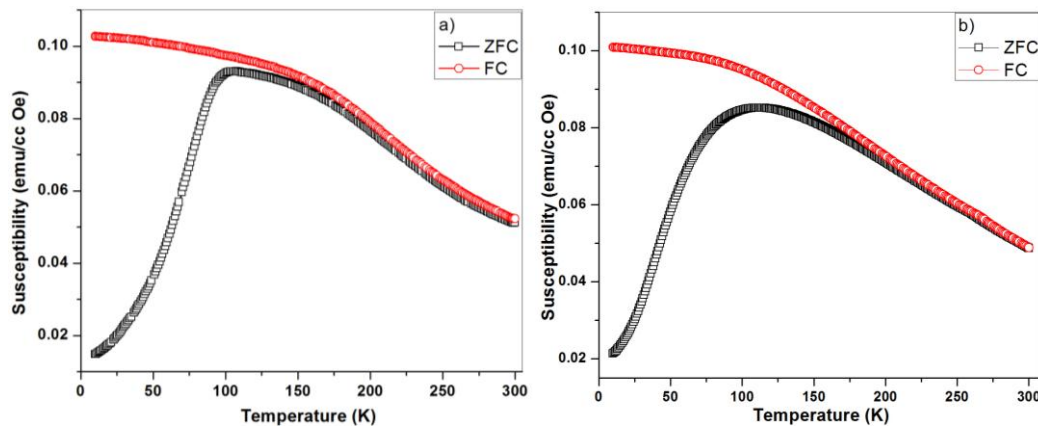


Fig. 4 FC-ZFC of a) FNMB-ZF1 b) FNMB-ZF2

### 7.3.2 Dependence of swift heavy ion irradiation on Exchange Bias

The electronic energy loss of 100 MeV ions in zinc ferrite is 0.015 MeV/nm as simulated using SRIM code (figure 5) [31]. The range of ions is about 12 $\mu$ m, which is much greater than the film thickness. The ions on traversing through the zinc ferrite layer of thickness 400 nm lose energy of 6 MeV and the remaining 94 MeV is transferred to the next layer. The energy loss in FeNiMoB layer is 0.016 MeV/nm. The range of ions in this layer is about 11 $\mu$ m, and the ions get deposited in the substrate terminally.

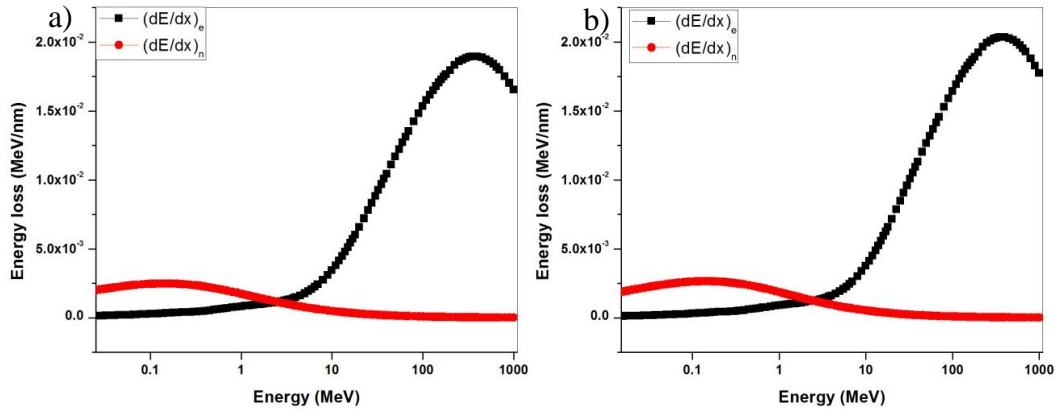


Fig. 5 Energy loss of 100 MeV ions in a) zinc ferrite and b) FeNiMoB

In the GXR D studies, (figure 6) the (311) plane corresponding to spinel zinc ferrite is observed. It is difficult to obtain the Fe-Ni phase for the second layer by GXR D due to the nominal concentration of Fe-Ni crystallites. The crystallite size is calculated using Scherrer formula and is  $\sim 7$  nm. The (311) plane narrows out on annealing at 873K and consequently the crystallite size increases to 12 nm. The crystallite size increases for films irradiated at  $1 \times 10^{11}$  ions/cm<sup>2</sup> and is  $\sim 15$  nm and reduces to  $\sim 10$  nm at  $1 \times 10^{12}$  ions/cm<sup>2</sup>. At higher fluences, complete amorphisation of films takes place.

## Chapter 7

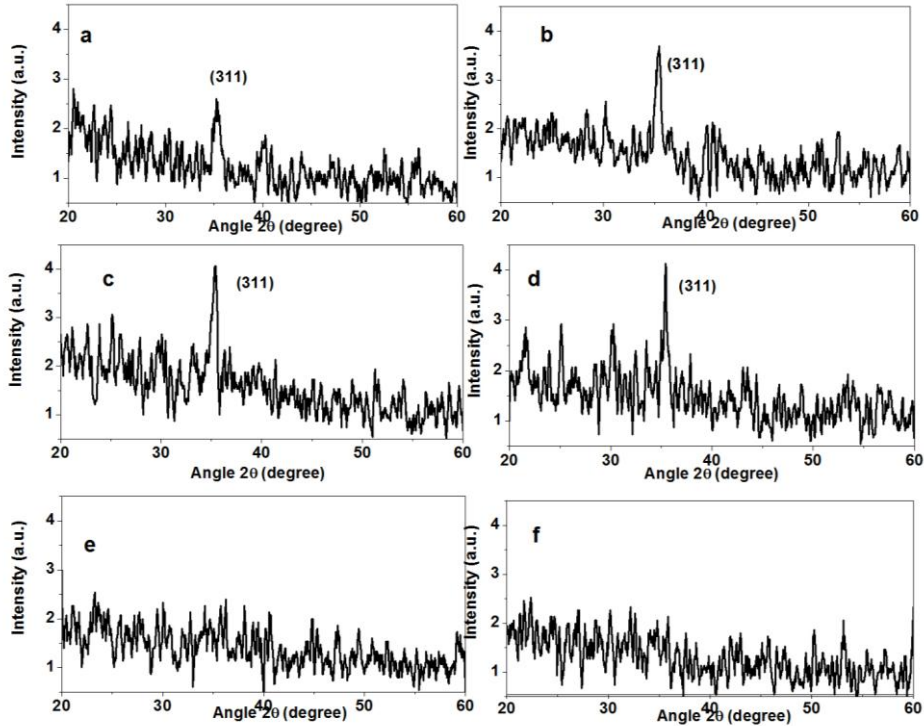


Fig. 6 GXR D pattern of a) pristine film b) film annealed at 873K, film annealed at 873K and irradiated at fluences of c)  $1 \times 10^{11}$  d)  $1 \times 10^{12}$  e)  $1 \times 10^{13}$  and f)  $3 \times 10^{13}$  ions/cm<sup>2</sup>

FC-ZFC measurements (figure 7) were conducted to study the magnetic ordering and the influence of ion fluence on  $T_B$ . The  $T_B$  for the sample irradiated at fluence of  $1 \times 10^{12}$  ions/cm<sup>2</sup> is around 100K same as that of pristine film. On irradiation not much changes in blocking temperature was observed. However  $T_{irr}$ , the temperature at which FC-ZFC curve bifurcate shifts to room temperature at higher fluences. The large irreversibility between FC and ZFC indicates glassy behaviour of the system. The saturation of FC below  $T_B$  is also indicative of a glassy behaviour.

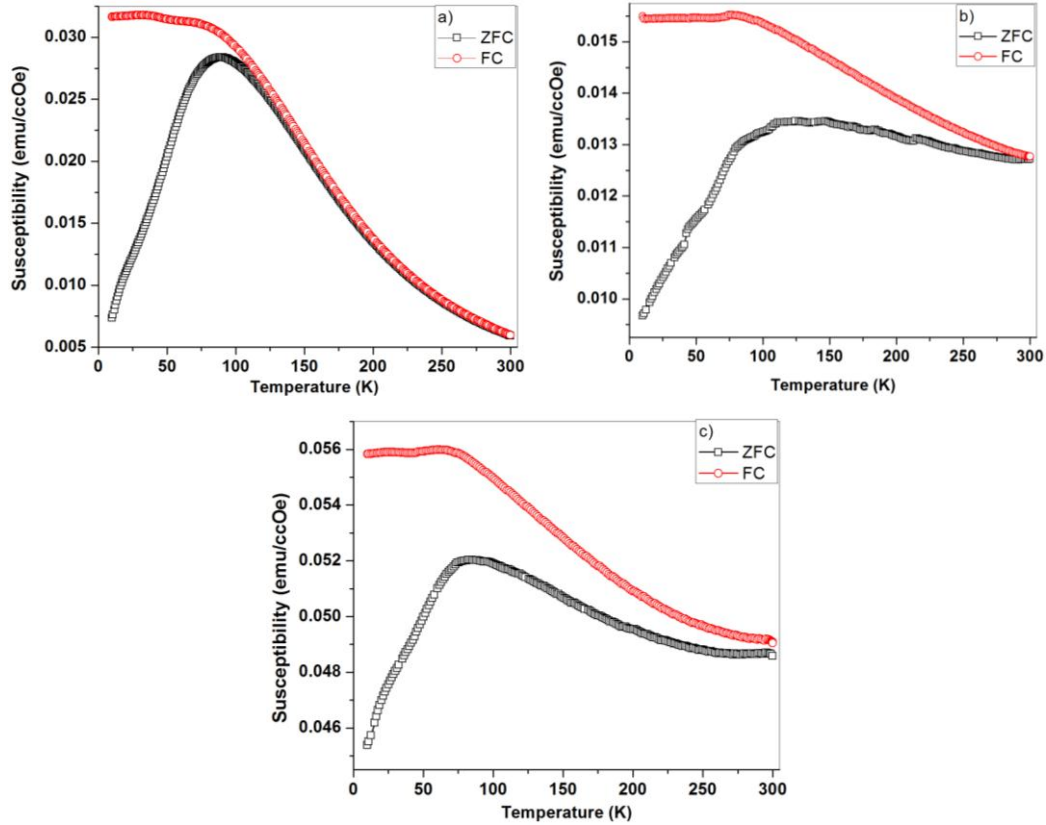


Fig. 7 FC-ZFC curves of FeNiMoB-Zinc ferrite film annealed at 873K and irradiated at fluences of a)  $1 \times 10^{12}$  b)  $1 \times 10^{13}$  and c)  $3 \times 10^{13}$  ions/cm<sup>2</sup>

Hysteresis (MH) loops at room temperature and at 10K of the irradiated films with field cooling of 5000 Oe are shown in figure 8. An exchange field of around 50 Oe is observed in the pristine film and on annealing at 873K, the exchange field increased to ~63 Oe (figure 3b-3c). On irradiation, it is observed that at low fluences, in particular  $1 \times 10^{11}$  and  $1 \times 10^{12}$  ions/cm<sup>2</sup>, exchange field shows an enhancement and then decreases on further increase of ion fluence. A maximum exchange field of 210 Oe is observed for the film irradiated at  $1 \times 10^{12}$  ions/cm<sup>2</sup>. The  $H_E$  value decreases to ~25 Oe for film irradiated at  $1 \times 10^{13}$  and

## Chapter 7

$3 \times 10^{13}$  ions/cm<sup>2</sup>. The variation of exchange field with ion fluence is shown in figure 9. Apart from variation in exchange bias field and coercivity, other phenomena related to exchange bias like loop widening and shift in positive magnetization is also observed.

Mougin *et al.* explained the change in exchange field with low energy ion irradiation with the help of a diluted AFM model [15]. He proposed that ion irradiation creates defects in the AFM and these defects act as pinning centres and thereby enhances the exchange field. The ion beam mixing at the interface presumably destroys magnetic order and suppresses exchange field. The net effect of ion dose on exchange field is given by the following expression

$$\frac{H_{EB}}{H_{EB,ini}} = (1 \pm aptN) \times e^{-b_1N} \quad (7.1)$$

where  $H_{EB}/H_{EB,ini}$  is the normalised exchange bias field with respect to exchange field before irradiation, 'N' is the ion dose, 't' thickness of AFM layer, 'p' the probability of the atom to be displaced per incoming ion per unit length, 'a' the parameter that describes the efficiency of the ion to create a defect in AFM and 'b<sub>1</sub>' is the parameter that indicates the efficiency of the defect at the interface to decrease exchange field. Most of the experiments carried out on irradiation induced exchange bias follow this equation; according to which, an increase in exchange bias is observed at low fluences and at higher fluences exchange bias is decreased [19, 34].

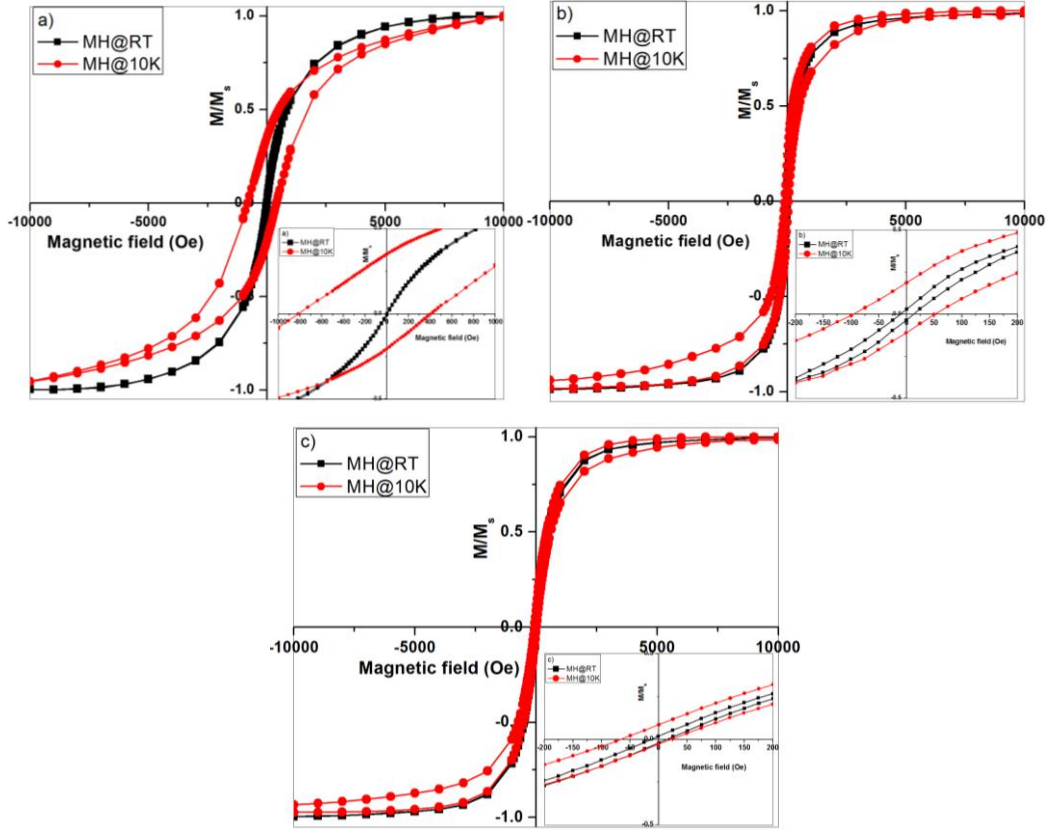


Fig. 8. MH loops of FeNiMoB-Zinc ferrite film annealed at 873K and irradiated at fluences a)  $1 \times 10^{12}$  b)  $1 \times 10^{13}$  and c)  $3 \times 10^{13}$  ions/cm<sup>2</sup> (inset shows enlarged graphs)

Our experimental result is fitted by using equation 7.1 and the fitting is found good at lower fluences, while at higher fluences, an exact fitting with experimental data is not possible (figure 9). The value of  $a$  and  $b$  was observed to be 0.6 and 18. Thus, the observed increase in exchange bias at low fluences can be explained as a result of defect creation in the zinc ferrite layer. These defects act as pinning centres for domain wall formation which can reduce the domain wall energy leading to stabilisation of the system. The formation of domain walls

## Chapter 7

results in enhanced loop shift. Further increase of ion fluence leads to excessive ion beam mixing at the interface, which affects the magnetic order in AFM layer. This decreases exchange coupling and thereby the exchange bias.

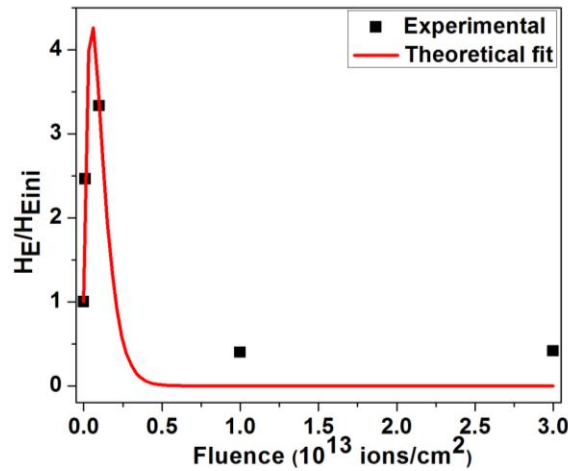


Fig. 9 Variation of exchange field with ion fluence

The variation of coercivity with ion fluence is shown in figure 10,  $H_c$  initially increases, exhibits a maximum value of 610 Oe at  $1 \times 10^{12}$  ions/cm $^2$  and then decreases. The correlation between coercivity and exchange field can provide information regarding the microscopic origin of exchange anisotropy and was studied by different groups [35, 36, 37, 38]. Leighton *et al.* observed that the enhancement of coercivity is proportional to the exchange coupling and the increase in coercivity is attributed to enhanced pinning of domain walls [35]. Morales *et al.* observed no direct correlation between coercivity and exchange field in Ni and Py layers [38]. In our study we have observed direct relation between variation of coercivity and exchange field with ion fluence and is fitted using equation 7.1. The fitting parameters a and b are 2 and 21. According to the

theoretical fit, the variation of coercivity can be explained as follows; at low fluences, the defect enhances the coercivity, while at higher fluences mixing of ions lowers the coercivity. The mechanism responsible for variation of exchange field with ion fluence is also responsible for the variation of coercivity.

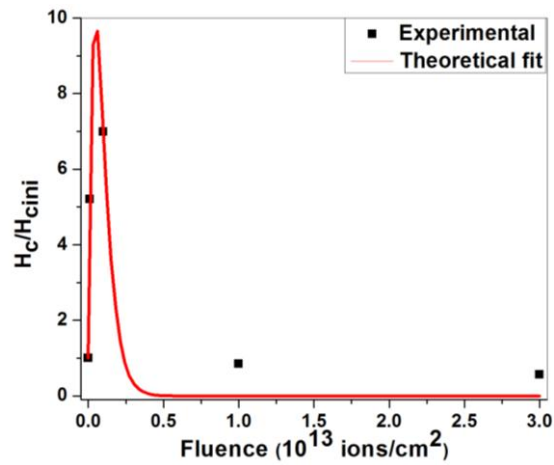


Fig. 10 Variation of coercivity with ion fluence

The sample irradiated at  $1 \times 10^{12}$  ions/cm $^2$  which exhibits the maximum exchange field was subjected to field cooled MH measurements at different temperatures of 40K, 50K, 80K, 100K and 120K (figure 11). No field shift is observed which establishes the fact that exchange field is observed far below the transition temperature which is 100K in the present case.

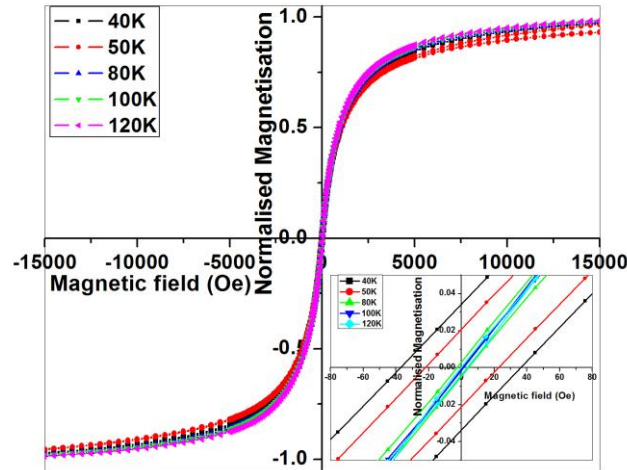


Fig. 11 MH loops of film irradiated at fluence of  $1 \times 10^{12}$  ions/cm<sup>2</sup> at different temperatures

#### 7.4 CONCLUSION

In summary, FeNiMoB-Zinc ferrite bilayer films exhibiting exchange bias was fabricated by RF sputtering at different FM and AFM thicknesses. Exchange bias was observed in FeNiMoB-Zinc ferrite films of both thicknesses and is attributed to FM-SG coupling. The exchange bias decreased on increasing the FM-AFM thickness and on annealing, significant changes in exchange bias was not observed.

The films annealed at 873K were irradiated with 100 MeV Ag ions at different fluences. Ion irradiation enhanced exchange bias at lower fluences and decreased at higher fluences. Highest exchange field of 210Oe was obtained on irradiation at a fluence of  $1 \times 10^{12}$  ions/cm<sup>2</sup>. The variation in exchange bias with ion fluence is modeled based on the competition between defect creation in AFM layer and interfacial mixing. The defect created by ions act as pinning centers in the AFM and this causes an enhancement in exchange bias at lower fluences. At higher fluences, the defects destroy the order at the FM-AFM interface, and hence

exchange bias decreases. The behavior of coercivity with ion fluence follows the variation of exchange field which implies that both the exchange field and coercivity are correlated. Thus both exchange field and coercivity can be tailored by swift heavy ion irradiation.

**REFERENCES:**

- [1] J. Nogués, J. Sort, V. Langlais, V. Skumryev, S. Suriñach, J.S. Muñoz, and M.D. Baró, *Phys. Rep.* **422** (2005) 65
- [2] Y.H. Cheng, X.H. Zhang, L.Y. Li, C.H. Wang, X.G. Luo, H. Liu, W.H. Wang, and R.K. Zheng, *Appl. Phys. Lett.* **10** (2013) 192403
- [3] K.D. Usadel and U. Nowak, *Phys. Rev. B* **80** (2009) 614418
- [4] R.L. Stamps, *J. Phys. D: Appl. Phys.* **33** (2000) R247
- [5] P. Miltenyi, M. Gierlings, J. Keller, B. Beschoten, G. Guntherodt, U. Nowak, and K. Usadel, *Phys. Rev. Lett.* **84** (2000) 4224
- [6] D. Mauri, H.C. Siegmann, P.S. Bagus, and E. Kay, *J. Appl. Phys.* **62** (1987) 3047
- [7] A. P. Malozemoff, *J. Appl. Phys.* **63** (1988) 3874
- [8] J. Nogués, C. Leighton and I.K. Schuller, *Phys. Rev. B* **61** (2000) 1315
- [9] A.P. Malozemoff, *Phys. Rev. B.* **37** (1988) 7673
- [10] R. Yanes, J. Jackson, L. Udvardi, L. Szunyogh, and U. Nowak, *Phys. Rev. Lett* **111** (2013) 217202
- [11] A.L. Kobrinskii, A.M. Goldman, M. Varela and S. J. Pennycook, *Phys. Rev. B* **79** (2009) 094405
- [12] H. Sang, Y.W. Du, and C.L. Chien, *J. Appl. Phys.* **85** (1999) 4931
- [13] V. Baltz, J. Sort, S. Landis, B. Rodmacq and B. Dieny, *Phys. Rev. Lett.* **94** (2005) 117201

*Chapter 7*

- [14] T. Mewes, R. Lopusnik, J. Fassbender, B. Hillebrands, M. Jung, D. Engel, A. Ehresmann, and H. Schmoranzer, *Appl. Phys. Lett* **76** (2000) 1057
- [15] A.Mougin, T. Mewes, M. Jung, D. Engel, A. Ehresmann, H. Schmoranzer, J. Fassbender, and B. Hillebrands, *Phys. Rev. B* **63** (2001) 060409
- [16] E. Demirci, M. Öztürk, R. Topkaya, S. Kazan, N. Akdoğan, M. Obaida, and K. Westerholt, *J. Supercond. Nov. Magn.* **25** (2011) 2591
- [17] M. Ali, P. Adie, C.H. Marrows, D. Greig, B.J. Hickey, and R.L. Stamps, *Nat. Mater.* **6** (2007) 79
- [18] P. Miltényi, M. Gierlings, M. Bammig, U. May, G. Güntherodt, J. Nogués, M. Gruyters, C. Leighton, and I.K. Schuller, *Appl. Phys. Lett.* **75**, (1999) 2304
- [19] S. Poppe, J. Fassbender and B. Hillebrands, *Europhys. Lett.* **66** (2004) 430
- [20] A.Mougin, S. Poppe, J. Fassbender, B. Hillebrands, G. Faini, U Ebels, M Jung, D Engel, A Ehresmann, H Schmoranzer, *J. Appl. Phys* **89** (2001) 6606
- [21] Ali C. Basaran, T. Saerbeck, J. de la Venta, H. Huckfeldt, A. Ehresmann, and Ivan K. Schuller, *Appl. Phys. Lett.* **105** (2014) 072403
- [22] S. Nakashima, K. Fujita, K. Tanaka, and K. Hirao, *J. Phys. Condens. Matter* **17** (2005) 137
- [23] K. Tanaka, S. Nakashima, K. Fujita and K. Hirao, *J. Phys: Cond. matter* **15** (2003) 469
- [24] M. Bohra, S. Prasad, N. Kumar, D.S. Misra, S.C. Sahoo, N Venkataramani and R Krishnan, *Appl. Phys. Lett.* **88** (2006) 262506
- [25] Y.Yamamoto, H.Tanaka, and T.Kawai, *Jpn. J. Appl. Phys.* **40** (2001) L545
- [26] S.D. Shenoy, P.A. Joy, M.R. Anantharaman, *J. Magn. Magn. Mat.* **269** (2004) 217

- [27] M.R. Anantharaman, S. Jagatheesan, K.A. Malini, S. Sindhu, A. Narayanasamy, C.N. Chinnasamy, J.P. Jacobs, S. Reijne, K. Seshan, R.H.H. Smits, H.H. Brongersma, *J. Magn. Magn. Mat.* **189** (1998) 83
- [28] T Hysen, S Deepa, S Saravanan, R V Ramanujan, D K Avasthi, P AJoy, S D Kulkarni and M R Anantharaman, *J. Phys. D: Appl. Phys.* **39** (2006) 1993
- [29] Hysen Thomas, Senoy Thomas, Raju V. Ramanujan, D.K. Avasthi, I.A. Al-Omari, Salim Al-Harhi, M.R. Anantharaman, *Nucl. Instrum. and Methods in Phys. Res. B* **287** (2012) 85
- [30] Senoy Thomas, Hysen Thomas, D. K. Avasthi, A. Tripathi, R. V. Ramanujan, and M. R. Anantharaman, *J. Appl. Phys.* **105** (2009) 033910
- [31] Ziegler J F, Biersack, J P, Littmark U, *The Stopping and Range of Ions in Solids* (New York: Pergamon) SRIM code: <http://www.srim.org> (1985)
- [32] S. Nakashima, K. Fujita, K. Tanaka, K. Hirao, T. Yamamoto, and I. Tanaka, *J. Magn. Magn. Mater.* **310**, (2007) 2543
- [33] F.-T. Yuan, J.-K. Lin, Y.D. Yao, and S.-F. Lee, *Appl. Phys. Lett.* **96**, (2010) 162502
- [34] N. Srivastava and P.C. Srivastava, *Radiat. Eff. Defect S.* **169** (2014) 529
- [35] C. Leighton, J. Nogues, B. Jonsson-Akerman, and I. Schuller, *Phys. Rev. Lett.* **84** (2000) 3466
- [36] R. Jungblut, R. Coehoorn, M.T. Johnson, Ch. Sauer, P. J. van der Zaag, A. R. Ball, Th. G. S.M. Rijks, J. aan de Stegge, and A. Reinders, *J. Magn. Magn. Mater.* **148** (1996) 300
- [37] R. Jungblut, R. Coehoorn, M.T. Johnson, J. aan de Stegge, and A. Reinders, *J. Appl. Phys.* **75** (1994) 6659.
- [38] R. Morales, Zhi-Pan Li, J. Olamit, Kai Liu, J. M. Alameda, and Ivan K. Schulle *Phys. Rev. Lett.* **102** (2009) 097201.

*Chapter 7*

## **Chapter 8**

### **Conclusions and Future Scope**

*Chapter 8*

### *Conclusions and Future Scope*

Magnetic alloys are an integral member belonging to the family of magnetic materials, which are of recent origin and increasingly being researched upon. They are amorphous in character and find extensive applications in many modern day devices. Metallic glasses belonging to the family of magnetic alloys is a new entrant and is promising and seen as a potential substitute to the existing conventional materials based on ferrites and permalloys. They are soft and the electrical conductivity is quite reasonable. Normally they are made in the form of ribbons. Though ribbons are amorphous in nature, nanocrystallinity can be induced and can be made crystalline. Newer applications like Magnetic Micro Electro Mechanical Systems (MEMS), Nano Electro Mechanical Systems (NEMS) and Tunnel Magneto Resistance (TMR) sensors necessitate that they are made in the thin film forms. The properties of ribbon and their thin film form need not be the same since ribbons are amorphous and on deposition they transform to crystalline.

Thin films of metallic glasses can be deposited on substrates from targets of appropriate compositions. Retention of the target composition in the film as well is an essential criterion. If one resorts to thermal evaporation, though good quality films can be obtained, the composition of the film are at variance with the parent target. This forces one to employ methods like RF sputtering and pulsed laser deposition. Though the target themselves are amorphous, the end film could be crystalline or vice versa. Hence post deposition thermal annealing is required to modify their magnetic properties. The employment of swift heavy ion (SHI) irradiation in the modification of magnetic properties is well known and thus SHI can be employed to modify the morphology and in turn the magnetic properties. This is part one of the present investigation, that is, fabricating thin films of metallic glass alloys based on Fe-Ni and the modification of their properties.

## *Chapter 8*

Zinc ferrite in the bulk is a normal spinel and exhibits anomalous properties in the nanoregime. However, literature on their thin film forms are less abundant and an interesting area of research. Their modification by employing thermal annealing and SHI was another motive of the present study.

Exchange bias is a relatively newer phenomenon involving ferromagnetic-antiferromagnetic (FM-AFM) structures. A bilayer consisting of a zinc ferrite and metallic glass based on Fe-Ni was thought to be ideal where in zinc ferrite serve as an AFM/spin glass (SG) and Fe-Ni the FM component. This investigation was undertaken with a two pronged objective. Firstly, to see the feasibility of fabricating a bilayer exchange bias system, and secondly, to study the effect of SHI on the exchange bias and exchange field. This is phase two of the present investigation.

The salient findings of the present study is listed in this chapter. As it is natural for any human, we need to strive for perfection and in the search for perfection we often subject ourselves to criticism. All the demerits of this study is brought out as seen by the author and the scope for improvements and future studies is also discussed.

We started by depositing thin films from a target of  $\text{Fe}_{40}\text{Ni}_{38}\text{Mo}_4\text{B}_{18}$  by using RF sputtering method. From the compositional studies using X-ray Photoelectron Spectroscopy (XPS), it was found that we succeeded in incorporating Fe, Ni, Mo and B in the thin film; however the exact stoichiometry of the target composition could not be retained in the film due to the contamination of oxygen. Contrary to the target which was amorphous, thin films were crystalline and the phase was FeNiMoB which is predominantly non magnetic. However, the films were ferromagnetic at room temperature with

diminished saturation magnetization. Post thermal annealing of these films did not improve their magnetic properties.

The next question that comes to our mind is can we improve the magnetic properties of FeNiMoB thin films? If the crystalline FeNiMoB phase is modified, there are chances that magnetic properties can be improved, as the amorphous counterparts exhibited superlative magnetic properties. To amorphise, SHI irradiation is a suitable technique. The high energy imparted to the material can cause localized high temperature zones and the sudden cooling when the ion transits results in amorphisation. SHI irradiation is a highly versatile technique used for nanostructuring and material modification. FeNiMoB films were irradiated using 100MeV Ag ions at different fluences. At an initial fluence of  $1 \times 10^{12}$  and  $1 \times 10^{13}$  ions/cm<sup>2</sup> an increase in grain size was observed from atomic force microscopy images, and at the highest fluence of  $3 \times 10^{13}$  ions/cm<sup>2</sup>, the grain size decreased rapidly. On irradiation, the crystalline FeNiMoB phase has been completely eliminated. The decrease in grain size along with amorphisation at the highest fluence of  $3 \times 10^{13}$  ions/cm<sup>2</sup> substantially enhanced the magnetic properties of FeNiMoB thin films.

Zinc ferrite, an antiferromagnet with a Neel temperature of 10K is a normal spinel in the bulk. Thin films and nanostructures of zinc ferrite exhibit altogether different magnetic properties due to cation redistribution. Thus nanosized zinc ferrite is a subject of intense studies. Zinc ferrite thin films were prepared by RF sputtering and they exhibited room temperature ferrimagnetism with a saturation magnetization of 120emu/cc. The shift in the blocking temperature from 10K to higher temperatures is attributed to cation redistribution resulting in a possible  $J_{AB}$  interaction. Zinc ferrite sample also exhibited spin glass behavior. Thermal annealing deteriorated the magnetic properties by lowering the

## Chapter 8

saturation magnetization and lowering the blocking temperature. On annealing, the cations have a tendency to reverse back to the normal spinel structure.

The formation of latent tracks in ferrites by swift heavy ion irradiation offers possibilities to study the stress induced magnetic properties. Zinc ferrite thin films were irradiated with 100 MeV Ag ions. The crystalline percentage of the spinel structure reduced on ion irradiation. At initial fluences, the grain size decreased and at the highest fluence of  $3 \times 10^{13}$  ions/cm<sup>2</sup> the grain size enhanced. This increase in grain size was visible from atomic force microscopy images and is due to agglomeration. The magnetic properties were dependent on grain size and highest saturation magnetization was for the pristine sample. With ion irradiation, the magnetization shows an initial decrease and at highest fluence a nominal increase was observed. This has been correlated with grain size. Another interesting observation was that at 5K of temperature, the pristine samples did not saturate even at the highest applied field of 60 kOe. But as irradiation progressed, films attained saturation at very low fields. Irradiation reduced the antiferromagnetic contribution.

It is well known that an FM-AFM or a FM-SG can exhibit exchange bias effect and these kinds of exchange coupled systems are highly desirable in various spintronic devices. The ferromagnetic property of FeNiMoB films can be coupled with the antiferromagnetic or spin glass property of zinc ferrite. To realize an exchange bias system we have adopted a bilayer structure of FeNiMoB and zinc ferrite. The role of thickness, thermal annealing and ion irradiation on the exchange bias was examined. The bilayer film of FeNiMoB and zinc ferrite exhibited exchange bias at 10K with an exchange field of 75 Oe. The observed exchange bias was attributed to FM-SG interaction. On increasing the layer thickness exchange field reduced to 50 Oe and on annealing a small increase of

## *Conclusions and Future Scope*

13Oe in exchange bias was observed. Appreciable changes in exchange bias properties could not be obtained by altering the thickness and annealing temperatures.

As the exchange bias is influenced by the interface, modification of interface can substantially cause changes in exchange field. The bilayer films were irradiated using 100 MeV Ag ions. The exchange field increased at initial fluence, reached a peak value of 210 Oe at a fluence of  $1 \times 10^{12}$  ions/cm<sup>2</sup>, and then decreased on further increase of ion fluence. The variation of exchange field with ion fluence is modeled as a competition between ion induced defect formation and interfacial mixing. At lower fluences, ions create defects in the AFM and these defects can act as pinning centers for domain wall formation thereby enhancing the exchange bias. At higher fluences, due to interfacial mixing the exchange field gets suppressed. Thus the role of ion irradiation as an efficient tool to modify the exchange bias was examined.

Further systematic studies on preparation of FeNiMoB by RF sputtering by changing the deposition parameters like RF power may result in the formation of magnetic Fe-Ni phase. The oxidation of these films is a major cause for worry and a reason for the decrease in magnetization. The target composition could not be retained due to oxidation. Passivation is an alternative, and can be passivated by coating a thin film of gold or a polymer.

Even though zinc ferrite films exhibited room temperature ferrimagnetic behavior; the actual reason for this change is still elusive. Extensive studies on deducing the structure and the cation distributions have to be performed by high end analytical tools such as Extended X-ray Absorption Fine spectroscopy (EXAFS) and neutron scattering. The track formation in spinels as a result of ion irradiation also has to be visualized by cross sectional TEM. Once the tracks and

## *Chapter 8*

its diameter are evaluated by appropriate tuning of ion energy and fluence, the track diameter can be tailored and nanostructures can be obtained.

The main application of exchange coupled systems is in magnetic tunnel junctions. The pinning of ferromagnetic layer can be achieved by exchange coupling with an AFM. But most of the AFM materials have Neel temperature below room temperature which are not of much use from an application point of view. Fabricating an exchange coupled system, under an applied magnetic field will ensure proper alignment of the top AFM layer. The modification of exchange bias properties by SHI is a highly efficient method. But visualization of interface by cross sectional TEM is rather difficult. The exact cause of the change can be ascertained only after observing the interface. Also, micromagnetic simulation on ion induced modifications can be looked after as a theoretical study.

When a thesis is being submitted a barrage of questions crop up in one's mind, very often the questions transcend from science to philosophy and society. A few of the pertinent questions are, whether I could deliver what I intended? Whether my thesis has the required quality, whether this piece of investigation going to benefit the society at large or not! Most often the answers to these questions are found in the very philosophy of research itself. That is, if this work is not earth shattering, has it added value to the existing? In this case, the answer is yes, it has contributed incrementally. This is often referred to as incremental science! Every thesis contributes incrementally to the knowledge base. This thesis is no exception to this! Pondering over the question of reproduction of results or repeatability, one often, repeats the experiment twice or thrice, the idea is to 'kill' the new result, if it reemerges like the phoenix it is accepted and a new result. The observance of exchange bias in a bilayer film of FeNiMoB-zinc ferrite was repeated and verified as a new result.

### *Conclusions and Future Scope*

Another obvious criticism is the employment of SHI for material modification, which is exorbitantly expensive and not suitable for large area application. However one take solace in the fact that if one can thoroughly understand the Physics behind the modification of material properties by SHI, a suitable inexpensive ‘down to earth’ technique can be devised to achieve the same effects. This is positive thinking and is earmarked for future.

In this investigation we have only looked at the possibility of an exchange coupled system using a bilayer of FeNiMoB and zinc ferrite. Fe-Ni based alloy thin films can also be used to fabricate TMR sensors and or even a cantilever consisting of a Fe-Ni phase for sensing gases or magnetic fields. These are some devices which can be fabricated by simple fabrication technique. However these propositions are futuristic. With the emergence of internet of things sensors are going to play a significant role. So metallic glasses can be a component of a energy harvester along with a magneto electric component for self driven sensors.

Any researcher who does not think differently and do not intend to innovate is not delivering his duty. Finally let me conclude with the words of JRD Tata, “More than ever before we must be ready to think every problem afresh, to change and innovate”.

*Chapter 8*